Thèse présentée à L'Université de Lille
Ecole Doctorale Sciences pour L'Ingénieur

Pour obtenir le grade de

DOCTEUR DE L'UNIVERSITÉ

en

Electronique, Microélectronique, Nanoélectronique et Micro-ondes

par

ROBIN BENARROUCH

Wireless Hub for the Human Intranet

—

Hub Sans Fil pour l'Intranet du Corps Humain

Préparée en collaboration avec:

STMicroelectronics
Le laboratoire IEMN
Le laboratoire BWRC

Soutenue le 20 Janvier 2021, devant la commission d'examen

Mme Hakima CHAOUCHI	Institut Polytechnique de Paris, Telecom Sud Paris	Présidente
M. Adam WOLISZ	TU Berlin	Rapporteur
M. Aziz BENLARBI-DELAÏ	Sorbonne Université	Rapporteur
M. Ove EDFORS	Lund University	Examinateur
M. Alvaro ARAUJO	Universidad Politécnica de Madrid	Examinateur
M. Antoine FRAPPE	Junia	Invité
M. Jan RABAEY	UC Berkeley	Co-encadrant de thèse
Mme Andreia CATHELIN	STMicroelectronics	Co-directrice de thèse
M. Andreas KAISER	CNRS - Université de Lille	Directeur de thèse

A mes Parents,
qui se sont battus pour que nous
puissions devenir ce que nous sommes

A mes Frangins,
qui ont toujours veillé sur moi

A ma Tante,
qui est partie beaucoup trop vite

"À vaincre sans péril,
on triomphe sans gloire."

Pierre Corneille,
in *Le Cid*

"I'm falling
In all the good times I find myself
Longing for a change
And in the bad times I fear myself"

Lady Gaga, Mark Ronson,
in *Shallow, A Star is Born*

ABSTRACT

This Ph.D. research work has bee conducted within the framework of the Human Intranet (HI) concept, which creates a human-dedicated infrastructure allowing a wide span of IoT nodes and wearable peripherals to communicate. The realization of such a platform is challenging in terms of signal transmission due to body shadowing and body dynamics, achievable communication throughput for demanding applications, network architecture for reliability, and a flexible communication scheme maximizing the global efficiency. To fulfill these objectives, a combination of a human-compatible wireless communication modality with an associated networking strategy is required. This thesis manuscript proposes a Body-Coupled Communication scheme. The choice is motivated by a detailed channel characterization confirmed by experimental results. It is followed by a network architecture analysis leading to a custom mesh-of-star hybrid topology. Ultimately, a heartbeat-based synchronization and MAC protocol have been proposed, benefiting from the on-body network deployment.

Multiple communication options have been studied and their efficiency toward the HI project analyzed. We covered some RF possibilities as well as Body Couple Communication (BCC). Following the State-of-the-Art analysis, among all possible BCC propagation mechanisms, Capacitive coupling (C-BCC) was the most promising option given the HI requirements, the compatibility with existing solutions, and the room for improvement. Using the human body as a communication medium offers numerous interesting characteristics: security, safety, and energy efficiency. However, the propagation mechanism and the expected attenuation were unclear. A channel characterization has been conducted from theory through FEM simulations to on-body and on-phantom measurements. Ultimately a battery-powered prototype (with off-the-shelve components) has been implemented, confirming the initial characterization results. Finally, a frequency of operation of 450 MHz, was chosen for its dominant surface-wave propagation mechanism, offering a trade-off between attenuation, environment sensitivity, and bandwidth. Additionally, lower attenuation per unit of distance than other existing RF solutions has been demonstrated to the cost of higher insertion losses.

A two-layer mesh-of-stars hybrid network architecture has been proposed. The types of nodes composing the network, leaves (lower layer) or hubs (main nodes), are based on their computing capabilities, status in the network, access to energy, and the amount of data generated. While the hubs are connected in a mesh (or partial mesh) ensuring robustness and reliability, the leaves are linked to a unique hub as a local star topology, lowering the complexity and improving their power consumption. A puncturing communication scheme, allowing low traffic nodes to interrupt the main on-going data exchange within the proposed network has been envisioned. This approach combines the non-applicable existing communication standards' concepts with the characterized single-channel and Body Coupled Communication mechanism.

A MAC layer, pairing a heartbeat-based synchronization scheme with the puncturing mechanism has been imagined. It enables the node synchronization by sensing the bio-signal of interest to define a superframe-based structure. Its principle has been detailed and its system-level hardware architecture introduced. Equation-based mathematical models have been established, including the building blocks non-idalities. System-level simulations have been performed, and the results compared with a common duty-cycled radio architecture according to three major metrics: latency, channel availability, and system power consumption. Improvement in power consumption up to 47% and tight latency control have been demonstrated at no cost on the channel availability.

Résumé

Ce travail de doctorat a été mené dans le cadre du concept Human Intranet (HI), qui propose une infrastructure déployée sur le corps humain, permettant à différents types de nœuds de communiquer. La réalisation d'une telle plate-forme est complexe, notamment en termes de transmission du signal (ondes atténuées par le corps humain), de mouvements corporels, de débit maximum suffisant, d'architecture réseau fiable et de mécanisme de communication flexible, maximisant l'efficacité globale. Pour atteindre ces objectifs, une combinaison d'un mode de communication sans fil, compatible avec le corps humain et une stratégie de mise en réseau dédiée sont nécessaires. Ce manuscrit de thèse, propose d'utiliser une technique de communication utilisant le corps humain comme moyen de propagation. Le choix a mené à une caractérisation détaillée du canal, confirmée par les résultats expérimentaux. Il s'en est suivi une analyse de l'architecture du réseau, menant à une topologie hybride, en étoiles maillées. Finalement une synchronisation, basée sur les pulsations cardiaques et un protocole MAC, ont été proposés, bénéficiant du déploiement du réseau sur le corps.

Plusieurs options de communication ont été étudiées et leur efficacité, dans le cadre de Human Intranet, analysée. Nous avons étudié certaines communications RF, ainsi que celles couplées au corps humain (BCC). Parmi les mécanismes de propagation BCC possibles, le couplage capacitif (C-BCC) était l'option la plus prometteuse, compte tenu des exigences de Human Intranet. Utiliser le corps humain comme moyen de communication offre de nombreuses caractéristiques intéressantes : sécurité, sûreté et efficacité énergétique. Cependant, le mécanisme de propagation et l'atténuation attendue n'étaient pas établis. Une caractérisation du canal a été menée, avec une étude théorique, des simulations électromagnétiques et des mesures sur le corps. Finalement, un prototype, alimenté sur batterie, a été mis en œuvre, confirmant les résultats de la caractérisation. Enfin, une fréquence de fonctionnement de 450 MHz a été choisie, pour son mécanisme dominant de propagation des ondes de surface, offrant un compromis entre l'atténuation, la sensibilité de l'environnement et la largeur de bande.

Une architecture de réseau hybride en étoiles maillées, sur deux niveaux, a été proposée. Les types de nœuds composant le réseau, feuilles (couche inférieure) ou hubs (nœuds principaux), sont basés sur leurs capacités de calcul, leur statut dans le réseau, l'accès à l'énergie et la quantité de données générées. Alors que les hubs sont connectés de façon maillée (ou partiellement maillée), assurant robustesse et fiabilité, les feuilles sont liées à un hub unique, en tant que topologie locale en étoiles, ce qui réduit la complexité et améliore leur consommation d'énergie. Un schéma de communication « à perforation », permettant aux nœuds à faible trafic d'interrompre les échanges principaux de données en cours au sein du réseau proposé, a été envisagé.

Un protocole MAC, associant un schéma de synchronisation basé sur le rythme cardiaque, avec le mécanisme de perforation, a été imaginé et permet la synchronisation des nœuds, en détectant le signal biologique, pour établir une structure à base de superframe. Son principe a été détaillé et son architecture matérielle, au niveau du système, a été présentée. Des modèles mathématiques, basés sur des équations ont été établis, y compris les éléments constitutifs des non-idéalités. Des simulations, au niveau du système, ont été effectuées et les résultats ont été comparés à une architecture radio-cyclique commune, selon trois paramètres majeurs : la latence, la disponibilité des canaux et la consommation d'énergie du système. Une amélioration de la consommation d'énergie jusqu'à 47% et un contrôle strict de la latence, ont été démontrés, sans frais sur la disponibilité des canaux.

Acknowledgments

TABLE OF CONTENTS

LIST OF FIGURES

List of Tables

ACRONYMS

AO Always ON

AO-WRx Always On Wake-up Receiver

ASK Amplitude Shift Keying

BAN Body Area Network

BCC Body Coupled Communication

BER Bit Error Rate

BLE Bluetooth Low Energy

BPSK Binary Phase Shift Keying

BW Bandwidth

CA Channel Availability

CAP Contention Access Phase

C-BCC Capacitive Body Coupled Communication

CIFRE Conventions Industrielles de Formation par la Recherche

CMRR Common Mode Rejection Ratio

CSMA Carrier Sense Multiple Access

CW Continuous Wave

DR Data Rate

EAP Exclusive Access Phase

ECG Electrocardiogram

EFC Electric Field Communication

EM Electromagnetic

FCC Federal Communications Commission

FDTD Finite Difference Time Domain

FEM Finite Element Method

FM Frequency Modulation

FS Free-space

FSDT Frequency Selective Digital Transmission

G-BCC Galvanic Body Coupled Communication

GFSK Gaussian Frequency Shift Keying

HB Heartbeat

HBC Human Body Communication

HI Human Intranet

HR Heart Rate

IC Integrated Circuit

IEEE Institute of Electrical and Electronics Engineers

IR Impulse Radio

ISCAS IEEE International Symposium on Circuits and Systems

ISM Industrial Scientific Medical

LED Light Emitting Diode

LR Low Rate

MAC Medium Access Control

MAP Managed Access Phase

M-BCC Magnetic Body Coupled Communication

MEMS MicroElectroMechanical systems

MPE Maximum Permissible Exposure

NB Narrow Band

NF Noise Figure

OFDM Orthogonal Frequency Division Multiplexing

OOK On Off Keying

OSI Open Systems Interconnection

PAN Personal Area Network

PCB Printed Circuit Board

PCE Power Conversion Efficiency

PDR Packet Delivery Ratio

PHY PHYsical layer

PPM Part Per Million

QPSK Quadrature Phase Shift Keying

RAP Random Access Phase

RF Radio Frequency

RFID Radio Frequency IDentification

RMS Root Mean Square

RSSi Received Signal Strength indication

RTC Real Time Clock

Rx Receiver

SAR Specific Absorption Rate

SMA SubMiniature version A connector

SNR Signal to Noise Ratio

TDMA Time Division Multiple Access

TE Transverse Electric

TU Time Unit

Tx Transmitter

UHF Ultra High Frequency

ULP Ultra Low Power

UWB Ultra Wide Band

VNA Vector Network Analyzer

WB Wake-up Beacon

WBAN Wireless Body Area Network

WPAN Wireless Personal Area Network

WRX Wake-up Receiver

1. INTRODUCTION

Over the past decade(s), objects are getting smarter, more capable, and more connected. This evolution was enabled with low power designs and wireless communications (among others). The smartwatch was probably one of the first non-medical devices worn on-body for an extended period, transmitting and receiving data from other devices such as a smartphone or a computer.

The above observation naturally leads to thinking that many more objects worn on-body could become smart and used to provide information or trigger actions. Wearables are becoming more and more common, peripheral are getting more diverse and the need to interconnect all those nodes together came up very early, leading to the Internet of Things concept. Therefore, the Human Intranet, a network dedicated to the human body, is a mandatory infrastructure to enhance all the human-oriented applications, allowing multiple sensors and actuators to be connected.

This chapter introduces the research context and the parties involved in this research work. The global Human Intranet concept is then introduced along with application examples. A description of this thesis purpose is presented with the main associated contributions. Ultimately, the manuscript structure concludes this chapter.

1.1 Research Context & Human Intranet Concept

1.1.1 Research Context

This Ph.D. has been conducted in collaboration with STMicroelectronics, Crolles, France, under a CIFRE Program, the University of Lille, France, and the Berkeley Wireless Research Center (BWRC), University of California, Berkeley, Berkeley, California, USA. This thesis takes place in the ambitious and long term research project: "Wireless Systems and Architectures under Human Intranet".

1.1.2 The Human Intranet Concept

1.1.2.1 Overview

The Human Intranet in its entirety is a complex project, interleaving a wide range of research topics. It expands from the physical layer transmitting the information to the intelligence driving the embedded capabilities and features, including dedicated hardware such as custom integrated circuits (ICs), human body interface with implants, electrodes and sensors, radiating elements dedicated to the physical layer of interest and, the communication protocol belonging to the link layer.

The Human Intranet is part of a much bigger and wider "concept" described in [22] and [23] and named "The Swarm". The Swarm is the projection of the actual trend, which consists of connecting more and more objects, in the near future when almost any item would be a source or a destination of the information. It will make our environment smarter, offering new possibilities and applications to the end-users, enabled by the amount of data available, the different layers of computation implemented and the number of actuators accessible.

This section introduces the Human Intranet context and requirements defining the framework of this thesis. Within The Swarm introduced earlier and described in [1], the Human Intranet "relates how humans interact with the physical world around them [...] how they interact with their fellow human beings, and ultimately how they monitor and introspect themselves". [1] also defines "The scope of this Human Intranet is not solely confined to the human body, but
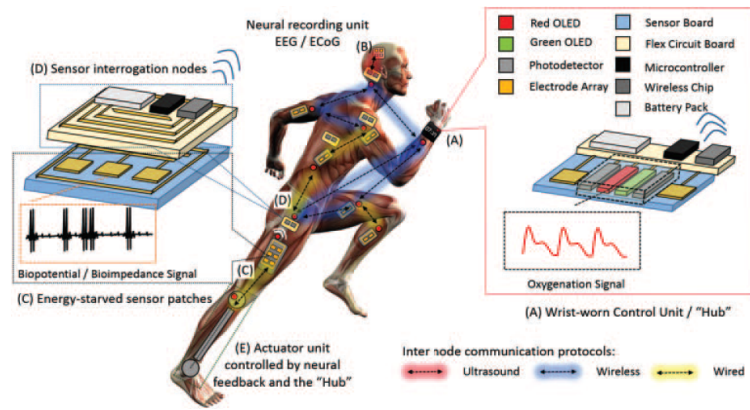
Figure 1.1: Example of a Human Intranet configuration targeting a neuroprosthesis (taken from [1]).

includes all devices and functions that are within the human's influence sphere at a given point in time. This means that any tool or object that moves with or is carried by a person (such as a bicycle, car, drill, or exoskeleton) is considered a wearable device, and hence is an inherent part of her/his Intranet". The integration of the Human Intranet within The Swarm requires the ability to connect and communicate with external devices and networks. The latter temporarily extend the already existing base-structure detailed below.

The Human Intranet is first and foremost a human dedicated and oriented network. It relies on a central backbone architecture deployed on the human body which this research work focuses on. As an on-body structure and by the nature of the data transmitted, the Human Intranet comes with specific requirements outlined in [1] and [23].

1.1.2.2 Requirements

Power consumption. The first requirement is about building an Ultra Low Power (ULP) network. All the energy resources are embedded and limited. The capability of a device connected to others to extend its operating life from a battery lies in three parameters. First, the node ultra low power design and consumption are mandatory; Second, the characteristics of the physical layer and, finally, the data link layer implementation. However, the hardware heavily relies on the physical layer of interest and, to some extent, on the MAC protocol. The former is thoroughly covered in chapter 2 while the latter is discussed in chapter 4.

Diversity. The Human Intranet must also flawlessly interconnect different types of nodes. They usually belong to two categories: sensors and actuators. The distinction between the two may not always be clear as a node can embed both capabilities. Sensors provide information regarding the surrounding environment such as pressure or brightness for instance but also on the wearer like its temperature or heart rate for example. Actuators follow the same behavior, from a fairly "simple" pacemaker to a more complex smart prosthetic with continuous feedback. A third category can be imagined for nodes only dealing with on- and off-body communication and data processing. This wide variety of devices must be properly considered from the early stages when building the Human Intranet to be addressed efficiently.

Data rate. Along with the wide variety of node building the Human Intranet introduced above, the maximum achievable data rate must be high enough to handle the most demanding operations. While the average required throughput may not be extraordinary (depending on the use-case), the peak data rate can be consequent. Finely controlling a smart prosthetic with real feedback and adjustment generates a significant amount of data.

Latency. The smart prosthetic use case presented above also comes with the notion of latency. While some actions are not time-sensitive (body temperature monitoring for instance), others, such as real-time feedback and control for a mechanical limb are. Latency management

and prediction are mandatory for critical life support applications (a pace-maker for instance) or enhancing the user experience (unlocking a car).

Security. Very common to any network, the security of the communication must be enforced within the Human Intranet. Since this network is dedicated to and deployed over the human body, it is more likely to carry very sensitive data than any other network. Privacy and security challenges are discussed in [24], highlighting a higher efficiency of systems designed with security features built-in compared to a security layer added *a posteriori.*

Safety. The safety of the network must be considered and addressed carefully. Its vicinity with human tissues requests the final solution to be compliant with the current regulations [25] and [26] to protect the wearer. It must as well not interfere with any biological signal as specified in [20], ensuring the end-user a worry-free experience.

Robustness. Another specificity of the human body is its mechanical degree of freedom and the countless possible associated movements. Unlike classic networks such as a company intranet, the Human Intranet continuously changes its shape, potentially leading to communication link unavailability. A redundant network layout is required to mitigate body dynamics, offering a robust and reliable architecture. The latter guarantees the proper operation of its critical functions. Following the same approach, body movements could, on the other hand, enable new communication routes. Thus, the Human Intranet must also be adaptive by handling those changes and benefiting from them to optimize the data exchange to this new configuration. Ultimately, while a given configuration can only be considered temporary, periodic patterns can be identified and an adapted communication pace can be derived [27].

Versatility. Besides body movements, connections and disconnections require specific attention to handle nodes' addition or removal. It is not a matter of re-routing the communication but creating new links and seamlessly allocating communication time without interrupting the on-going operations. The required degree of flexibility is achieved by combining the network's adaptivity and robustness of the physical and data link layers.

Intelligence distribution. The evolutionary, flexibility, and robustness requirements highlighted earlier regarding the network structure and communication ability are directly applicable to the intelligence distribution among the Human Intranet. While some decisions must be centralized as they necessitate data-gathering from all around or even outside the network, local decision making is mandatory for reactivity and latency purposes. The combination of centralized and distributed intelligence optimizes the network performance by triggering actions in a timely manner, not overflowing the network with unnecessary traffic, and still features the ability to address global issues.

Based on the requirements and challenges listed above, the development of a wireless hub might play a significant role in reaching the goals of the Human Intranet. It would act as a gateway between end nodes and the network. It would embed extended capabilities compare to the end nodes offering a local star topology to the network. This topic is addressed within the following section as part of the thesis purpose.

1.2 Thesis Purpose and Main Contributions

1.2.1 Thesis Objective

The objective of this thesis is to design a wireless and battery-powered communication platform dedicated to the Human Intranet, following the requirements highlighted in the above-section. Ultimately, the goal of this research work is to define the system specifications for a future implementation embedding the required functions enabling the Human Intranet.

The need for a structure deployed over the body, allowing any kind of peripherals to communicate is clear, the following questions must be answered to reach these goals: How do we

address it? What does the network should look like? Which communication mechanism should be implemented? How do we enable the communication?

The choice of the communication physical layer is of first importance. It sets numbers of parameters and cannot easily be changed *a posteriori*. The physical layer comes with its pros and cons and specifies the challenges to be addressed. This research work focuses on Body Coupled Communication (BCC) and more specifically on Capacitive-BCC (C-BCC). The state-of-the-art presented in chapter 2 shows interesting capabilities and implementations. However, none were satisfying regarding the targeted application in terms of bandwidth, data rate, mode of operation, and form factor. It led us to increase the frequency of operation from below 200 MHz to 450 MHz to overcome those limitations. At this frequency, none to extremely limited studies were available, raising the need for a full channel characterization. Toward the future implementation of a full solution, building the Human Intranet requires the constraints to be established upfront. A mandatory characterization has been conducted to set the specifications associated with the physical layer.

The Human Intranet is a global concept not only relying on the physical layer but also on a strong network architecture as introduced in the above section. While network architectures are known, none were directly compatible with the Human Intranet and its inherent constraints (limited access to energy, latency, flexibility, distributed computing resources...). Therefore, a dedicated topology for the Human Intranet has been imagined, taking into account its specificities and the envisioned physical layer. The types of nodes and their interconnections have been defined accordingly.

Given the choice of the physical layer and the network topology presented earlier, an appropriate communication scheme was required. While well-established power-saving techniques and communication protocols such as IEEE standards already exist, it has been demonstrated that they were not applicable "as is" or with very degraded outcomes. Within this thesis, a custom communication strategy along with a novel heartbeat-based synchronization scheme has been introduced, mathematically modeled, and quantitatively evaluated. They take advantage of the Human Intranet singularities to address the identified challenges such as: optimizing the power consumption while maximizing the average throughput with tight control on the communication latency.

1.2.2 Main contributions

The main contribution of this thesis are listed below:

- **Communication review.** Several communication technologies have been compared. Among all the possibilities, this work proposes Body Coupled Communication (BCC) and more specifically Capacitive-BCC (C-BCC) as the communication mechanism offering the best fit with the Human Intranet.

- **Capacitive Body Coupled Communication Characterization at 450 MHz.** This work has highlighted the frequency of 450 MHz as the best suited for the Human Intranet. Consequently, a full characterization in the 400 MHz to 500 MHz frequency band has been conducted.

- **Network topology.** A mesh-of-star network composed of hubs and leaves has been selected as the best possible configuration to built the Human Intranet.

- **MAC layer.** This work has introduced a new, human intranet-centered, heartbeat-based sycnrhonization scheme. In addition, a puncture-based communication protocol has been proposed.

- **Analytical modeling and demonstration.** A mathematical model including realistic system characteristics has been proposed. The simulations results reported in this work have highlighted better performance than existing solutions.

As a summary, this thesis focus was on characterizing the channel, establishing the network backbone architecture, and developing the human-oriented synchronization scheme including the system mathematical model. The above-listed contributions of this research work have led to the four following publications:

A. F. Solt, R. Benarrouch, G. Tochou, O. Facklam, A. Frappé, A. Cathelin, A. Kaiser, and J. Rabaey, **"Energy Efficient Heartbeat-Based MAC Protocol for WBAN Employing Body Coupled Communication,"** IEEE Access, pp. 1–1, 2020.

B. R. Benarrouch, A. Moin, F. Solt, A. Frappé, A. Cathelin, A. Kaiser, and J. Rabaey, **"Heartbeat-Based Synchronization Scheme for the Human Intranet: Modeling and Analysis,"** in 2020 IEEE International Symposium on Circuits and (ISCAS), 2020, pp. 1–5.

C. R. Benarrouch, A. Thielens, A. Cathelin, A. Frappé, A. Kaiser, and J. Rabaey, **"Capacitive Body-Coupled Communication in the 400–500 MHz Frequency Band,"** in EAI International Conference on Body Area Networks, Springer, 2019, pp. 218–235.

D. A. Thielens, R. Benarrouch, S. Wielandt, M. Anderson, A. Moin, A. Cathelin, and J. Rabaey, **"A Comparative Study of On-Body Radio-Frequency Links in the 420 MHz–2.4 GHz Range,"** Sensors, vol. 18, no. 12, p. 4165, 2018.

1.3 Manuscript Structure

This manuscript is organized into six main chapters. Chapter 2 presents this thesis' main objective. An overview of the different communication mechanisms available from the literature is provided, given the Human Intranet framework. A thorough analysis of Body Coupled Communication is proposed, detailing the three main coupling mechanisms: Magnetic, Galvanic, and Capacitive. Ultimately a comparison is conducted and the C-BCC has been selected as the preferred solutions.

Chapter 3 presents a deep analysis and full channel characterization on Capacitive Body Coupled Communication (C-BCC). A theoretical approach considering C-BCC electrodes as small dipoles is first introduced. A theoretical model is derived. Realistic electrodes are 3D-modeled and electromagnetic simulations are conducted. The theoretical and simulation results are then confronted. Those preliminary results are followed by a measurement campaign, conducted with laboratory instruments. A fully battery-powered prototype is developed, providing additional and realistic results. The characterization has led to a channel model and the operation frequency selection. Finally, a comparison with other existing communication solutions is presented.

Chapter 4 deals with network considerations. Different architectures are presented with their specificities. The Human Intranet skeleton is established given its requirements and the features offered by the reviewed topologies. IEEE communication protocol standards are presented and analyzed within the framework of the Human Intranet. The Wake-up receiver concept is presented and the corresponding power saving ability is detailed. Ultimately, a novel heartbeat-based synchronization scheme and the associated communication protocol is proposed.

Chapter 5 addresses a system-level approach and study on the heartbeat-based synchronization scheme introduced above. The system architecture is modeled along with each functional block's non-idealities. Three metrics are presented allowing for quantitative analysis. A duty-cycle approach is also detailed and as a reference in the final comparison on the heartbeat-based scheme's relevance with the Human Intranet.

The conclusion of this thesis is given in chapter 6 summarizing the research work within the Human Intranet framework and some future research perspectives are proposed.

2. State of the Art

Within this chapter, multiple communication options for building the Human Intranet are reviewed with a particular focus given on Body Coupled Communication (BCC). Ultimately, all communication techniques are compared leading to our preferred solution for this research work.

2.1 Communication options

This section aims at reviewing the main communication mechanisms, potential candidates to build the Human Intranet.

Wireless communication techniques are widely spread due to the number of connected objects continuously increasing. Are including in this category the following communication protocols: Bluetooth, BLE (Bluetooth Low Energy), WiFi (Wireless Fidelity), and ZigBee. All of the above are very similar as they are IEEE standards, operating in the same ISM frequency band of 2400 MHz (and 5 GHz for WiFi). They are extremely popular as their frequency of operation is unlicensed worldwide. WiFi communication standard is however excluded from review as it is not widely deployed for BAN and PAN applications due to its protocol overhead and associated power consumption, and higher output power. Wifi is more capable than the others in terms of data rate and covered range to the cost of higher power consumption and radiated power.

Classic RF communication propagates through the air enabling on-body and off-body communications. It offers a communication range up to 10 m, data rates up to 10's of megabit per second (3 Mbit/s for Bluetooth), and an output power rarely exceeding 10 dBm [28, 29]. Those protocols rely on narrowband communication with multiple channels available within the allocated bandwidth. Bluetooth offers 79 communication channels with a frequency-hoping spread spectrum, allowing the radio to switch channel during the transmission. It permits multiple devices to co-exist while homogenizing the bandwidth occupation. A lower power Bluetooth version has been created, BLE (Bluetooth Low Energy), to reduce the energy cost and overall communication delay [30]. The number of channels has been reduced to 40, including three broadcast dedicating ones, allowing better traffic handling and coexistence with other protocols such as WiFi. The maximum data rate has been reduced down to 1 Mbit/s. BLE also embeds an advertising/scanning capability allowing two nodes to trigger a data exchange while optimizing the power consumption. Contention techniques, such random advertising time offset or backoff strategy are implemented.

In [30], the authors propose a BLE extension to improve BLE's efficiency for deployments with a large number of nodes. The need for this extension relies on the fact that above 5 scanning devices listening for a tag's advertising message, the probability of success (to establish the link) starts decreasing significantly. Additional listening time can improve those results, granting more time for the different nodes to communicate and avoid a collision. Above 9 scanning nodes, the probability of communication success within a 5s-window after the advertising drops below 70%. Those results are the consequence of the limited number of advertising channels, in combination with a consequent number of nodes intending to communicate. While Bluetooth and BLE are offering great advantages in terms of off-body range, data rate, power consumption, and widely spread communication mechanism, its limitations regarding the communication latency due to node density could be problematic for building the Human Intranet.

Besides the BLE protocol limitations which could be addressed by reworking the stack, classic RF communications require a radiating element, commonly called an antenna. Antenna

design for on-body positioning is challenging for several reasons, especially for narrow-band communications. First, the antenna detuning and impedance variation must be considered. The human body shifts the antenna's operational frequency compared to free space tuning [31]. Such behavior is highlighted in figure 2.1 for a top-loaded antenna designed for the 2400 MHz band (represented in figure 2.1(a)). The S_{11} parameter was measured for three configurations: in the air (no body load), on the arm, and on the chest [2]. The body effect on the antenna tuning is clear, with higher insertion losses and a resonance frequency-shifted towards the lower part of the spectrum.

(a)   (b)
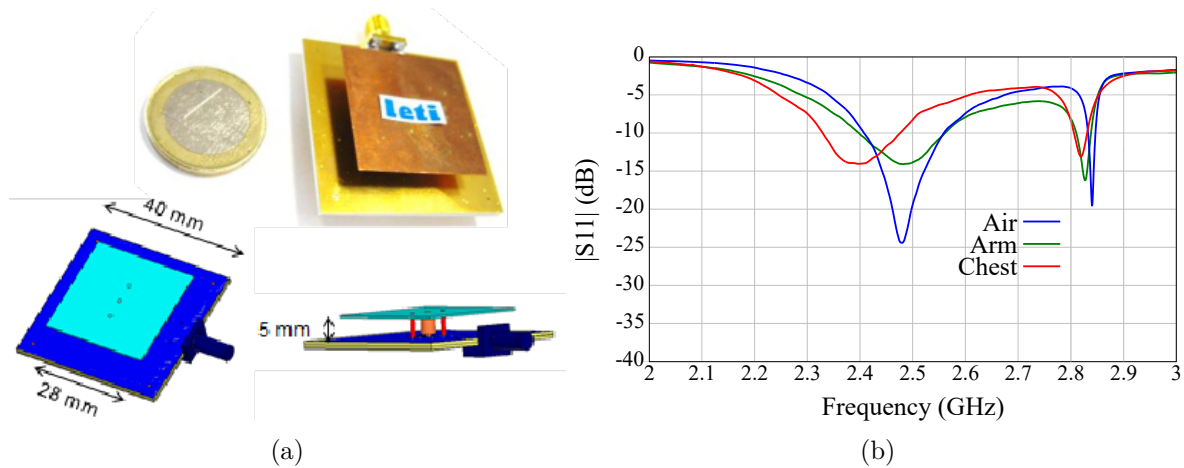
Figure 2.1: (a) Top loaded monopole design for the 2400 MHz band, (b) S_{11} in air and loaded on body: arm and chest. Taken from [2].

To compensate for the antenna detuning, multiple designs and techniques were studied. A reconfigurable antenna for on-body and off-body communication is presented in [32], optimizing the radiation pattern given the targeted type of communication. In [33], the authors have designed a patch antenna with a radiation pattern similar to a monopole antenna dedicated to BAN communications. While their design offers promising characteristics, its dimension is non-negligible: 62 mm in diameter, and a thickness of 5 mm. Despite a dedicated design, the antenna still suffers a slight detuning on-body but appears sensitive to variations in body-to-antenna spacing: up to 15 dB variation regarding the insertion loss and 300 MHz for the resonance frequency compared to free space.

Another challenge must be taken into account while considering classic RF communication around the body: the body-shadowing. The human body, due to its composition and associated dielectric properties, causes additional attenuation between communicating nodes [3]. The latter has been investigating in [3] with full-wave computer simulations using the FDTD method at 2450 MHz. A transmitter was located in front of the human model, at a distance a, while the receiver was located on the opposite side at a distance b. This scenario, along with the electric field (E-field) strength is presented in figure 2.2(a). The corresponding path loss is given in figure 2.2(b) for three source-body distance as a function of the receiver-to-body distance along with free space results (i.e. in line of sight without the human body in the communication path).

From figure 2.2(b), the body shadowing effect appears clearly, increasing the path loss by at least 6 dB. Furthermore, the source-body distance has a very limited impact while the body-to-receiver distance significantly impacts the extra attenuation. As the receiver gets closer to the body, it enters a deep E-field attenuation zone, increasing the path loss up to 25 dB for a global attenuation around 67 dB.

Ultra Wide Band (UWB) can be investigated as well. In [4], the authors focus their research on the 3-6 GHz band, while [34] studies the 60 GHz band with a bandwidth as large as 7-9 GHz. In UWB communication, the radiated power is spread over a wide spectrum which corresponds to short pulses in the time domain. This technique enables a very low transceiver's duty cy-
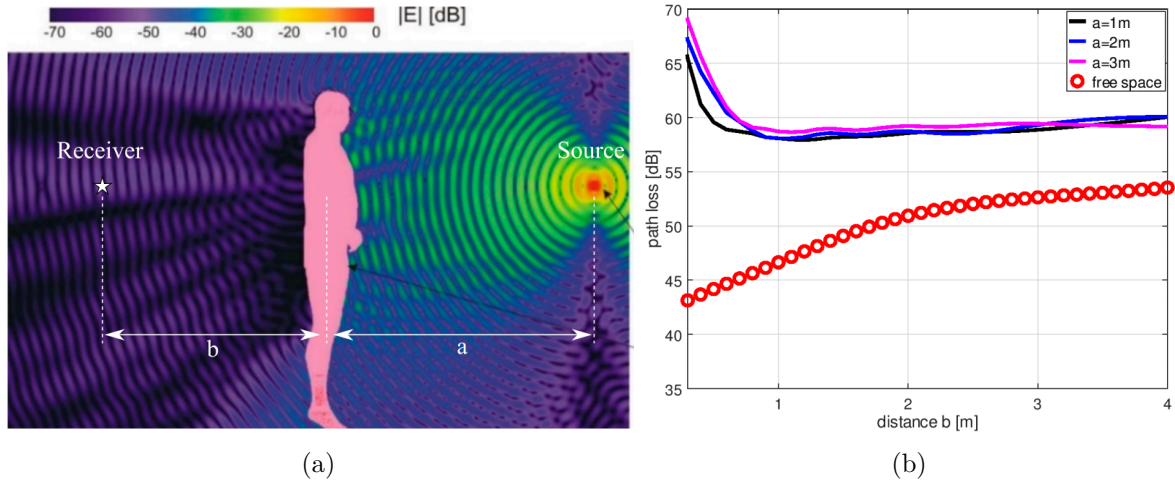
Figure 2.2: Body shadowing in the 2400 MHz band (a) E-field strength, (b) path loss for different source-receiver distance. Taken from [3].

cle, lowering the average power consumption and improving the overall energy efficiency [34]. Furthermore, a higher frequency of operation requires smaller radiating elements, lowering the node's form factor, improving the wearability [4, 34]. Those frequency bands on the higher part of the spectrum are less sensitive to interference due to lower global usage and the physical phenomena in place. A higher frequency of operation comes to the price of higher attenuation, increasing with the square of the frequency, limiting the detectable power at a distance-enhancing the communication's security level, but making the receiver design more challenging. Furthermore, a 60 GHz electromagnetic wave only penetrates around 0.5 mm within the human body, ensuring almost no effect on organs, but amplifying its sensibility to body shadowing (about 120 dB of attenuation from torso to back [34]). Figure 2.3 presents the attenuation results from [4]. A significant attenuation can be observed along with an important variance. Interesting results are reported in [34] regarding the path loss variations in regards to the body-antenna separation distance. On the one hand, the available bandwidth decreases with the separation distance, from 12.5 GHz while in contact to 5.5 GHz, 5 mm apart, while on the other hand, the total efficiency soars from 28.85% to 59.31% while in contact and 5 mm apart respectively. This significant global efficiency variation is coherent with the body shadowing effect introduced earlier.
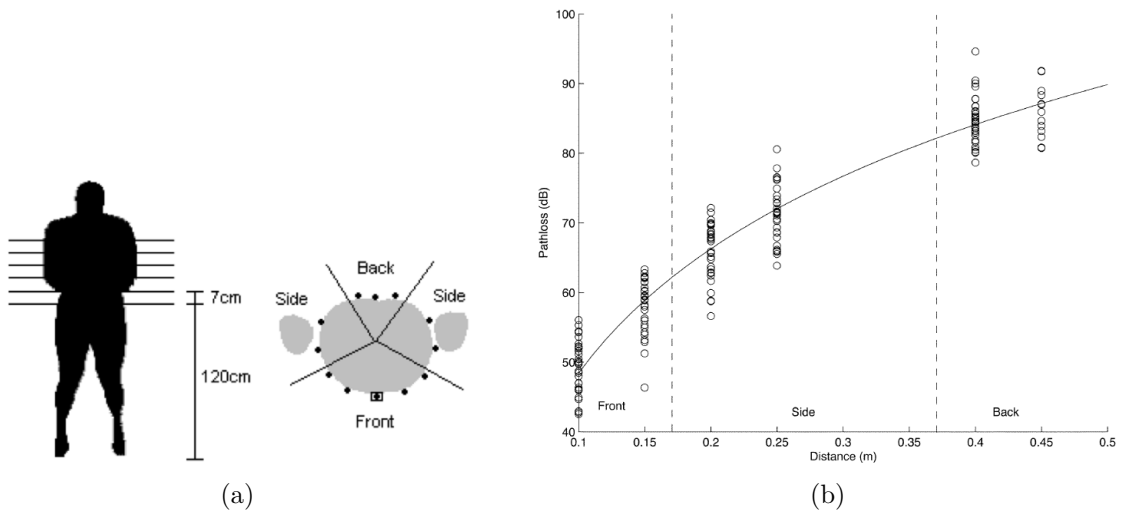
Figure 2.3: UWB (3-6 GHz) path loss measurement, (a) antenna location on body, (b) measured path loss. Taken from [4].

Wireless RF communications follow two type of regulations: (i) the regulation managing the

usable spectrum for a given frequency, with the maximum radiated power in band and out of band, and (ii) the regulation regarding the radiated power within the vicinity of a human body and the maximum absorption allowed. We are focussing here on the second type.

The FCC edited guidelines regarding the human exposure to radiofrequency electromagnetic fields [5]. The Specific Absorption Rate (SAR) is defined as the rate at which RF energy is actually absorbed in a body. In [35], it is stated that: "In the case of exposure of the whole body, a standing ungrounded human adult absorbs RF energy at a maximum rate when the frequency of the RF radiation is in the range of about 70 MHz. This means that the "whole-body" SAR is at a maximum under these conditions. Because of this "resonance" phenomenon and consideration of children and grounded adults, RF safety standards are generally most restrictive in the frequency range of about 30 to 300 MHz."

Consequently, the FCC defined the "limits for Maximum Permissible Exposure (MPE)" in [5], from 300 kHz to 100 GHz as presented in figure 2.4. Within this figures, two curves are presented, the dashed is the one that matters as it "applies to human exposure to RF fields when the general public is exposed or in which persons who are exposed as a consequence of their employment may not be made fully aware of the potential for exposure or cannot exercise control over their exposure. Therefore, members of the general public always fall under this category when exposure is not employment-related." [5]. Ultimately, the maximum exposure is established by averaging the power density over a period of 6 minutes as stated in [5].
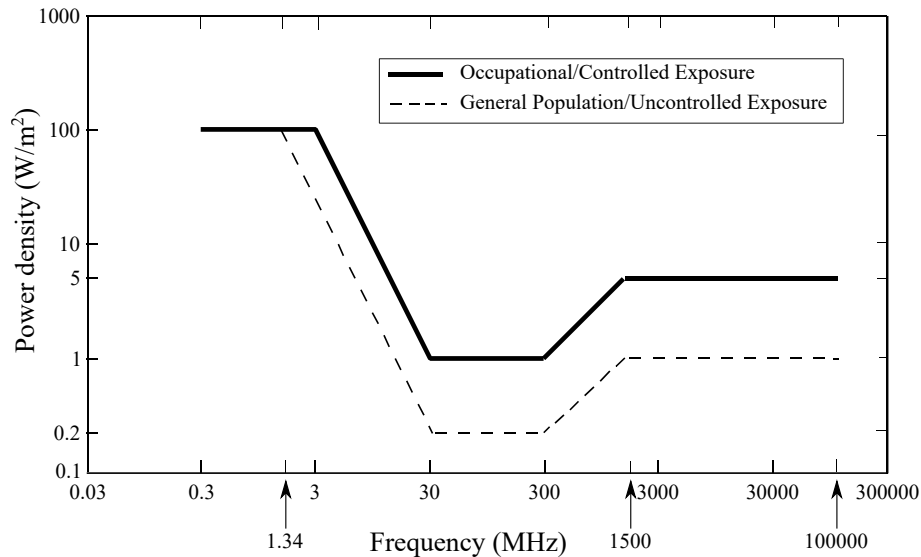
Figure 2.4: FCC limits for Maximum Permissible Exposure (MPE). Taken from [5].

It is mandatory, for safety purposes to follow the limitation stated above. Local regulations might differ from the FCC but they all refer to the same power density and SAR.

The last communication technique that maybe considered here is ultrasonic communication. Ultrasounds are acoustic waves above 20 kHz, non-audible for humans. Ultrasounds propagate very well in an aqueous solution with limited path loss. The human body is mostly composed of water, around 65% [36, 37], giving ultrasound communication a great advantage.

Generating ultrasounds follows the same principle as audio speakers (as both are acoustic waves). The electric signal must be converted into a mechanical deformation. The ultrasonic is somewhat, equivalent to the radiating element (i.e. antenna) for classic RF communication. Human ultrasonic communication usually operates at frequencies of a few hundreds of kilohertz. Alike electromagnetic waves higher frequencies face higher attenuation. Consequently, the signal's frequency should not exceed 10 MHz [38].

In [37], the authors have successfully achieved the transmission of a continuous wave throughout a meat sample. The frequency of excitation was set to 300 kHz and an attenuation of 9 dB

over 15 cm in the human body has been reported. However, given the inhomogeneity of the human body, ultrasound propagation can suffer multipath and destructive interferences [38].

To address this issue, ultrasonic short pulses are used to benefit from the resulting wideband behavior [39]. Combined with a custom MAC layer, the authors proposed a multi-path resilient ultrasonic solution, associating a pseudo-random adaptive time-hoping ultrasonic pulses pattern with an adaptive spreading code [38]. Another technique presented in [38], consists of implementing an OFDM (Orthogonal Frequency-Division Multiplexing) communication scheme, benefiting from the complex signal encoding and spread over orthogonal frequencies to reduce the inter-symbol interference resulting from the multipath propagation. A data rate of 28.12 Mbit/s has been demonstrated in [38].

Although ultrasonic communication brings interesting characteristics regarding its ability to propagate a signal through the human body, it faces an important drawback in its implementation. Complex (and thus energy consuming) algorithm are required to mitigate the multipath propagation. Ultrasound transceivers are not negligible in terms of form factor, could suffer path loss variation if their connection to the body changes (extra layers and interfaces added in the communication channel). Ultimately, the transceiver directivity could also be problematic for implementing the Human Intranet.

Besides all the above communication techniques, it exists a mechanism called Body Coupled Communication (BCC), taking advantage of the human body characteristics to establish communication. It is presented in-depth within the following section.

2.2 Body Coupled Communication State of the Art

Body Coupled Communication (BCC) consists of using the human body as a communication medium, carrying the signal, and associated data. The three mains BCC mechanisms are Galvanic, Magnetic Resonance, and Capacitive coupling. They are introduced with their principle, as well as a few relevant examples of modeling and implementation from the state-of-the-art within this section.

2.2.1 Magnetic Coupling

Magnetic Body Coupled Communication (M-BCC) consists of at least a coil on the transmitter's (Tx) end. When a current flows through the inductor, a magnetic field is generated. On the receiver's (Rx) side, two configurations can be observed. Either the considered subject must interact with its environment by touching dedicated spots, electrically closing the Rx loop which senses the current induced from Tx [6]. This configuration is depicted in figure 2.5(a). The other option relies on a second coil on the Rx side converting the generated magnetic field into a current [7,8], as pictured in figure 2.5(b).

(a)   (b)
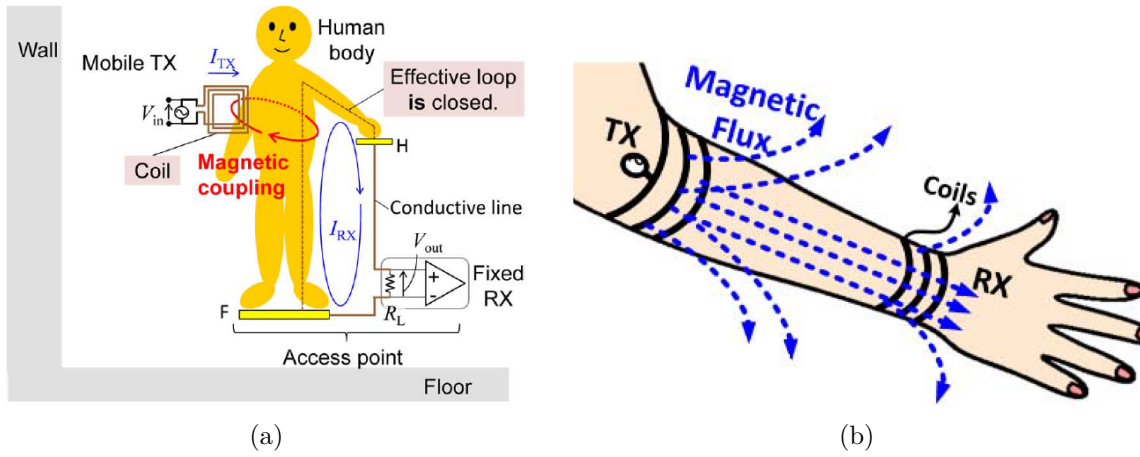
Figure 2.5: M-BCC principle (a) with a single coil, (b) with a double-coil. Taken from [6] and [7].

The single-coil configuration, regardless of the number of potential applications, does not suit very well within the framework of the Human Intranet due to its infrastructure requirements and immobility. On the other hand, the double-inductor approach makes this communication fully wearable.

To improve the channel characteristics and lower the impact of the wearer surroundings, M-BCC should operate with a quasi-static magnetic field. A magnetic field is considered magnetostatic if the equation (2.1) is satisfied [6,8].

$$d << \frac{c}{2\pi f} \tag{2.1}$$

where d is the distance between both coils, c the speed of light, and f the frequency of operation.

Consequently, a frequency in the megahertz range is usually considered. The coil size is chosen accordingly, a 6.73 cm square in shape inductor with a maximum operating frequency of 20 MHz is reported in [8]. Their measurement results are presented in figure 2.6 over frequency for a range of 1 m. One can observe the tight relationship between the skin-coil separation distance and the attenuation: the greater is the separation distance, the more important is the path loss. Therefore, M-BCC is sensitive to the coil movement relative to the human body. This point was also highlighted in [7] for inductors wrapped around a limb. To maximize energy efficiency, the frequency of excitation is chosen such as it corresponds to the resonance frequency.

Body motion could detune the coil, making the system operating off-resonance, reducing the efficiency, the covered range, and increasing the attenuation.
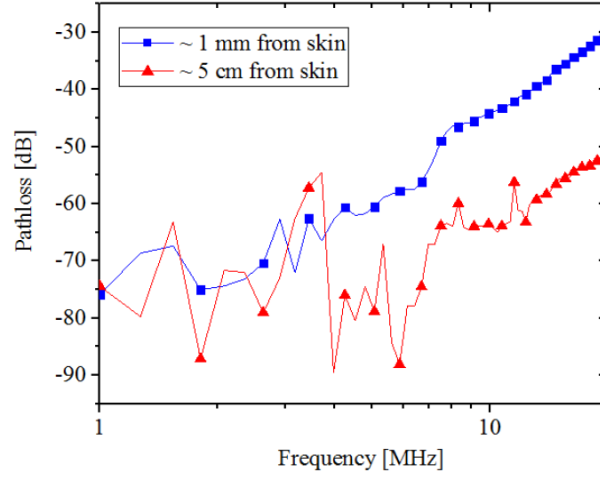
Figure 2.6: M-BCC measured attenuation for two skin-coil separation distance. Taken from [8].

Electromagnetic simulations are conducted in [9] where a human arm is modeled as a cylinder with muscle dielectric properties. Two coils are wrapped around the arm model, 32.5 cm apart, with a frequency of excitation of 64.7 MHz. The path loss is simulated for several arm bending angles, from 0° (straight arm) to 135°, and reported as the transmission parameter S_{21}. We can observe from figure 2.7(a) that the magnetic field is mostly confined around the transmitting coil and limited propagation is taking place on a straight arm. In the latter configuration an attenuation of -29 dB is reported (see figure 2.7(c)). The path loss sees limited variation for bending angles from 0° to 60°. As the bending angle increases, the Rx coil gets closer to the source, improving the channel losses by 10 dB at 135°. This analysis shows a limited coupling with the human body but offers a better channel gain in the case of bent limbs. The attenuation reported is better than the results presented in figure 2.6 from [8] where the communication range is three times larger.
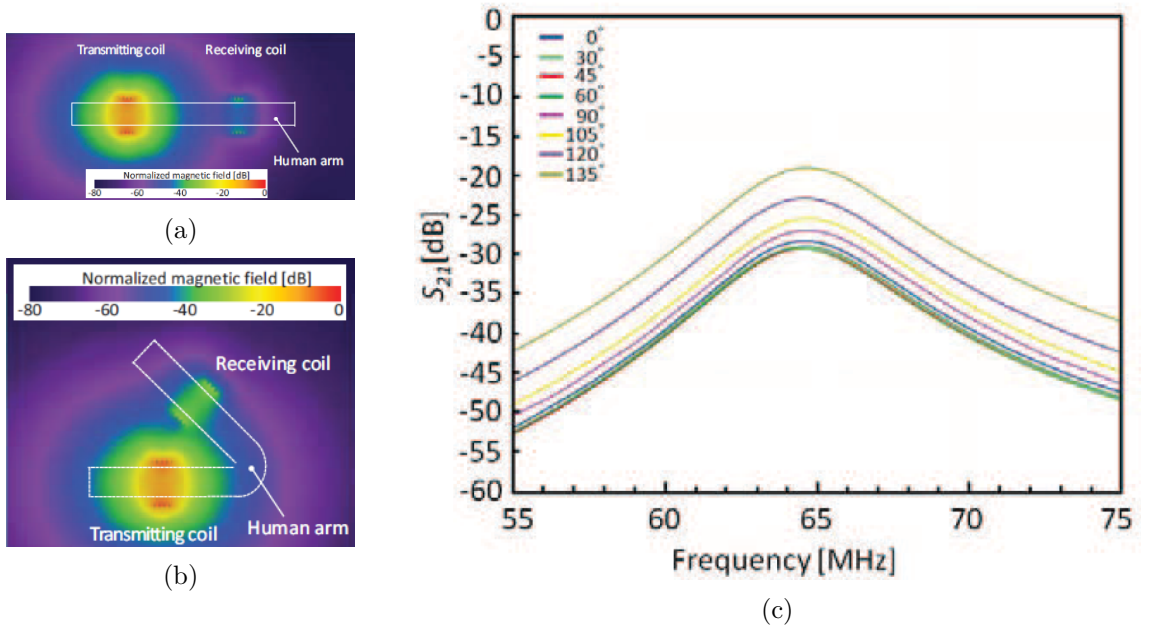
Figure 2.7: M-BCC electromagnetic simulation results (a) straight arm, (b) 135° bent arm, (c) attenuation. Taken from [9].

M-BCC offers interesting attenuation results over distances larger than one meter. The coils

are rather bulky as the frequency of operation must be in the megahertz range. Ultimately, the coil's position, relative to the body, induces important variations in the channel loss.

2.2.2 Galvanic Coupling

Galvanic Body Coupled Communication (G-BCC) consists of two pairs of electrodes on both ends (Tx and Rx). Each electrode pair must be connected to the human body. A differential signal is applied on the transmitter inducing a current galvanically coupled to the human body and flowing through the upper layer of the skin [7, 10, 40]. The G-BCC principle is illustrated in figure 2.8.
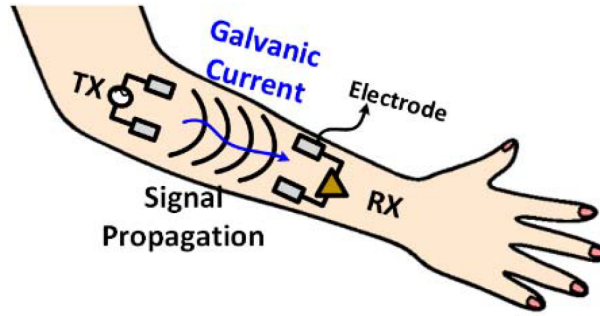
Figure 2.8: Galvanic coupling principle. Taken from [7].

G-BCC can be operated following two approaches: (i) constant voltage applied across the electrodes, or (ii) constant current flowing between the electrode set on the Tx side. As always, interfacing the body with a set of electrodes means to deal with the electrode impedance and their associated variation. Consequently, a constant voltage approach suffers from the electrode-skin attachment quality [40]. However, even with a constant current method, differences can be observed from one electrode reference to another [10].

Similar equivalent electrical circuit model are established in [10, 12, 40] as presented in figure 2.9. Modeling the channel is important to predict the behavior over frequency or distance for instance but also to make sure all phenomena involved in the communication mechanism are properly identified and understood.
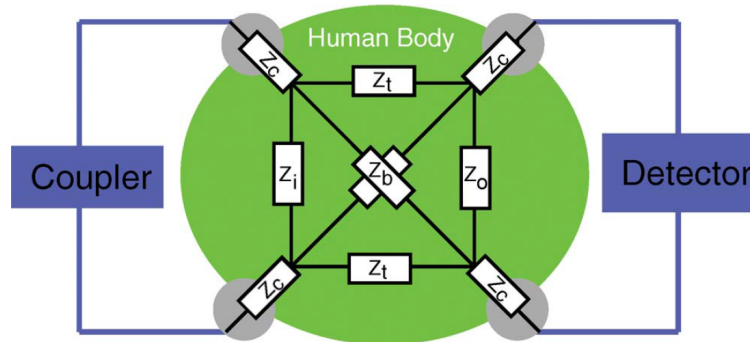
Figure 2.9: GBCC equivalent electrical circuit model, with Z_c the electrode's impedance; Z_i and Z_o the transmitter and receiver output/input impedance respectively; and Z_t and Z_b the channel impedance (longitudinal and crossed). Taken from [10].

In the above representation, both electrode potential references are distinct. It makes sense given the targeted applications, with nodes meant to be battery powered. However, splitting the grounds with laboratory equipment can be quite challenging as they are all connected to the earth ground. In [10], a smart "optobridge" interfaces the computer with the battery-powered prototype allowing full control on the communication. The measurements are performed for frequencies below 1 MHz. On the other hand, [40] interconnects a pair of balun on both Tx and Rx leads.

Two types of measurements, on the biceps and from hips to hip, with three electrodes reference were conducted in [10] as represented in figure 2.10(a). One can observe that the electrode-type matters, even with a constant-current approach. The blue curve suffers from a higher attenuation than the two others in the same scenario. As expected, the path loss increases with distance with similar additional losses for all three references. Ultimately, the gain increases with frequency for all to reach a kind of plateau from 700 kHz to 1 MHz. Figure 2.10(b) plots the attenuation for four electrode-size combinations: F11: 560 mm^2 for Tx & Rx, F21: Tx=280 mm^2 & Rx=560 mm^2, F41: Tx=560 mm^2 & Rx=140 mm^2, and F44: 140 mm^2 for both. A greater electrode surface enables a lower attenuation. Along with those plots are presented the simulation results based on the channel model from figure 2.9. The fit is accurate for the intermediate-range and predicts an optimal path loss at 700 kHz and at least 36 dB of attenuation.
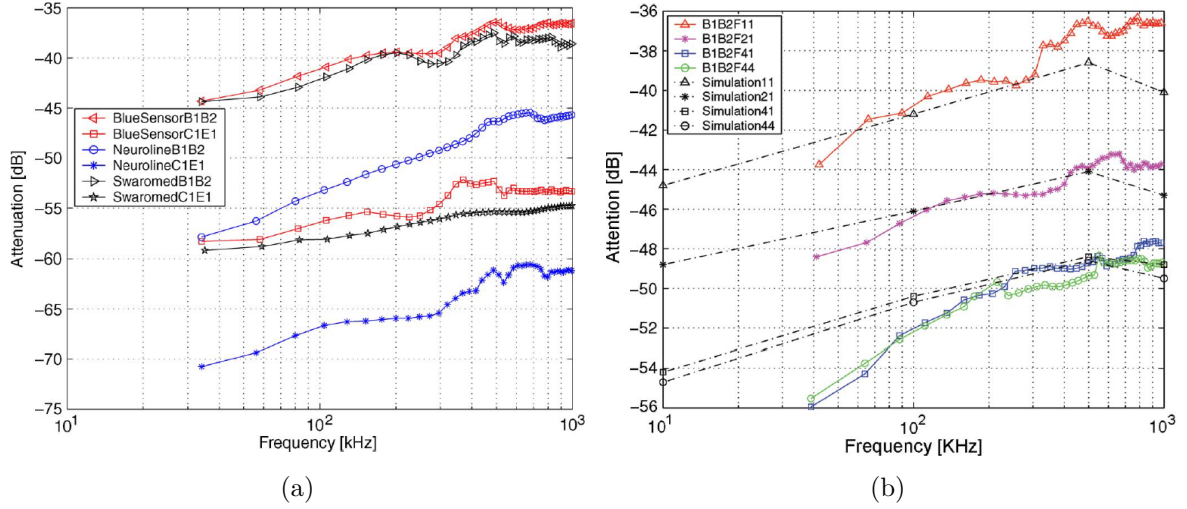
Figure 2.10: G-BCC attenuation (a) for three different type of electrodes, (b) for four electrode-size combinations along with model predictions. Taken from [10].

FEM simulation from 100 kHz to 10 MHz were conducted on a five-layer human arm model and reported in [41]. Those results are well aligned in terms of behavior frequency in [10], with an optimum around 3 MHz. However, much lower path loss is reported (around -12 dB) and only a tiny difference can be observed over distance between 10 cm and 30 cm.

In [11], the authors follow an electromagnetic analysis to study the propagation mechanisms involved and define the frequencies of operation allowing a wave to stay confined within the skin layer. A three-layer model is considered, including muscle, fat, and skin, lying in the air as represented in figure 2.11(a). For an EM wave to exist and propagate within the skin layer, a propagation mode must exist. In other words, the frequency of excitation must be above the "cut-off frequency" below which the boundary equations have no solution. Regarding this matter, the skin thickness plays a major role as it defines the propagation layer's geometry and is directly linked to the minimum operating frequency as depicted in figure 2.11(b).

Those frequencies of operation guarantee a better wave confinement within the skin layer to the cost of an important attenuation per unit of distance as expected with higher frequencies. From figures 2.12(a) and 2.12(b) it is clear that the wave is more confined with a higher frequency of excitation to cost of much shorter propagation range.

An implementation example is given in [12]. The communication between a smart wrist band and a smartphone is achieved, relying on G-BCC with a frequency of operation of 200 kHz for a data rate of 100 kbit/s. The authors use the balun technique to insulate both grounds. The resulting channel loss is presented in figure 2.13(b).

G-BCC enables a high level of confinement regarding the propagating EM wave of interest.

(a)   (b)
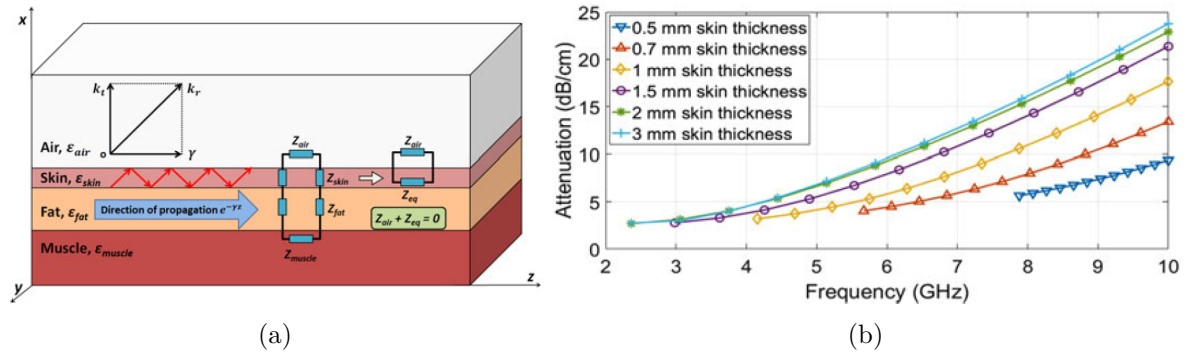
Figure 2.11: EM skin confined analysis, (a) four-layer model, (b) TE modes and their associated attenuation for multiple skin thickness. Taken from [11].

(a)   (b)
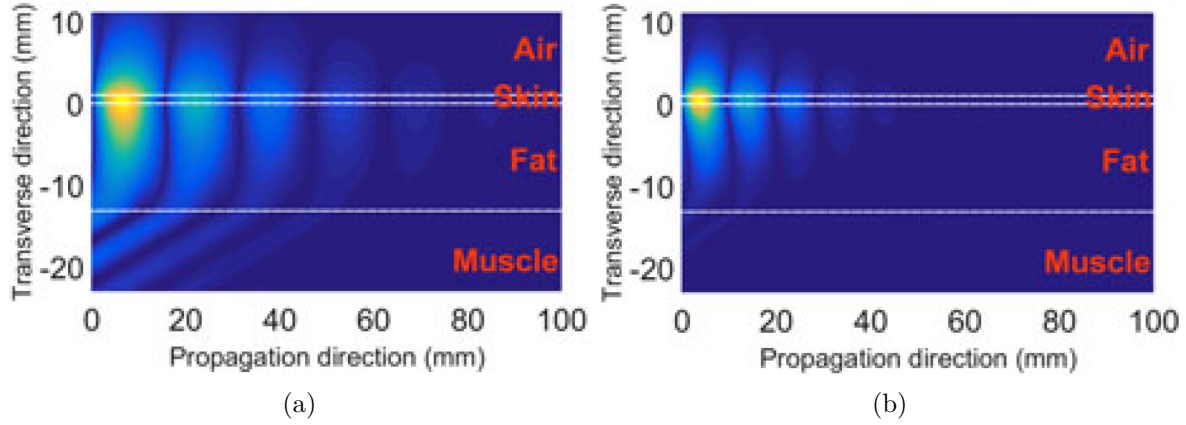
Figure 2.12: Power distributions of TE fundamental mode for the 1 mm thick skin and 13 mm thick fat model, (a) at 4 GHz, (b) at 6 GHz. Taken from [11].

(a)   (b)
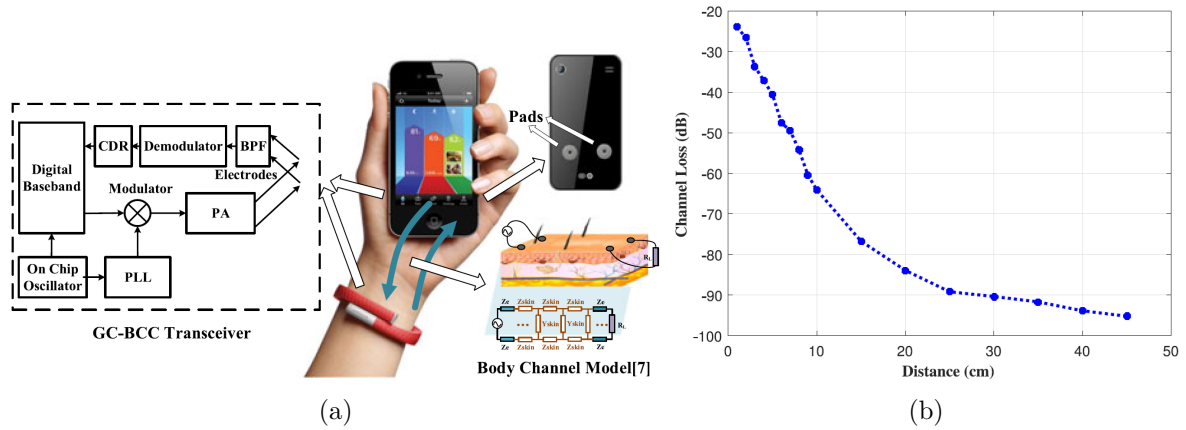
Figure 2.13: G-BCC prototype, (a) system principle, (b) measured attenuation over distance. Taken from [12].

It has been proven sensitive to the electrode-skin interface and its corresponding impedance, significantly impacting the resulting path loss. Thorough EM analysis showed a high cut-off frequency to guarantee minimal power radiated in the air. Ultimately, G-BCC suffers high losses per unit of distance, with a practical limit of a few centimeters.

2.2.3 Capacitive Coupling

Capacitive Body Coupled Communication (C-BCC) consists of an electrode pair on both transmitter (Tx) and receiver (Rx). One connects the signal to transmit or receive to the body while the second serves as a reference and is also called the "ground electrode". This principle

is presented in figure 2.14(a) as exposed in [13] for the first time in 1995.
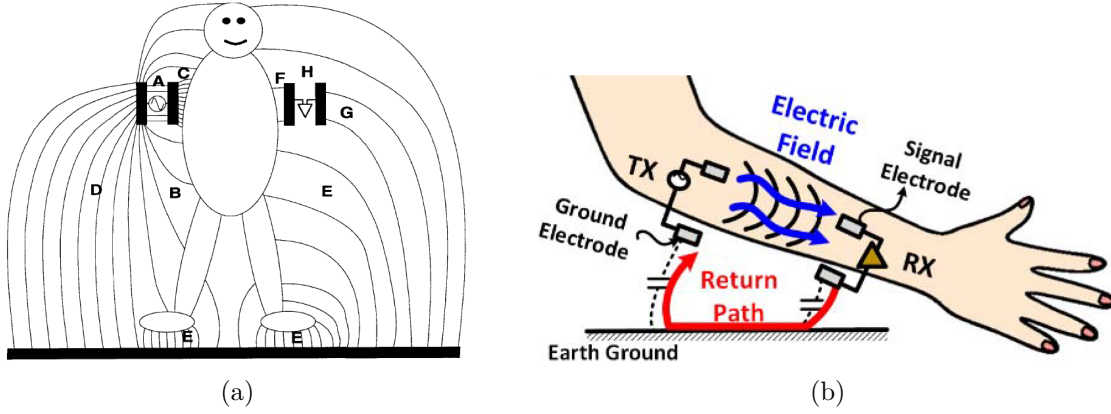
Figure 2.14: Capacitive coupling principle, (a) as introduced in [13] by T. G. Zimmerman, (b) highlighting the "return path", taken from [7].

This mechanism is called "capacitive coupling" as both ends are capacitively coupled to the human body. The electrical potential generated on the transmitter is detected on the receiver. For this non-radiating perturbation to flow through to the human body, a "return path" is mandatory to "close the circuit". The latter is formed by the air and the earth ground [13], as depicting in figure 2.14(b). From here, C-BCC has been extensively studied following those two main aspects: the coupling to the body and the return path (coupling to the earth ground). It must be noted that this behavioral representation was the reference when this research began and has only been adjusted recently (March 2019) in Nature Scientific Reports [42].

The return path study has drawn a lot of attention as is it a very variable, yet crucial parameter within the C-BCC mechanism. In [16], the link between the communication range and the channel loss has been demonstrated, due to a resistance increase of both couplings: with the body and the external ground. The authors also state that the return path is frequency dependent: higher frequencies are facing a lower effect from the return path but the body impedance becomes more important. In [14], the authors also state that the total transmission loss is dominated by the ground electrode coupling strength due to its larger impedance compared to the forward path.

In [43], the authors split the communication between the forward path, which corresponds to the signal propagating within the body, and the return path referred to as the "extrinsic part". The latter is split into three distinct capacitances: (i) from the ground electrode to the ground plane, (ii) from ground-to-ground electrodes (from Tx to Rx), and (iii) from the body to the ground plane. It was shown that the cross-coupling between electrodes cannot be neglected for short distances. From their investigation, the return path from the electrode ground plane to the earth ground is at least ten times larger.

Given the significant role of the return path in C-BCC, the ground plane size and shape as well as the electrode design have been investigated. It is shown in [43] that a greater ground plane size brings a higher ground coupling capacitance. For instance, a 5×5 cm electrode provides a $4.5\,\mathrm{pF}$ capacitance, 1 cm from the ground while a 2×2 cm ground plane only offer about $1\,\mathrm{pF}$ capacitance under the same condition. This difference decreases with the distance from the ground. While the ground capacitance of the smaller electrode stays almost constant with the height from the ground, the bigger design sees its capacitance decreasing down to $2\,\mathrm{pF}$. The investigation conducted in [14] confirms the above results, with an important cross-coupling for short-range (below 5 cm), which decreases exponentially with distance. The attenuation measured and simulated is then very similar for a transmission distance from 10 cm to 30 cm. The authors mathematically express the cross-coupling capacitance C_{cc} given in equation (2.2)

$$C_{cc} = \left[1 + 1.3105 \left(\frac{d}{l}\right)^{0.1075}\right] \frac{\epsilon_0 \epsilon_r S}{d} \qquad (2.2)$$

where ϵ_0 is the vacuum permittivity, ϵ_r is the dielectric relative permittivity, S the ground electrode surface, l is the ground electrode side length, and d the inter-electrode distance. [14] also studies the ground-to-electrode distance and its consequences on the ground electrode coupling capacitance with the external ground. It decreases exponentially to reach a plateau for heights above 50 cm. Similarly, they express the corresponding capacitance C_{gnd} given in (2.3)

$$C_{gnd} = 2 \left[1 + 3.1124 \left(\frac{2h}{l}\right)^{0.9691}\right] \frac{\epsilon_0 \epsilon_r S}{2h} \qquad (2.3)$$

where h is the ground electrode height from the ground.

Larger electrodes increase the channel coupling lowering the return path impedance [43], while smaller electrodes are offering a more consistent behavior and a more convenient form factor. In [14], the electrode's size is thoroughly studied with three different square ground electrode sizes. The frequency band of interest ranges from 1 MHz to 40 MHz. Increasing the ground electrode area improves the path loss. In their investigation, a 10×10 cm electrode offers a lower attenuation by 5 dB to 6 dB compared to a 4×4 cm electrode as depicted in figure 2.15 (taken from [14]). Ultimately, the authors also specify that a larger electrode will however increase the body load. A trade-off between both must be considered. Those observations were reported in [16] with a similar electrode, lower losses were measured with bigger electrodes, especially for a higher frequency of operation, up to 150 MHz.
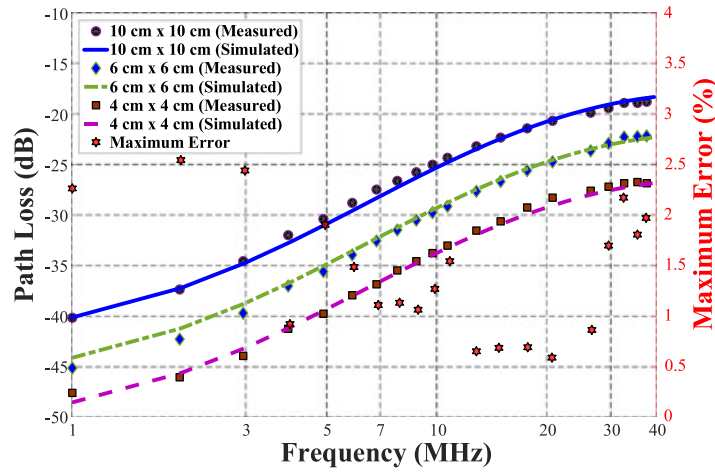
Figure 2.15: Path loss for several ground electrode size, taken from [14].

Three different electrode shapes have also been investigated in [14]: a triangle, a hexagon, and a circle. The electrode shape also plays an important role as the hexagonal electrode provides the best path loss while the circular one results in the highest path loss. Those results are confirmed by simulation in [14] and are justified by the electrode's edges improving the channel gain.

The electrode structure and the signal electrode position relative to the ground electrode is another degree of freedom and variability. As detailed in [15], their structure could either be horizontal or vertical. When positioned horizontally (see figure 2.16(a)), both electrodes a juxtaposed with a dielectric material keeping the conductive parts apart from one another. With such a structure, the electrode could also be oriented longitudinally, where the longest edge is parallel to the intended direction of communication. Oriented transversely (see figure 2.16(b)), their main dimension is perpendicular to the communication direction. The vertical structure

consists of both conductive plates stacked on top of each other with a dielectric layer used for insulation. Both structures are represented in figure 2.16.
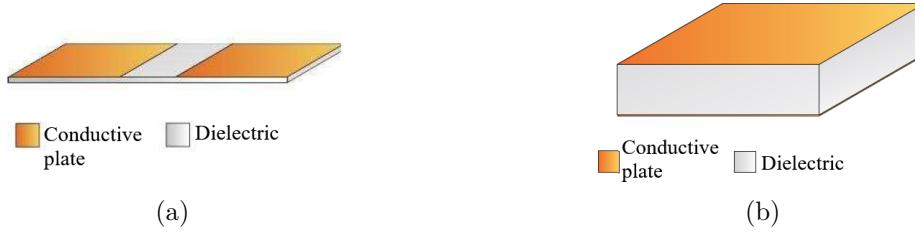
Figure 2.16: Electrode structure: (a) Horizontal, and (b) vertical. Taken from [15].

Alternative configurations and implementation can be observed. In [44], a medical electrode is used as the signal electrode, ensuring firm contact with the body while the ground electrode is benefiting from the PCB ground plane from their implemented prototype.

Measuring the channel's path loss is challenging due to the communication dependence on the return path. Directly connecting the electrodes to the laboratory instruments would shorten the return path with the instrument's connection to the earth ground. The topic is addressed in [45] where the authors highlight the effects of the grounded equipment on the measured path loss. Performed under the same conditions, the attenuation observed on the battery-powered set-up is greater than with the plugged instruments. The difference decreases with frequency, from 90 dB at 10 MHz to 30 dB at 150 MHz. This difference cannot be ignored and must be taken into account while performing channel loss measurements. In the reported work, two configurations are observed to tackle the issue. The first one consists of having one node (usually the transmitter) battery-powered while the other is connected to grounded equipment [17]. The second option interconnects a pair of baluns in between the electrodes and the laboratory instrument [14]. With both configurations, the equipment's ground plane size could impact the measurement in addition to their proximity to one another.
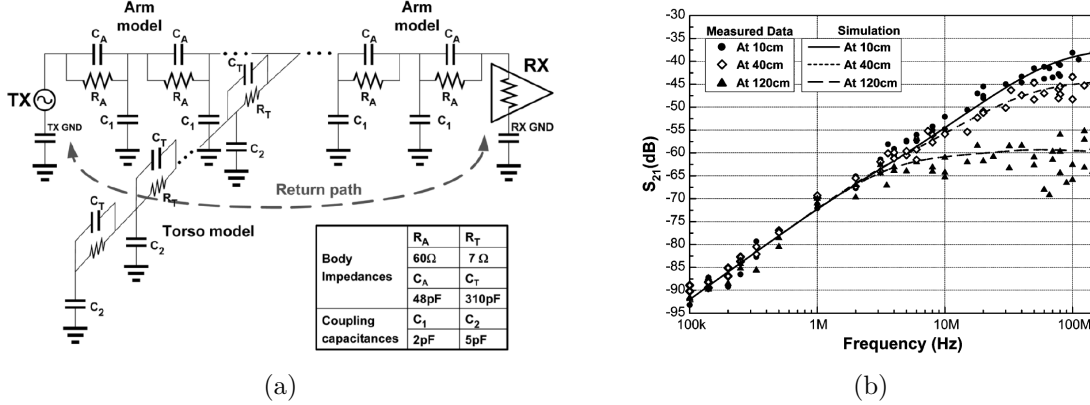
Figure 2.17: (a) C-BCC channel electrical model, and (b) comparison between the simulated model and measurement results. Taken from [16]

The capacitive body channel has been electrically represented following a distributed R-C model such a the example is given in figure 2.17(a) [16, 43]. Those models give fairly accurate results in comparison with the measurements as presented in figure 2.17(b). The frequency of interest in those studies never exceeds 150 MHz.

In addition to the electrical model, the communication channel can also be modeled following a path loss approach. In [15] the authors rely on measurement results to define the channel gain. Their work reports an increasing attenuation with frequency and the transmitter-receiver distance. A general path loss model is expressed, highlighting two specific behaviors: (i) a flat attenuation A below the cut-off frequency f_c, and (ii) a linear attenuation following a coefficient

B. Their model is given in equation (2.4). The model's coefficients are adjusted according to the measurement results plotted in figure 2.18 over frequency from 1 MHz to 60 MHz.

$$L_p(f) = \begin{cases} A & f < f_c \\ A + B(f - f_c) & f \ge f_c \end{cases} \tag{2.4}$$
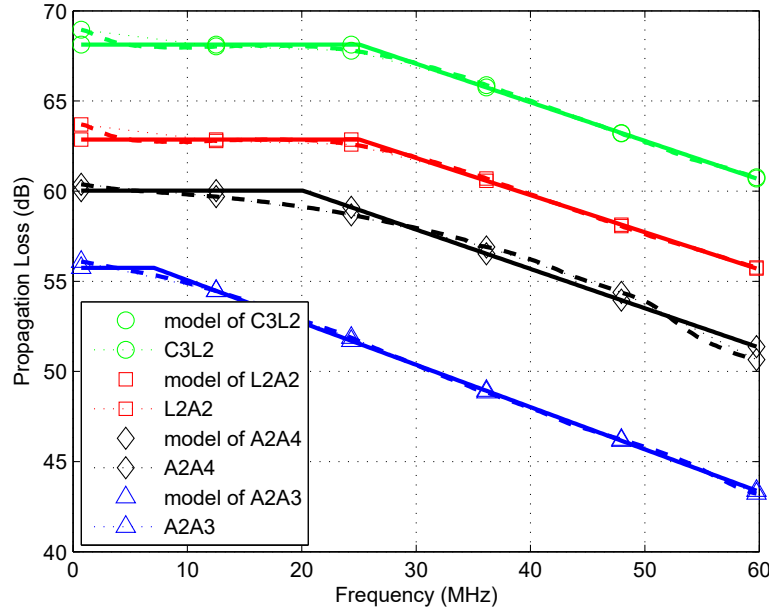
Figure 2.18: C-BCC path for multiple distances and locations, model and measurements, taken from [15].

In [17] the authors also aim at defining the channel attenuation by calculated the resulting electric field at a distance r from the source. To develop their theoretical expressions, the human is considered as a conductive surface and the electrodes as a small dipole. This approach highlights a combination of three phenomena: (i) surface wave propagation, (ii) reactive induction field, and (iii) the quasi-static near field coupling. All three depend on the communication range and the frequency of operation (among others). Their contribution over frequency for a fixed distance of 1 meter is given in figure 3.2. The path loss was then measured over distance for three frequencies of operation: 1 MHz, 33 MHz, 80 MHz as reported in figure 2.19(b).

For very low frequency (1 MHz) the attenuation stays relatively constant. The quasi-static coupling is dominant. For higher frequency (80 MHz), the attenuation seems linear over distance as the surface waves are the dominant propagation mechanism. For intermediate frequency (33 MHz), a change in the attenuation slopes corresponds to the dominant regime change.

While C-BCC is often presented as a mean to establish the communication link between two devices on the human body surface, intra-body communication capabilities have been demonstrated in [18]. In figure 2.14(a) the capacitive coupling between the electrodes and the body as well as with the earth ground is represented as a phenomenon external to the human body. The electric field radiated from the source also penetrates the human tissues. In such a situation, the outer layer of the human body is operating as a ground electrode, capacitively coupled to the earth ground as modeled in [43]. This specificity is exploited in [18] to communicate between two implanted devices by the mean of C-BCC as depicted figure 2.20. The authors report coherent simulation and measurement results.

Through those reported work C-BCC has been shown as a sensitive communication mechanism. First, the return path studied in [7, 14, 16, 43], in particular its impedance, mostly made of the capacitance formed between the ground electrode and the earth ground, changes with the body movement. Such observation is made while performing the measurement, as in [17]. A
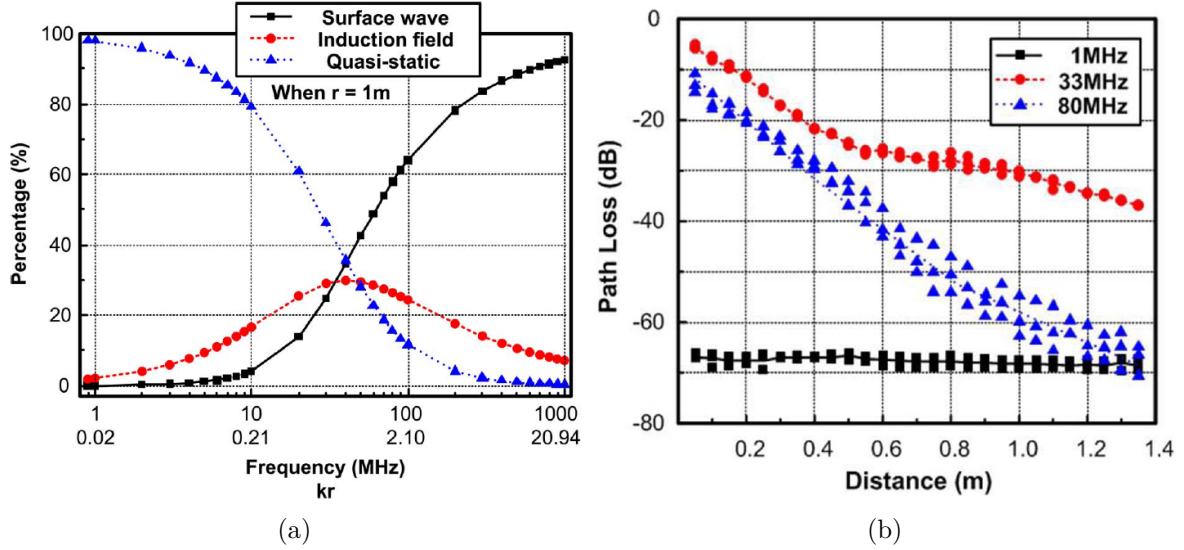
Figure 2.19: (a) C-BCC mechanism contribution ratio, and (b) measured path loss for multiple frequencies. Taken from [17].
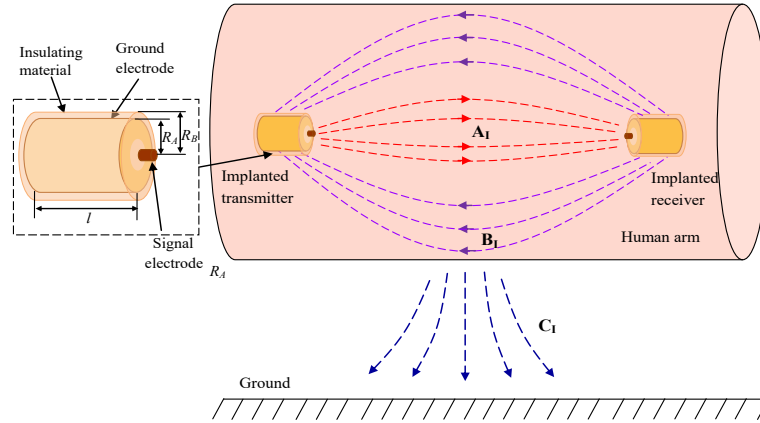
Figure 2.20: C-BCC principle for intra-body communication, taken from [18].

classic environment like an open space is very noisy, deteriorating the communication channel as depicted in [15]. Also, as the radiation is not contained with the human body, a direct RF path (through the air), defined as a special path in [17] can form the main communication channel. Again, with body movement, the phenomena can compete with C-BCC, directly impacting the channel characteristic and the resulting attenuation. Ultimately, if surface waves are the dominant propagation phenomenon, constructive and destructive interference could take place, degrading the path loss.

Several prototypes implementing C-BCC as their communication mechanism have been reported in the state of the art. In [46], the authors tackle the return path variability by designing a self-adaptive compensation technique. The idea is to control a tunable inductor to resonate with the return path's equivalent capacitor and compensate for the associated path loss. They report the channel gain improvement by 9 dB to 16 dB over a range from 1 cm to 10 cm for a frequency range below 100 MHz.

An interesting study aiming at adapting the RFID tag concept led the author in [47] to explore the energy harvesting possibilities with C-BCC. They developed a battery-less body-worn receiver capable of harvesting energy from a tag. To compensate for the channel loss, a variable number of rectifier stages can be enabled, setting the sensitivity and the charging output voltage. They achieve up to 56% Power Conversion Efficiency (PCE) at 13.56 MHz. As the palm is used as the contact point with the reader, the equivalent electrode's size is much

bigger than any other prototype, improving the coupling.

The work reported in [48] is very promising in the Human Intranet context as it reports one of the best energy efficiency of 79 pJ/bit and offers two data rate: 80 Mbit/s (BPSK modulation) and 100 kbit/s (OOK modulation) with full-duplex capability. To achieve such energy efficiency, the authors combine two frequency bands: 20-60 MHz and 140-180 MHz, avoiding major interferers in-between. Those frequency bands are re-used in [49], implementing a capsule endoscope. The data are transmitted from within the human body following the principle detailed in [18]. The transmitter achieves a cutting edge energy efficiency as low as 22 pJ/bit but heavily relies on the external receiver capabilities, which consist of eight nodes. The communication is asymmetric as it is only meant to go from the inner to the outer node.

Ultimately, the work reported in [44], proposes an IEEE 802.15.4 standard compatible HBC communication. The authors' focus was to tightly follow the radiation mask imposed within the standard as well as the frequency of operation centered on 21 MHz and the communication rate in the range from 656 kcps to 5.25 Mcps ("cps" stands for "Chips per Second" with a spreading factor (FS) of 8 for HBC as defined in the IEEE standard). The digitally controlled transceiver achieves a -72 dBm sensitivity and communication from the torso to the wrist are reported successful. Medical pre-gelled electrodes are used as the signal electrode while the prototype's ground plane (i.e. PCB ground plane) is acting as the ground electrode.

At this point, the state-of-the-art on C-BCC has been focusing on the frequency of operation below 200 MHz, assuming that the representation given in figure 2.14(a) is correct. It drove most of the attention on understanding, modeling, and mitigating the return path sensitivity and variation. The electrical circuit model, electromagnetic studies, and channel loss profile were defined. Additional measurements were conducted with the necessary care to split the grounds. Several prototypes were also implemented and promising results were reported.

2.2.4 Comparison and preferred solution

Body Coupled Communication has shown promising characteristics for enabling communication over the human body. While other communication techniques such as classic RF, UWB, or even ultrasounds are compatible for on-body as well as off-body communication, their limitations are too important to build a robust backbone for the Human Intranet. Table 2.1 summarizes the different techniques and some of their specifications. Body Coupled Communication, proposes one of the most promising characteristics with high achievable data rates, a decent on-body communication range, and is not subject to body shadowing. Besides, it is not meant to radiate power in the subject's surroundings, providing a higher level of security by physically keeping the data within the human body [50]. Only ultrasound communication offers such capability. Ultimately, the BCC coupling element tends to offer a smaller factor than the other techniques.

Table 2.1: Wireless communication technique comparison

Technique	Frequency (MHz)	Data Rate (Mbit/s)	On-body / Off-body	Range (m)	Interference	Body Shadowing
Zigbee [51]	865-2400	0.25	Yes/Yes	10	High	Yes
Bluetooth [52]	2400	1-3	Yes/Yes	10	High	Yes
UWB [53]	3-10 GHz	0.85-27	Yes/Yes	10	Medium	Yes
UWB$_{60GHz}$ [34]	51-63 GHz	0.85-27	Yes/Yes	10	Medium	Yes
Ultrasound [38]	0.1 - 10	up to 28	Yes/Yes	0.5-0.7	Low	No
BCC [29]	21 - 200	Up to 80	Yes/No	up to 2	Low	No

Given the results presented in the table above, this section focuses on comparing the three different Body Coupled Communication (BCC) techniques introduced earlier.

Magnetic-BCC (M-BCC) is an interesting technique offering one of the best path loss as

reported in [8]: up to -30 dB at 20 MHz for a 1 m separation distance (see figure 2.6). It has also been demonstrated in [9] that M-BCC can benefit from limb bending, as Tx and Rx get closer allowing a direct coupling, thus improving the channel attenuation by 10 dB (see figure 2.7(c)). On the other hand, such variations require a high input dynamic range on the receiver to properly handle the communication.

Although M-BCC offers unique advantages it suffers important drawbacks compared to Galvanic- and Capacitive-BCC (G-BCC and C-BCC respectively). First, its frequency of operation is lower than the two others, limiting the available bandwidth and thus, the maximum achievable data rate. Second, M-BCC is bulky. The coils' size corresponds to the frequency of operation. The latter being limited, the coils tend to be cumbersome. In [8], a 6.73 cm square in shape coil was designed. The second possibility is to wrap the coil around the limbs, which is not convenient, especially for nodes located close to the head, neck, or even the chest. Ultimately, M-BCC was proven sensitive to the coil-skin separation distance [8]. Such variations change the coil impedance, thus its resonance frequency leading to operate off-resonance and significantly diminishing the overall efficiency. Ensuring the separation distance would lead to tightening the coils to the human body, making it uncomfortable.

Despite the strong advantages offered with M-BCC, the drawbacks bring a high level of complexity with important limitations in building the Human Intranet.

C-BCC and G-BCC both use a pair of electrodes (on Tx and Rx) as their coupling element with the human body. The former only requires one electrode to be in contact with the medium while the latter needs both to operate. This difference in their configuration is due to the physical phenomenon responsible for signal propagation. C-BCC relies on a voltage difference between its electrodes, capacitively coupled to the human body, to generate an electric field (E-field) which propagates around the medium. G-BCC on the other hand is based on an alternating current flowing between the Tx electrodes galvanically coupled to the human body and propagating within the skin's upper layer. This difference implies one major change: G-BCC does not require a ground electrode as it does not depends on its surroundings to create a return path (i.e. electrically "closing the circuit") and thus, is insensitive to any environmental change.

Their differing mode of propagation have consequences on the level of security offered "by default". While C-BCC is based on the E-field propagating along the body, G-BCC uses the skin as a waveguide, keeping most of the signal within the medium. The latter mechanism offers a higher level of security. Nevertheless, C-BCC still offers a high level of security since the signal propagation is also based on the electrode coupling with the human body.

The above advantages in favor of G-BCC come to a cost: the channel attenuation and reachable range on the body. C-BCC brings much higher power efficiencies than galvanic coupling [11]. [12] reports an attenuation larger than 80 dB for a 20 cm communication with G-BCC for a frequency of operation of 200 kHz and a data rate of 100 kbit/s. On the other hand, [54] achieves an 80 Mbit/s C-BCC link from wrist to wrist with a 79 pJ/bit resulting efficiency. Those results are unreached with any other BCC mechanism. C-BCC offers lower attenuation at higher frequency allowing wider bandwidth, higher data rate, and longer range [7].

The bottleneck of C-BCC is the "return-path". It is the ability of the system to couple itself to a reference plane via its electrodes to "close the circuit" (see figure 2.14(b)). This phenomenon is covered in [7, 14, 16, 43]. As a consequence, the return path is different from one situation to another. It could become critical if not addressed or optimized in case of a subject moving, working out for instance.

Table 2.2 compares different BCC implementations from the state of the art and their associated performance. From all the prototypes listed, C-BCC offers the most attractive results.

Table 2.2: Wireless communication technique comparison

Parameter	Park [55][1]	Chen [12]	Seyedi [56]	Zhao [44]	Saadeh [57]	Cho [54]	
Type	M-BCC	G-BCC	G-BCC	C-BCC	C-BCC	C-BCC	C-BCC
Frequency (MHz)	37.5-42.5	0.2	Carrier-free	21	20-120	20-60/140-180	13.56
Bandwidth (MHz)	5	0.16	n/a	5.25	100	2×40	n/a
Modulation	OOK	GFSK	PPM	FSDT	BPSK/OFDM	BPSK	OOK
Rx Power (µW)	23.5	950	n/a	620	1100	6300	42.5
Tx Power (µW)	36.7	1700	2000	3520	870	1700-2600	21
Data rate (Mbit/s)	5	0.1	1.56	1.3	0.2-2	80	0.1
E./bit Rx (nJ/bit)	0.005	9.3	n/a	0.46	0.55-5.5	0.079	0.43
E./bit Tx (nJ/bit)	0.007	16	1.28	2.62	0.43-4.3	21-33	0.21
Range (cm)	10-100	10	20	50-60	25-60	180	180
Sensitivity (dBm)	-56	-82	n/a	-72	-83	-58	-72
BER	10^{-3}	10^{-3}	n/a	10^{-7}	10^{-7}-10^{-10}	10^{-5}	10^{-5}

C-BCC is our solution of choice to build the Human Intranet. Even if it performs with a lower attenuation at a higher frequency than galvanic, all the research performed to this day stays below 200 MHz for attenuation purposes. Our objective is to increase the frequency of operation to enable the surface waves as the dominant propagation mechanism [17], increase the bandwidth available and the achievable data rate within one band, which would shorten the communication duration for a given message. Ultimately, a higher data rate should help to improve the communication link's energy efficiency.

2.3 Conclusion

In this chapter, the main wireless communication techniques have been reviewed and evaluated regarding the Human Intranet framework presented in chapter 1. Particular attention has been paid to Body Coupled Communication followed by a comparison of the different mechanisms introduced leading to our choice for the following of this research work.

The first communication technique analyzed was the "classic RF". It covers standardized protocols such as Bluetooth, BLE, and ZigBee. Their common denominator is their propagation mode: a radiating element (i.g. an antenna) converts the electric signal into an electromagnetic wave propagating in the air. Despite its wide adoption among most connected objects, it is not the best choice to build a network dedicated to the human body as it suffers major drawbacks. First, the antennas undergo important detuning from their optimal frequency of operation, thus lowering their performance, making their design complex. In addition, their form factor can make them inconvenient for a final user. Second, being a popular technique, numbers of in-band interefers are present, a source of extra communication issues. Third, Classic RF also faces the body shadowing effect. The latter results in an important path loss and potential areas without coverage.

The second communication technique reviewed was the Ultra Wide Band (UWB) approach. Similar to the classic RF, it benefits from a wider bandwidth to transmit the signal, lowering its sensitivity to in-band interferers. It suffers most of the drawbacks affecting the classic RF, but requires smaller antennas. UWB is sensitive to body-antenna distance variation, leading to an unpredictable channel attenuation.

The safety and regulation topic has also been addressed. All wireless communications relying on electromagnetic waves must carefully follow the maximum power density allowed by the regulation, ensuring a safe usage of the device. It is worth noting than the maximum power density allowed is averaged over a duration of 6 minutes. Ultimately, the limitation depends on the frequency of operation, as the human does not absorb all frequencies evenly.

---

[1] Given for comparison purposes. Published very recently (Nov. 2019), after the state of the art initial review.

Ultrasonic communication has also been studied. This technique relies on non-audible acoustic waves propagating within the human body. Ultrasonic communication is limited in terms of frequency of operation, thus limiting the maximum achievable data rate. It requires a fairly bulky transceiver converting the electric signal into a mechanical vibration. Ultimately, the human body non-homogeneity creates multi-path signal propagation, deteriorating the channel characteristics due to destructive interferences for instance.

Body Coupled Communication (BCC) has then been considered. Alike ultrasonic communication, it uses the body as a communication medium. The BCC family includes three distinct techniques: Magnetic coupling (M-BCC), Galvanic coupling (G-BCC), and Capacitive coupling (C-BCC). M-BCC relies on a magnetic field generated with a coil connected to the transceiver. A similar topology is required on the receiver to sense the induced current and establish the communication. M-BCC is constrained in terms of frequency to operate with the quasi-static field, keeping the environment's effect as low as possible. Consequently, it limits its achievable data rate. M-BCC also suffers from the coil detuning due to its vicinity with the human body. This leads to an important channel gain variation when the coil-body distance changes. Finally, this technique is cumbersome, making it inconvenient to wear.

G-BCC relies on a different mechanism and topology. It requires a pair of electrodes on both ends (Tx and Rx). The electrodes are galvanically coupled to the body letting a current flow from one to the other. It propagates within the upper layer of the skin, similar to a waveguide. It offers the highest level of security of all techniques studied as most of the signal is confined within the human body. Given the dimensions involved, a higher frequency of operation increase the waveguide effect to the cost of an important attenuation. Most studies report a range not exceeding few centimeters, to at most tens of centimeters.

Finally, C-BCC has been evaluated. Similar to G-BCC it relies on a pair of electrodes on both, Tx and Rx, but only one is in contact with the skin. The other is left floating and used as a reference (called the ground electrode). An electric field is generated on one hand and received on the other. To complete the communication, a return path must be established between the ground electrodes and their environment. This return path is the C-BCC bottleneck, as it is the source of major channel variations and thus, path loss variations. On the other hand, C-BCC is compatible with a higher frequency of operation, increasing the maximum throughput and offers extended coverage and range up to two meters. Furthermore, C-BCC has been proven compatible with intra-body communication. This means that a non-invasive set of electrodes can enable communication with implanted devices, making this technique quite versatile. Ultimately, a comparison with the implemented prototype was presented. C-BCC stands out by its performance in terms of data rate and power consumption.

Despite C-BCC abilities, all implementations to date have never crossed the 200 MHz barrier. From theoretical studies, C-BCC would mostly rely on surface waves at a higher frequency of operation, which could significantly improve its robustness to environmental changes as the return path would not be as preponderant anymore. Given the above results and the room for improvement at a higher frequency, C-BCC has been chosen as the communication technique to investigate to build the Human Intranet.

3. BODY COUPLED COMMUNICATION

Body Coupled Communication (BCC), introduced in section 2.2, and in particular, Capacitive Body Coupled Communication (C-BCC), offer interesting capabilities to build and enable the Human Intranet. The state of the art only reports limited propagation mechanism analysis [7, 13, 14, 16, 43], most implementations operate below 200 MHz. Fully battery powered wearable demonstrators are rare.

This chapter presents a full communication mechanism analysis involved in C-BCC. It starts with a theoretical study, modeling a small dipole in free space and on a conductive surface. The idea here is to refer to a simple and well-known configuration modeling the C-BCC electrodes. It will theoretically describe their behavior. Electromagnetic simulations are then performed with a detailed 3D-model. They bring more accurate and realistic results to be confronted with the theoretical predictions. The propagation mechanism study is followed by a thorough channel characterization with laboratory instrumentation. Finally, an experimental on-body communication system (also referred to as a prototype) has been implemented (with off-the-shelf components) and a measurement campaign performed in free space, on phantom, and on-body. Ultimately, a channel model is built, and the optimal operating frequency chosen. To confirm the assumptions made in section 2.2, a side by side confrontation between C-BCC and other communication mechanisms is conducted.

Part of the research work reported in this chapter has been conducted in collaboration with Arno Thielens from Ghent University[1].

3.1 Theoretical Analysis

Detailed in section 2.2.3 and evaluated in section 2.2.4, Capacitive Body Communication is a promising candidate to establish the communication over the human body, key point to build the human intranet.

The two parallel conductive materials composing the electrodes can be seen as a dipole. The latter is qualified as small when the considered signal wavelength is much larger than the dipole's main dimension [17]: $d_{dipole} \ll \lambda_{signal}$.

3.1.1 Small Dipole Behavior in Free Space

Free space behavior and electromagnetic field expressions have been thoroughly studied and analyzed. Free space configuration is used as a reference scenario and is depicted below.

The electric field (E-field) radiated by a small dipole oriented along the Z axis in a classic spherical coordinate system (r, θ, φ) (see figure 3.1(a)) is given in equation (3.1) [58].

$$\begin{cases} E_\theta = \dfrac{I_0 d}{4\pi} e^{-ikr} \left(\dfrac{i\omega\mu_0}{r} + \dfrac{1}{r^2}\sqrt{\dfrac{\mu_0}{\epsilon_0}} + \dfrac{1}{i\omega\epsilon_0 r^3} \right) \sin\theta \\ E_r = \dfrac{I_0 d}{4\pi} e^{-ikr} \left(\dfrac{2}{r^2}\sqrt{\dfrac{\mu_0}{\epsilon_0}} + \dfrac{2}{i\omega\epsilon_0 r^3} \right) \cos\theta \end{cases} \tag{3.1}$$

where r is the distance from the source (centered on $(0, 0, 0)$), I_0 the magnitude of the periodic current flowing through the dipole, k the wave-packet defined as $k^2 = \omega^2/c^2$, ω the angular frequency, μ_0 and ϵ_0 the vacuum permeability and permittivity respectively.

---

[1]IMEC, with the Department of Information Technology, 9052 Ghent, Belgium, within the framework of his research collaboration with BWRC, UC Berkeley, Berkeley, California, USA.
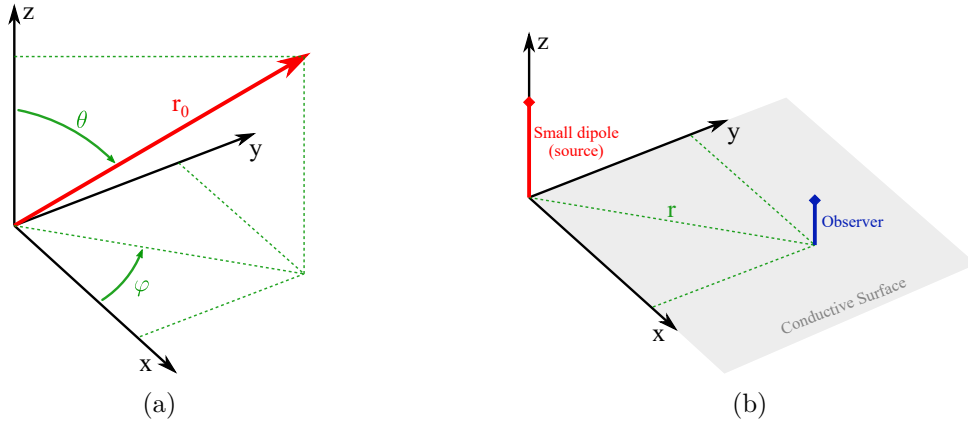
Figure 3.1: (a) Cartesian and Spherical coordinate system; (b) Dipole on a conductive surface.

Equation (3.1) is driven by the $1/r^n$ factor, inversely proportional to the source-observer distance. For very short distances, the $1/r^3$ term dominates the expression while the $1/r$ is dominant for greater distances. Those are defined as the near- and far-field zones respectively.

For later investigation, it is worth noting that the E-field magnitude, projected along the Z-axis in a Cartesian coordinate system can be written [17]:

$$|E_Z| = \left| \frac{I_0 \cdot dz \cdot k^3}{4\pi\omega\epsilon_0} i \left[\frac{1}{kr} - i \cdot \frac{1}{(kr)^2} - \frac{1}{(kr)^3} \right] \cdot e^{-ikr} \right| \tag{3.2}$$

The $1/r^n$ dependence is obvious in (3.2) as well. In both equations ((3.1) and (3.2)), the electric field amplitude decays exponentially with distance as dictated by the $1/r^n$ terms.

3.1.2 Small Dipole Behavior on a Conductive Surface

Capacitive Body Coupled Communication requires the electrodes to be positioned in contact or close vicinity to the body (see section 2.2.3). From a modeling standpoint, the body can be considered as a conductive surface. Consequently, free space equations must be adapted to take those new parameters into account.

The theoretical expression of the electromagnetic field surrounding a small dipole, located on a Cartesian coordinate system (at $(0, 0, z \geq 0)$), above an infinite conductive plane $(X, Y, 0)$ (as depicted figure 3.1(b)), is described in [59, 60].

The electric field's dominant polarization at the interface with the conductive surface, follows the dipole orientation: along the Z-axis [59]. The relative magnitude of the electric field normalized to a reference E_0, parallel to the Z-axis, at the conductor interface, at a distance r from the source can be expressed from [17, 59, 60] as:

$$\left| \frac{E_Z}{E_0} \right| = 2 \left| k \cdot S \cdot \frac{1}{r} + i \cdot \frac{1}{r^2} - \frac{1}{k} \cdot \frac{1}{r^3} \right| \tag{3.3}$$

where S is a term that depends on the frequency and the dielectric properties of the conductive surface.

Equation (3.3) is also strongly dependent on the observation distance r from the source. The first term in $1/r$ corresponds to surface wave propagation, while those in $1/r^2$ and $1/r^3$ highlight the induction field and quasi-static coupling respectively [17, 58].

3.1.3 Theoretical Model Applied to C-BCC

To better understand the propagation phenomena involved in C-BCC over the 400-500 MHz frequency band, numerical calculations were performed following equation (3.3). The S parameter (from equation (3.3)) has been computed with muscle tissue dielectric properties from Gabriel database [61], which provides human tissues' conductivity and permittivity for selected frequencies.

Figure 3.2 plots each propagation phenomena contribution computed from equation (3.3) (surface wave, induction field, and quasi-static coupling) as a ratio of the total E-field strength radiated parallel to the Z-axis. The results are a given over distance (source-observer) for two frequencies: 400 MHz (dashed lines) and 500 MHz (solid lines). Figure 3.2 highlights the surface wave dominance as the main propagation mechanism for a source-observer distance greater than 13-15 cm. The latter distance gets shorter with frequency. Surface waves bring a significant advantage as the communication should be more resilient to changes in the return path (introduced section 2.2.3).
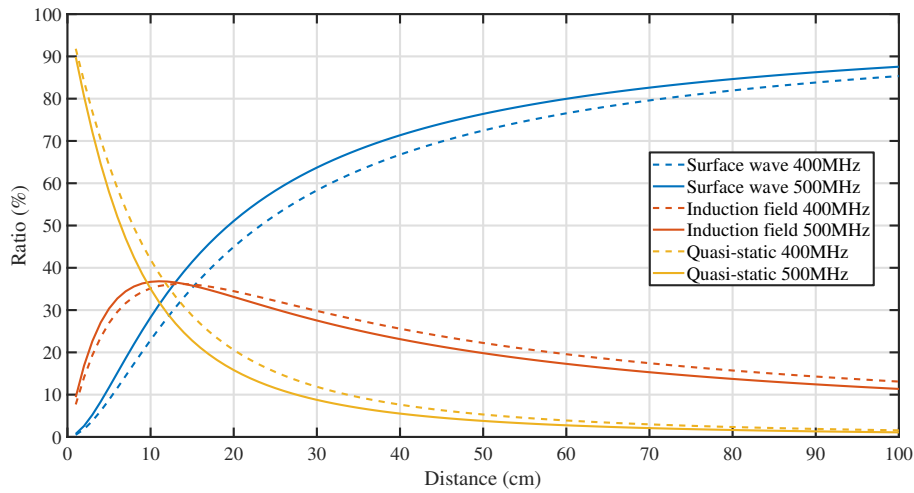
Figure 3.2: Contribution of each propagation mechanism as a proportion of the total electric field for 400 MHz (dashed lines) and 500 MHz (solid lines).

Besides the interesting hints in understanding the propagation mechanism involved for C-BCC, the model only takes a limited number of parameters into account. In fact, the human body has been approximated to a single layer, infinite surface with muscle dielectric properties. It neglects the finite size, discontinuity, versatility, lack of homogeneity, and multi-layer configuration of the human body. Consequently, the electrodes cannot only be modeled as electric circuits but necessitate full-wave electromagnetic simulations with a 3D-model to accurately describe the propagation phenomena.

3.2 Electromagnetic Simulations

Section 3.1 presented a theoretical analysis with a low complexity model highlighting the surface waves as the dominant propagation mechanism. This section aims to push the analysis further by performing electromagnetic simulations, mimicking body-worn electrodes. Two types of simulation were executed: the modeled electrodes in free space and on a so-called phantom.

3.2.1 Simulated Model

The simulations were performed with Ansoft HFSS software. It has the ability to design a realistic and complex 3D-model of the electrode involved. The different layers are assigned dielectric properties of the material, taken from the HFSS database.

The theoretical analysis considered a small dipole as a radiating source. However, from the

state of the art (see section 2.2.3) the electrodes in place for C-BCC are usually flat, with a conductive material in contact with the skin (referred to as the signal electrode). The reference electrode, however, also made of conductive material, located on top of the signal electrode. The electrode 3D-modeled in HFSS was designed following the real electrode-set fabricated in the lab. It allows simulations of the real device, which will be measured within the next stage of our investigation.

The 3D electrode model renderings, top and bottom, are presented in figure 3.3(a) and (b) respectively. The model is composed of a classic side-mounted SMA connector modeled in brass. The inner feed line is insulated from the outer chassis. Its ground pads are connected to a 35 μm-thick copper layer covering a 2×2 cm, 1.6 mm-thick FR4 substrate with rounded edges. On the opposite side, a stainless-steel snap is glued to the FR4 and connected to the SMA feed line with a copper wire. The complete electrode model also include a wet electrode used to establish the electric connection with the body (not represented in figure 3.3, pictured in figure 3.18). The electrode model described above is the main design for the rest of our investigations. It is referred to as the *small electrode.* A larger electrode following the same architecture was also implemented. It had a 5×5 cm form factor and is referred to as the *large electrode.* Its specifications are presented within the following section.

The Cartesian coordinate system orientation represented in figure 3.3 is used for the entire analysis.

(a)   (b)
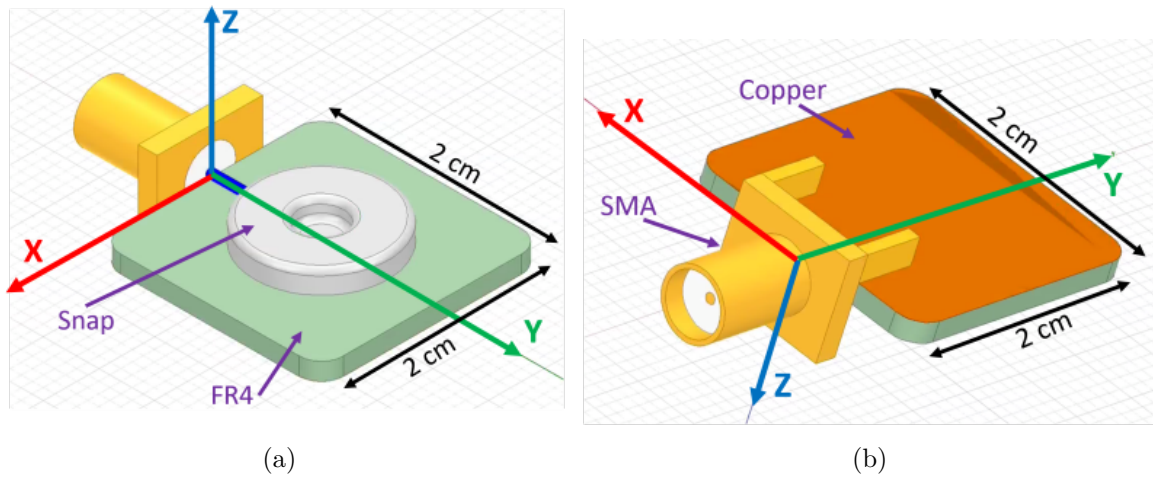
Figure 3.3: HFSS 3D electrode model: (a) top view, (b) bottom view.

The electrode will be simulated "as is" in free space conditions. To simulate a body-worn device configuration, a human body needs to be modeled in HFSS. A detailed and accurate model is complex to implement (even if 3D human body models exist) and long to simulate. Instead, a phantom (i.e. a proxy for the human body) is modeled. This simplification offers multiples advantages: the phantom geometry is chosen to avoid simulation artifacts and gives the ability to change the cross-section. Simulating different cross-sections covers a wide range of body shapes.

We used a cuboid shape with a cross-section of 50×50 mm and 4 m in length as the default phantom. With such dimensions, no simulation artifact from the edges is observed within and around the area of interest. The phantom form factor aims to imitate a human limb, more specifically a human arm. The frequency-dependent dielectric properties were chosen as those of muscle tissue from the Gabriel database [61]. Figure 3.4(a) shows the cuboid muscle in a 3D representation while figure 3.4(b) specifies the positioning of the electrode, below and centered on the muscle in the (YZ) plane.

A more detailed analysis uses a multi-layer phantom, modeling the 4 main layers of a human limb. They are, from the outer to the inner layer: skin, fat, muscle, and bone, as depicted
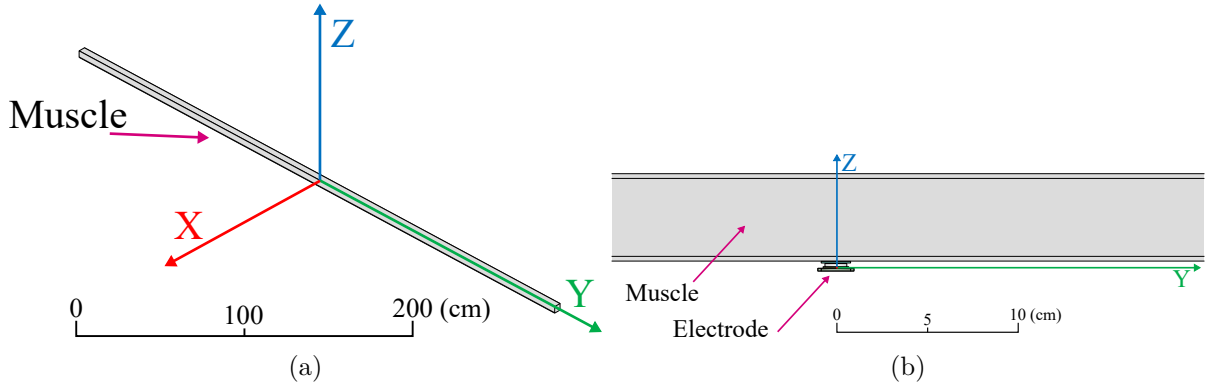
Figure 3.4: Electrode on phantom: (a) cuboid phantom 3D view, (b) 2D side view (YZ) plane.

figure 3.6(a). Their dielectric properties, permittivity, and conductivity are presented figure 3.5. This multi-layer modeling will confirm or invalidate the assumption made above regarding the interest of the single-layer abstraction level. The last representation sets up a filled and sealed, plastic-based water pipe: figure 3.6(b).
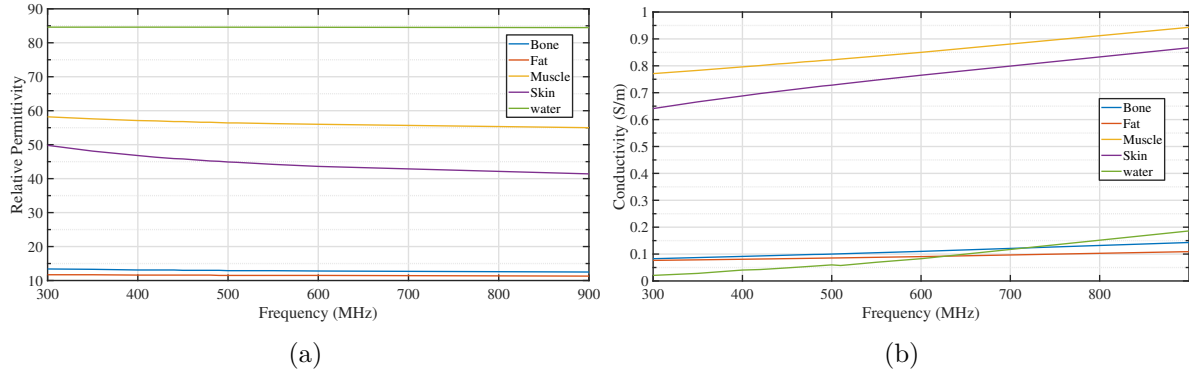
Figure 3.5: Water and human tissue dielectric properties: (a) Relative permittivity and (b) Conductivity.

Finally, a water-pipe phantom has been simulated. The water pipe is designed as a 2-meter long "phantom" which is similar in size to the muscle-based phantom depicted earlier. The dimensions allow artifact-free simulations. The water permittivity is similar to the muscle permittivity. Ultimately, this geometry can easily be built and measured with laboratory equipment, creating a solid bond between simulation and reality.
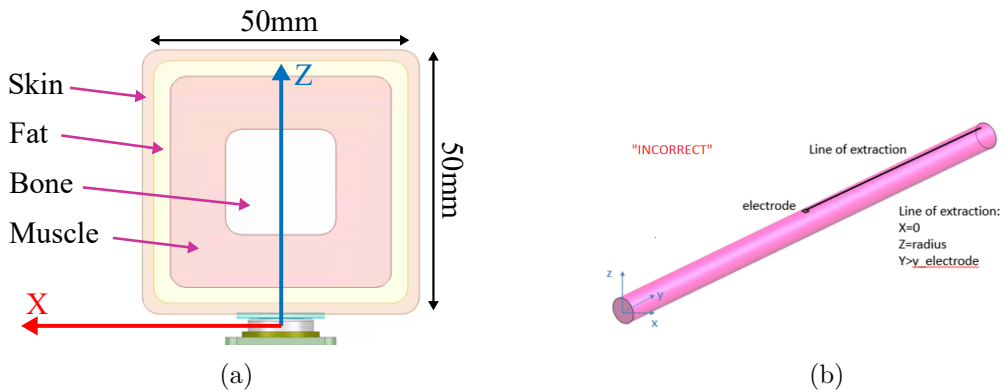
Figure 3.6: (a) Electrode on a multi-layer phantom (XZ plane 2D view), (b) water pipe 3D view.

The elements modeled are surrounded by a $3 \times 3 \times 6$ meter box of air, large enough to avoid simulation artifact at the boundaries. The source electrode is exited by a lumped port

with a 50 Ω impedance and a 1 V signal amplitude. The excitation is located between the SMA connector feed line and its chassis. Ansoft HFSS implements a Finite Element Method (FEM) applied to calculate the electromagnetic fields surrounding the electrodes excited over a frequency range from 300 MHz to 600 MHz.

3.2.2 In Free Space

The designed electrodes were simulated first in free space. Their impedance are plotted figure 3.7(a) on a Smith chart and figure 3.7(b) as its resistance (solid line) and reactance (dashed line). Figure 3.7 highlights a capacitive behavior for frequency below 1 GHz and a resonance frequency of 3.4 GHz for the main (small) electrode. The capacitive behavior was expected from design as the electrodes are made of two parallel plates of conductive material stacked on top of each other. Regarding the resonance frequency, it matches a quarter-wavelength dipole antenna in free space as:

$$f = c/\lambda \tag{3.4}$$

Where c is the speed of light in free space, and f the frequency matching the wavelength λ. Applied to the small electrode dimensions, the theoretical frequency of resonance becomes: $f_{res} = c/(4 \cdot d)$ giving $f_{res} = 3.75$ GHz for $d = 2$ cm. This result is acceptable as the excitation port is located in the SMA connector on the 3D model and a resonance frequency of 3.4 GHz corresponds to a quarter-wavelength dipole of 2.2 cm.

(a) (b)
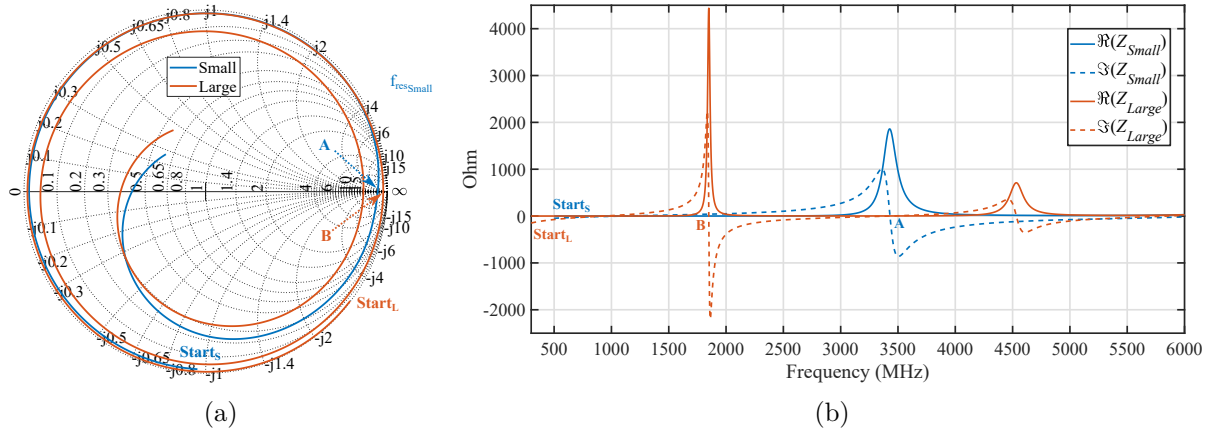
Figure 3.7: Small (blue) and large (orange) electrodes impedance simulated with HFSS: (a) on a smith chart, (b) as real (solid) and imaginary part (dashed).

Given the simulated resonance frequencies of the electrodes, the small version is selected as the default electrode for our study. The large electrode presents a resonance too low and too close to the targeted frequency operation.

For the rest of our study, the results are represented in the 2D-plane (YZ) (see figure 3.4(a)) since the electrodes are symmetric. It eases the understanding and the comparison with on-phantom simulation results.

A dipole antenna radiation pattern is represented in figure 3.8(a). It is usually described as a "donuts" shaped radiation pattern as its null is along the main axis and its maximum perpendicular to the dipole orientation.

Figure 3.8(b) represents the E-field radiated in free space at 450 MHz by the small electrode. Indicated by the color bar, the E-field strength is maximum in the center and decays with distance. The pattern described here shows great similarities with the donut-shape from figure 3.8(a). The null is identifiable, parallel to the Z-axis. The E-field stronger along the Y-axis (and the (XY) plane by extension) for a given distance. It follows the direction parallel to the

electrode's conductive surface. This is the optimal communication direction as it is outlined in figure 2.14(b).

(a)   (b)
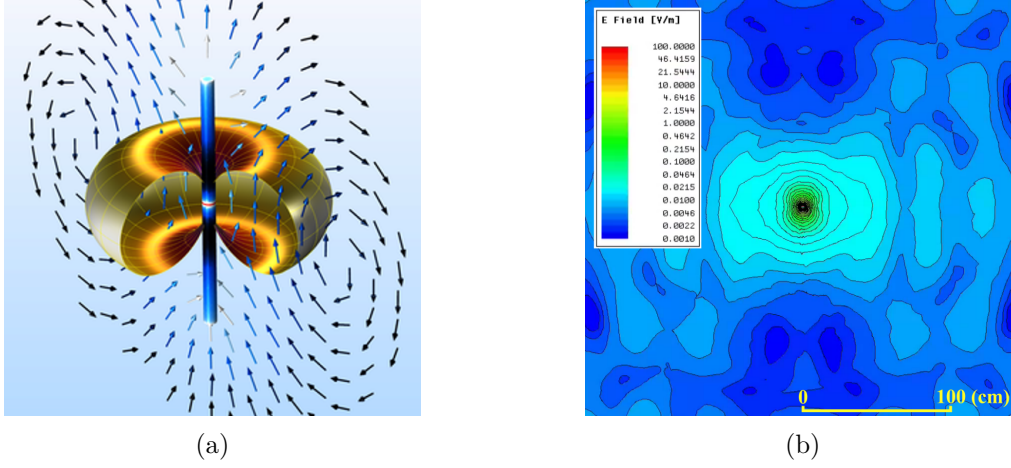
Figure 3.8: (a) Small dipole radiation pattern in free space, (b) E-field radiated from an electrode in the air at 450 MHz in the (YZ) plane.

Due to the electrode geometry and symmetry, the E-field strength analysis is narrowed down to the numerical values along the Y-axis only (for $y > 0$). Figure 3.9 plots the E-field over distance from the center of the electrode in free space. A near field approximation with a $1/r^3$ curve slope and a far-field approximation with a $1/r$ curve slopes are superimposed. The good match between the simulation results and the theoretical expectations (from equations (3.1) and (3.2)) validate the small dipole hypothesis.
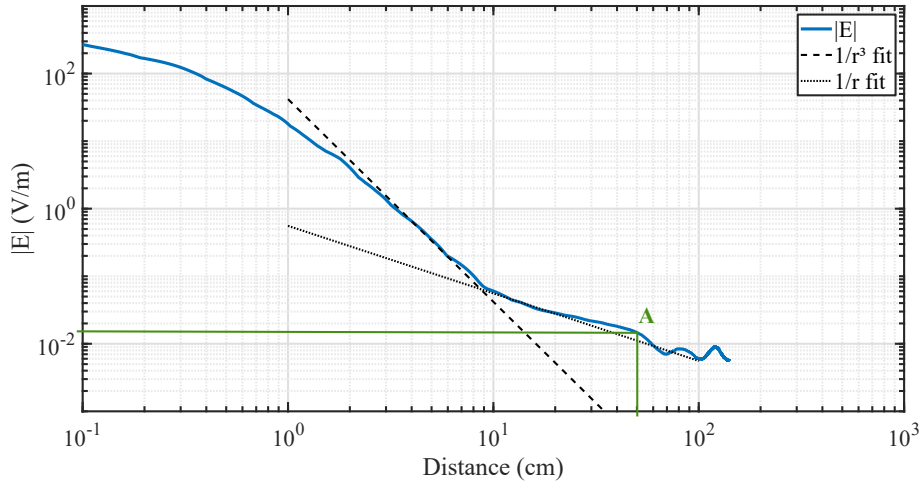
Figure 3.9: E-field magnitude radiated from an electrode in the air at 450 MHz along the Y-axis.

3.2.3 On Phantom

Phantoms for electromagnetic analysis, aim at mimicking the human body in terms of shape and dielectric properties. They help to predict the human body's effects on electromagnetic radiation. For our investigation, the first phantom is modeled in HFSS as a cuboid shape, 4-meter long and a default 50×50 mm cross-section (introduced in section 3.2.1). The simulation setup and the electrode are the same as the free space case. The electrode is in contact and located below the muscle (see figure 3.4).

The resulting E-field at 450 MHz is represented in figure 3.10. It is worth noting that the results are plot following the same color bars as figure 3.8(b). The E-field decays more softly than in free space. For instance, at a fixed distance of 50 cm (from the source), the E-field

amplitude is more than 28 dB greater than in free space (0.26 V/m on phantom (point B in figure 3.13) vs. 0.01 V/m in free space (point A in figure 3.9)).
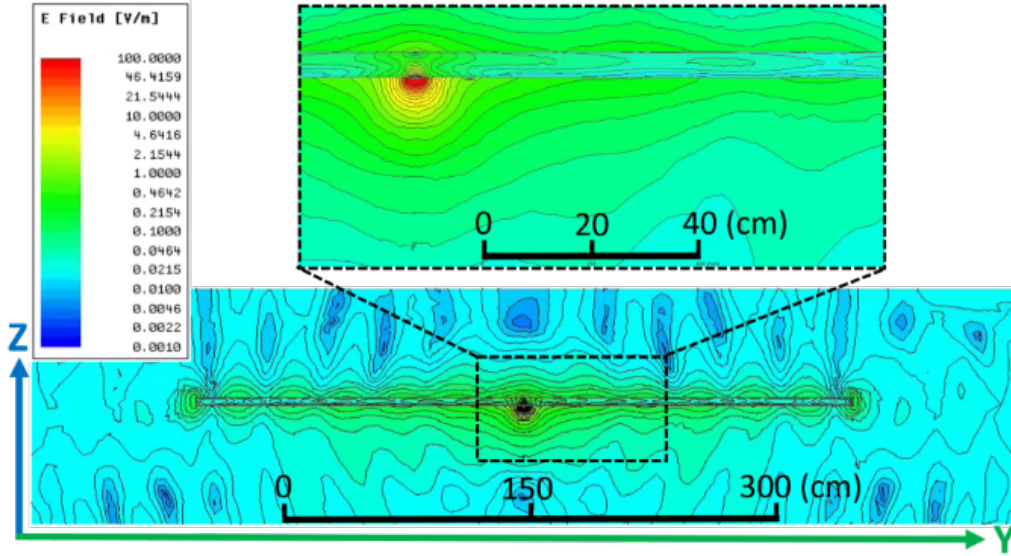
Figure 3.10: E-field radiated by a single electrode on muscle at 450 MHz in the (YZ) plane.

Figure 3.10 highlights that the E-field propagates along the phantom main dimension, acting as a waveguide. This conclusion is also supported by the Poynting vector $\vec{P}$ (defined in equation (3.5)) analysis. It represents the transported flux of energy. In other words, how the electromagnetic energy flows, containing its direction and magnitude [58].

$$\vec{P} = \vec{E} \times \vec{H} \tag{3.5}$$

The Poynting vector or direction flux of energy per unit of time and area, is represented with colored arrows, showing its direction and magnitude. Figure 3.11(a) and figure 3.11(b) propose a side-by-side comparison of $\vec{P}$ for an electrode in free space and on phantom respectively. While the energy goes in every direction in the first configuration, it primarily flows parallel to the phantom in the second. It confirms figure 3.10 interpretation: the phantom focuses on the energy and guides the propagation.

(a)   (b)
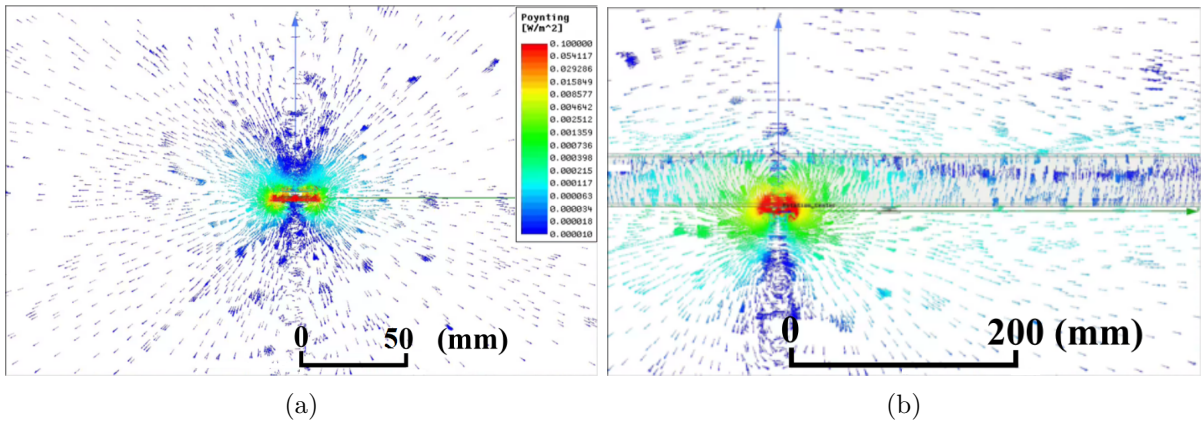
Figure 3.11: Poynting vector (a) in free space configuration, (b) on phantom configuration plot in the (YZ) plane at 450 MHz.

The E-field projected along all three axes of the Cartesian coordinate system shows a strong polarity along the Y-axis, perpendicular to the surface of interest (the phantom). The ratio of the E-field contained along this direction (Y-axis) is represented figure 3.12.
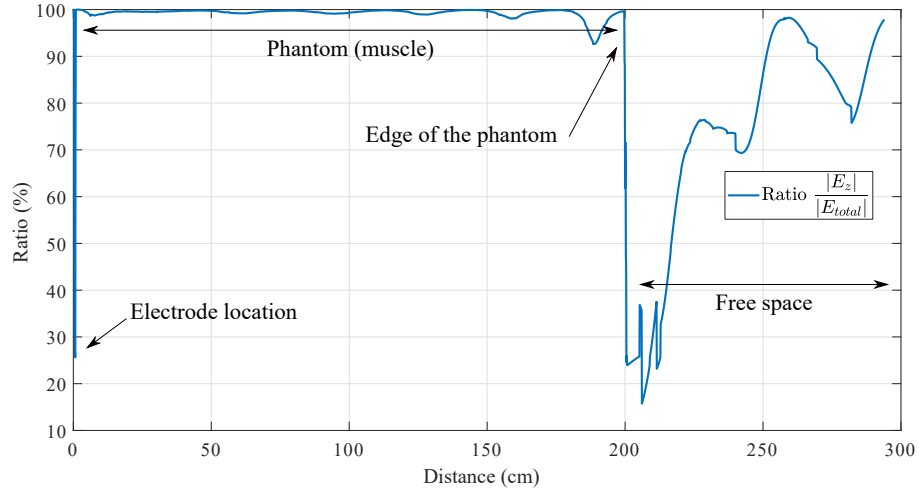
Figure 3.12: Ratio of the total electric field along Z direction at 450MHz with the electrode positioned on muscle.

From the edge of the electrode to the edge of the phantom (1 cm and 2 meter from the center of the electrode respectively), more than 98% of the E-field is polarized along the Y direction. This is coherent with the theory presented in section 3.1 and especially equation (3.3), only dealing with the E-field perpendicular to the conductive surface of consideration.

To complete our analysis, additional frequencies of excitation were simulated for the standard phantom from 420 MHz to 510 MHz by steps of 30 MHz. Figure 3.13 compares those simulations results with theoretical fits in near and far-field, $1/r^3$ and $1/r$ respectively from equation (3.3). The takeaway from this plot is dual. First, the far-field fit in $1/r$ matches very well the theoretical results. It confirms the surface waves as the dominant propagation mechanism. In the near field, the $1/r^3$ fit is close to the theoretical results for a distance greater than 2cm. This is due to the fact that the theoretical analysis takes into account a small dipole on an infinite conductive surface. While the electrode's edges are 1 cm away from the center.
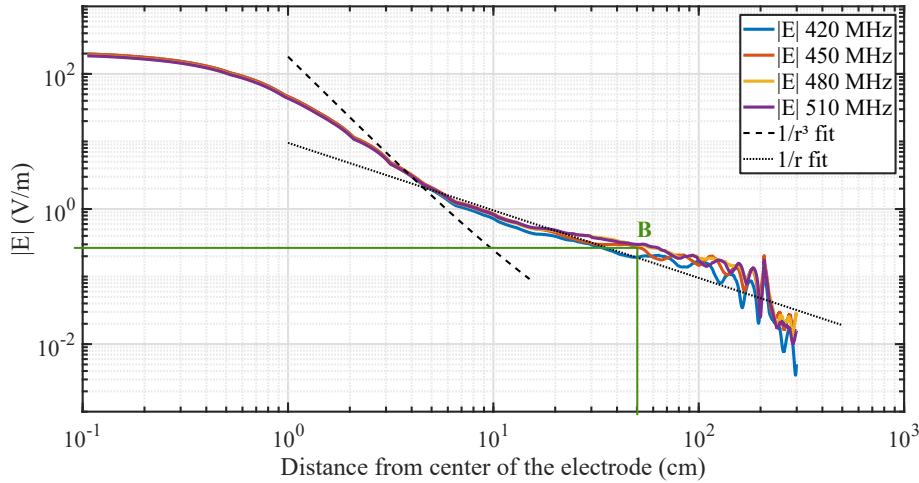
Figure 3.13: E-field along the Y-axis radiated by a single electrode on muscle for multiple frequencies on a 50 x 50mm2 phantom section.

The second point of interest from Figure 3.13, is the bundled attenuation for all frequencies over a range of almost 100 MHz. This behavior is identifiable from figure 3.14 which plots the E-field magnitude over frequency for multiple source-observer distances. The limited fluctuation (less than a factor 1.5) over frequency at a given distance is a very desirable communication channel property. It offers a wide bandwidth for implementing C-BCC, employing a 2×2 cm electrode as the coupling element.
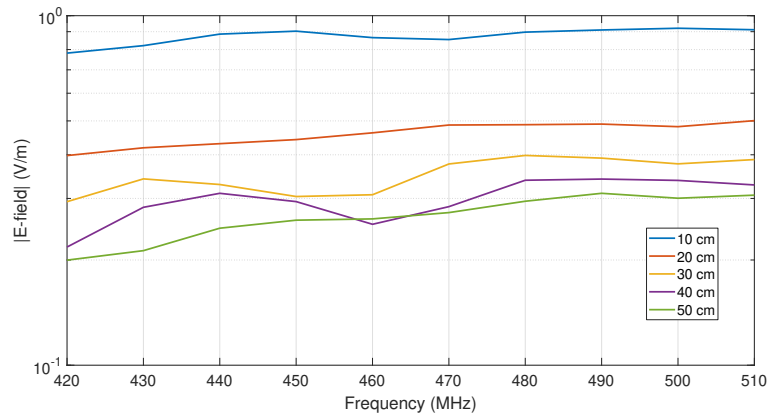
Figure 3.14: E-field radiated along the Y-axis by a single electrode on muscle over frequency for multiple distances.

The cuboid-shaped phantom standard dimensions of $50 \times 50 \times 4000$ mm was arbitrarily chosen to represent a human arm. However, shape and size vary from body to body and need to be investigated to better understand the impact of such a variation. Consequently, the phantom cross-section was swept from 30×30 mm to 80×80 mm by steps of 10 mm in side-length. The simulation results at 450 MHz are presented in figure 3.15. The induced variation in E-field magnitude quite significant. For instance, 50 cm from the electrode, the E-field magnitude varies by a factor of 5 for a cross-section change from 30×30 mm to 80×80 mm. The interpretation of this observation suggests that the factor S from equation (3.3) depends on the conductive surface dielectric properties as mentioned in [17] but also on the phantom geometry.

From figure 3.15, it appears that there is an optimal pair cross-section/frequency offering a maximal radiated power at given distance. For instance, under our simulation conditions, the optimal cross section is around 50×50 mm (yellow) and 60×60 mm (purple).
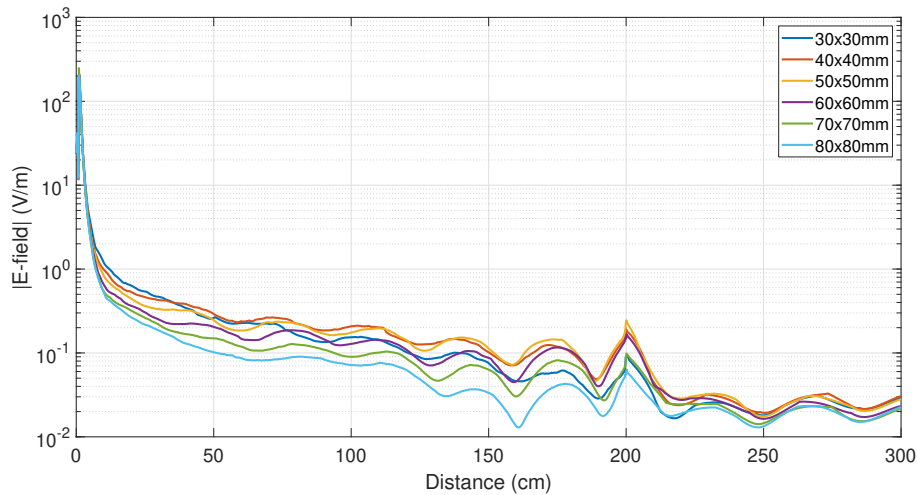
Figure 3.15: E-field radiated by a single electrode at 450 MHz on muscle for multiple frequencies on a 50 x 50 mm phantom section.

Our phantom was so far defined following a single layer topology, modeled with muscle dielectric properties. Figure 3.16 compares the single-layer approach with a multi-layer phantom (presented in figure 3.6(a)) for a given phase. Both simulation results are similar and diverge over distance. However, beyond a source-observer distance larger than 1.3 meter, the attenuation is stronger.

Given the results above, The single layer simulation approach and relative results are considered valid up to 1 m-distance. The trade-off in terms of simulation time and results accuracy
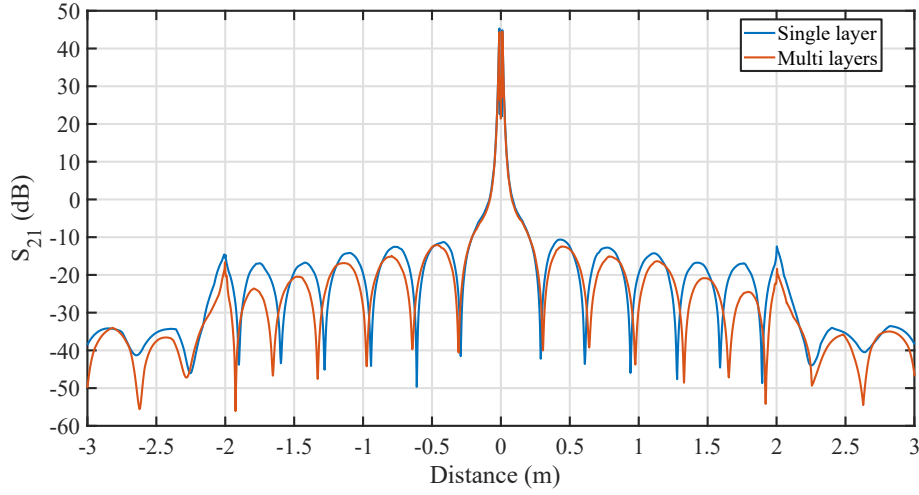
Figure 3.16: Single layer and Multi layers simulation results for a given phase.

validates our initial hypothesis.

Introduced in figure 3.13 and figure 3.14, the path loss is presented in figure 3.17 as the channel S_{21}-parameter. It plots the simulated attenuation for a pair of electrodes on the phantom. The distance between them is swept from 5 cm to 60 cm by steps of 5 cm. One electrode is used as the transmitter while the other is set as the receiver. It is the closest simulation configuration to real measurement. It eases the comparison between simulation and measurements performed at a later stage of our study.

(a)	(b)
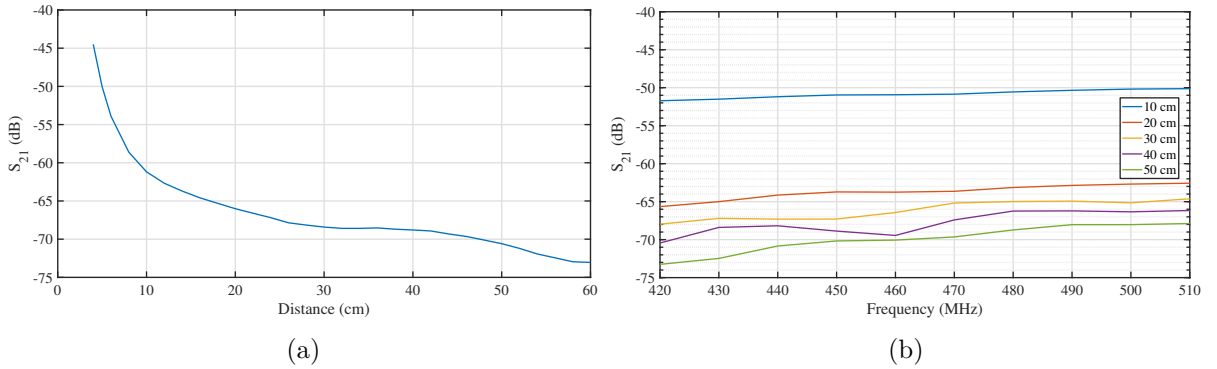
Figure 3.17: Simulated attenuation (path loss) on phantom (default dimension): (a)over distance at 450 MHz, (b) over frequency for multiple distances.

An exponential decay over distance is expected from figure 3.17(a) with an attenuation varying between -65 dB and -70 dB from 20 cm to 50 cm at 450 MHz. The attenuation over frequency (figure 3.17(b)) is flat over almost a 100 MHz-bandwidth.

The on-phantom simulation-study highlighted a positive phantom impact on the propagation. In other words, under the same simulation conditions, the E-field is stronger than in free space for a given distance (up to 28 dB better at 50 cm) and propagates further. We also showed that the E-field is strongly polarized perpendicular to the electrodes conductive planes and the phantom-air interface. Ultimately, the simulation was well aligned with the theory and initial hypothesis, in terms of the dominant propagation phenomena and the flat response over frequency. We identified the phantom geometry impact on the path loss providing good hints on the expected variations from person to person. Finally, the single-layer phantom model with muscle dielectric properties was validated by performing and comparing the simulation results with a 4-layer 3D-model.

It is also interesting noting from figure 3.10 that the E-field penetrates the phantom. It

propagates within the phantom while being out of phase with the E-field outside. The internal E-fields is out of phase in comparison to the external fields. This property could be developed to interact with an implanted device with a non-invasive source of excitation.

3.2.4 Wrap-up

The electromagnetic (EM) simulations performed in this section confirmed the initial hypotheses and assumptions made to conduct the theoretical analysis. In fact, the free space small dipole behavior on a conductive plane was confirmed by 2D-simulation with the phantom. The dominant propagation phenomenon was also verified, with a clear boundary distance where the surface waves take over the quasi-static coupling. From the simulation, we also observed a path loss improvement while in presence of phantom as propagation support.

3.3 Channel Characterization

Sections 3.1 and 3.2 proposed a theoretical model and analysis followed by EM simulation. This section covers the electrode implementation and testing with laboratory instruments as well as a specifically designed prototype.

3.3.1 Electrode Implementation and VNA measurements

3.3.1.1 Electrode design and sizing

As stated in section 3.2.1, the real electrodes, and their HFSS 3D model were completed in parallel, ensuring a high fidelity between the implemented and simulated coupling elements. The real electrodes were made of a single-sided clad board, 1.6 mm-thick laminated with a 0.35 µm copper layer. A side-mounted SMA connector is soldered on the edge to the copper layer. On the opposite face, a female snap is glued, centered on the support. The snap was taken from a regular ECG cable for medical use. Two versions of the electrode were made, a *large* 5×5 cm and a *small* 2×2 cm. On the former, the whole lead termination is fixed on the electrode (as it fits) while the latter only features the snap without a plastic bezel. The last part composing the electrode is the pre-gelled skin electrode, ensuring the connection between the human body and the female snap. Those pre-gelled skin electrodes are one-time use for medical applications [62] allowing a high repeatability factor by facilitating the positioning, a solid body-interface, and offering the same adhesiveness for every measurement. Scaled pictures of both electrodes, as well as the pre-gelled skin-electrode, are presented in figure 3.18.

(a)   (b)
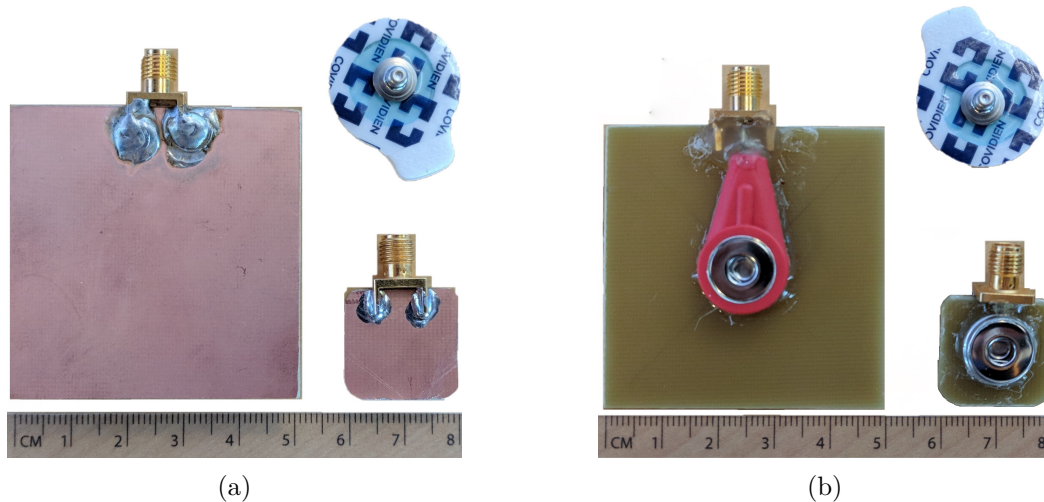
Figure 3.18: Real electrodes, 2×2 cm, 5×5 cm and pre-gelled skin electrodes: (a) top view, (b) bottom view.

The measurements were performed with a 2-port E5071C or a 4-port N5242A Vector Net-

work Analyzer (VNA), both from Agilent. 70-cm cables were attached to the measurement instrument. The calibration was performed with an electronic calibration kit (E-cal kit) for every measurement set.

Ultimately, the electrode was connected to the cable and positioned on a non-conductive stand (made of cardboard), about a meter from the ground under free space configuration. For on-phantom and on-body measurements, the pre-gelled skin electrodes ensured the coupling with the medium. The height was also fixed and kept constant. The distance between the electrodes was maintained stable for the entire measurement duration due to the adhesive property of the pre-gelled skin electrode and will be specified for each result.

3.3.1.2 In Free Space

The electrodes' impedance in free space are shown in figure 3.19. The large electrode (5×5 cm) measurement (dark blue) and simulation (light blue) results are compared on a Smith chart figure 3.19(a) and as a real and imaginary part on figure 3.19(b). There is a slight frequency shift in the resonance frequency: about 300 MHz. It can be explained by the complexity of the real electrode. difficult to replicate with its 3D HFSS model counterpart. The snap is the end of a regular ECG lead, still encapsulated into the resin-based tip. The material and properties and dimensions were replicated in the model with the greatest possible accuracy with the data available and measured. It consequently impacts the distance and conductivity of the material keeping apart the parallel conductive plates.

Figure 3.19 also shows the small electrode (2×2 cm) characteristics following the same approach. Their much simpler and basic design in comparison to the larger electrode, highlight a greater coherence between measured (blue) and simulated (green) results with a resonance frequency of less than 40 MHz apart. In this case, the control over the positioning was greater, allowing a finer replica in HFSS.

We can already conclude regarding the design of the electrode. Its implementation is sensitive to the distance between the conductive planes, their geometry, and symmetry. A more robust and repeatable electrode "manufacturing" such as printed electronics would allow an optimized electrode design and implementation.

(a)   (b)
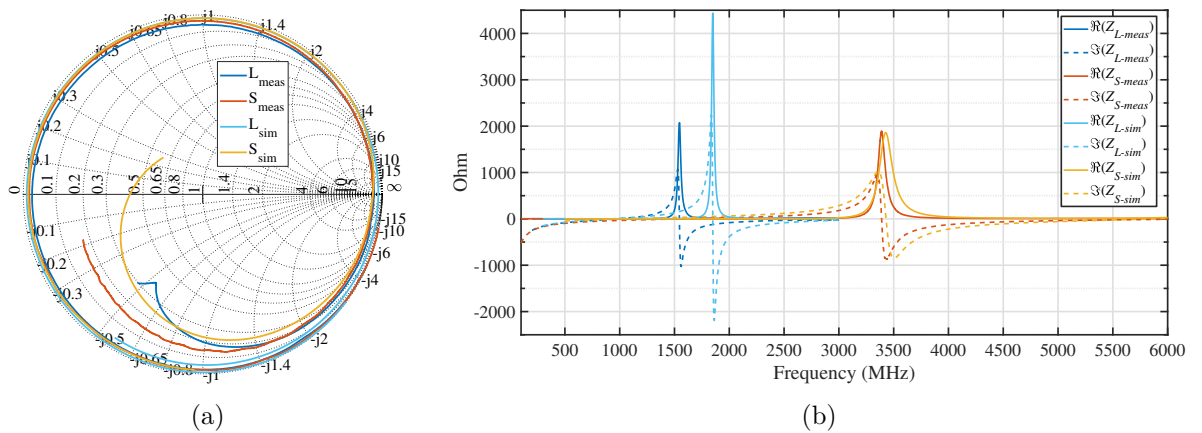
Figure 3.19: Electrode impedance simulated (light blue and yellow) and measured (dark blue and orange) for both sizes (large: dark and light blue - small: orange and yellow): (a) on a smith chart, (b) as real and imaginary part.

Figure 3.20 shows the free space measurement setup with the VNA. As mentioned earlier, non-conductive support holding the electrodes was put together keeping the distance between them solid.

In terms of insertion losses, no particular matching network or design technique was applied. Multiple reasons support that decision. An adapted matching would reduce the bandwidth
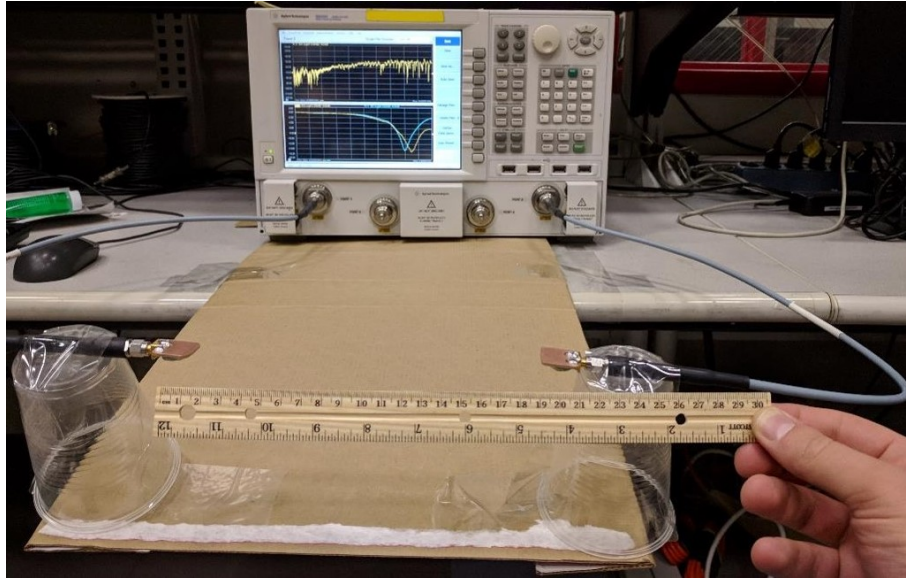
Figure 3.20: VNA free space measurement setup.

available, enabling narrow-band communication only. The results presented are given under free space conditions, without suffering from the human body load which would "de-tune" the electrode. Instead, a wide band characterization is performed, confirming the suspected (from simulation) electrode wideband behavior and compatibility.

The transmission parameter S_{21}, between a pair of small electrodes, is plotted in Figure 3.21. They are positioned 10 cm (blue) and 20 cm (orange) apart from one another. The difference between the two, calculated as $\Delta S_{21} = S_{21_{10cm}} - S_{21_{20cm}}$, is represented in yellow on the figure. The lower part of the spectrum (sub-GHz) shows an attenuation between 0 and 5 dB while the path loss average comes close to 6 dB from 1.5 GHz to 5 GHz. The difference can be explained by the multipath, reflection, and interferences with the environment for sub-GHz frequencies as the measurement was not conducted in an anechoic chamber.
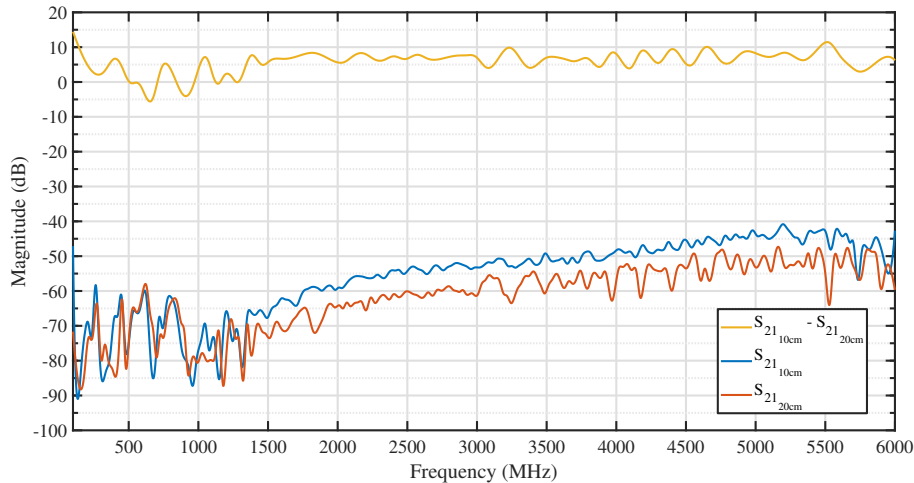
Figure 3.21: S21 over the air (free space), 10 cm (blue), 20 cm (orange) apart and their difference (yellow).

As a reminder, the Friis' law [63], defining the relationship between transmitted and received power (see equation (3.6)) is only applicable for a far-field configuration (commonly considered $d \gg \lambda$).

From (3.6), where G_{Tx} and G_{Rx} are the gain of the transmitter and receiver antenna respectively, λ the wavelength and d the distance between the two, we can calculate that doubling the

distance ($d' = 2 \cdot d$) would increase the path loss by 6 dB.

$$\frac{P_{Rx}}{P_{Tx}} = G_{Tx} \cdot G_{Rx} \cdot \left(\frac{\lambda}{4\pi d}\right)^2 \tag{3.6}$$

From [64], we learn that the near field channel model applicable to the E-field can be approximated with far-field path gain when the range is greater than $d \approx 0.15 \cdot \lambda$, for a vertically polarized electric antenna such as the one we have.

The free space measurement results obtained with the laboratory instruments show a very good alignment with the theoretical analysis proposed earlier and with the simulations' output as well.

3.3.1.3 On Body

After testing the electrode with the VNA under free space conditions, on-body measurements were performed. Only the small electrode set was tested as its characteristics offer better compatibility in terms of frequency of operation and future prototype implementation. The electrode impedance while positioned on the body (along with the free space measurement for comparison purposes) is presented in figure 3.22 on a Smith chart (a) and as its real and imaginary part (b). The electrode impedance is presented under those two formats as it is not tuned for a particular frequency. Consequently, the results' readability is more difficult. Last, the frequency range covered is much wider than the targeted operating frequency.

The on-body impedance was expected to be different (from free space) as it loads the radiating device. By comparing the two on figure 3.22(b), we observe that the resonance frequency is shifted toward the lower part of the spectrum, its magnitude divided by four, as its frequency spread. For sub-GHz frequencies, the electrode behavior is capacitive.

| (a) | (b) |
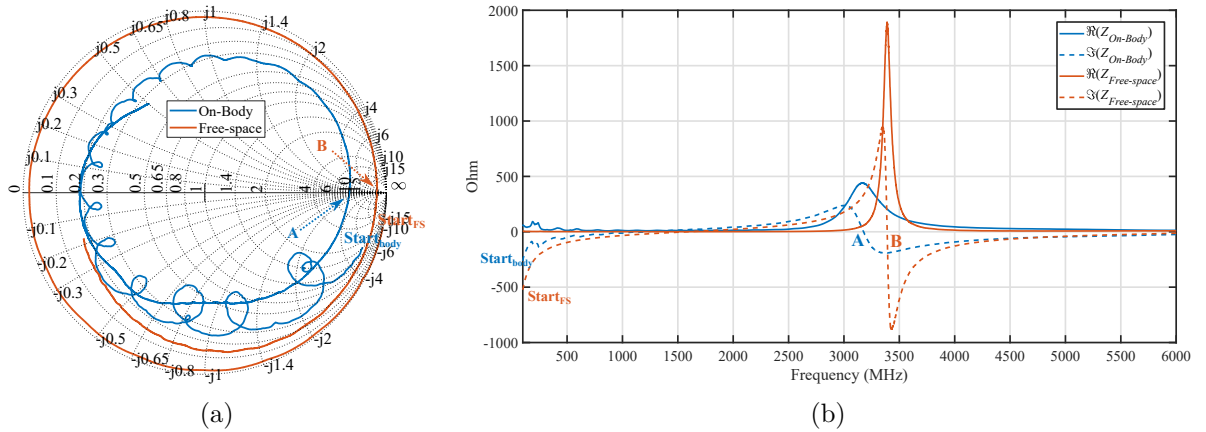
Figure 3.22: Measured electrode impedance (S_{11}) on body (a) on a smith chart, (b) as real and imaginary part.

Performing relevant C-BCC on body measurements is challenging as both (Tx and Rx) electrode-set's reference planes are connected via the lab equipment. This topic has been covered in literature [14, 17, 45]. Following those publications, a BalUn was placed between the electrode and the VNA on both channels.

The interconnected BalUn [65] is designed to operate from 400 MHz to 2300 MHz. It offers a 1-input-2-outputs configuration. It was selected for its frequency of operation as well as its form factor, connector compatibility with the lab equipment, and its price range. The VNA channel was connected to the input port with a cable while one electrode-set was connected to output A and a 50 Ω load plugged into output B. The second channel was set up following the same procedure. Since the instrument is not directly connected to the electrode-set, it would be pointless to look at the S_{ii} parameter as we would represent the accepted power of the following

combination: BalUn, 50 Ω load and the on-body electrode. However, the S_{ij} parameter shows the transmitted power from one port to the other. The interconnected BalUn helps to insulate both electrode set from the instrument ground which creates an artificial return path.

The transmission parameter S_{21} is presented in figure 3.23. It was recorded following the configuration presented above, both electrode-set positioned on the forearm, 10 cm apart from one another. From this figure, we observe a flat attenuation, about 30-35 dB, over a wide frequency range, from 400 MHz to 1200 MHz. This behavior is well aligned with the simulation prediction as presented figure 3.14, highlighted a flat E-field strength over frequency.
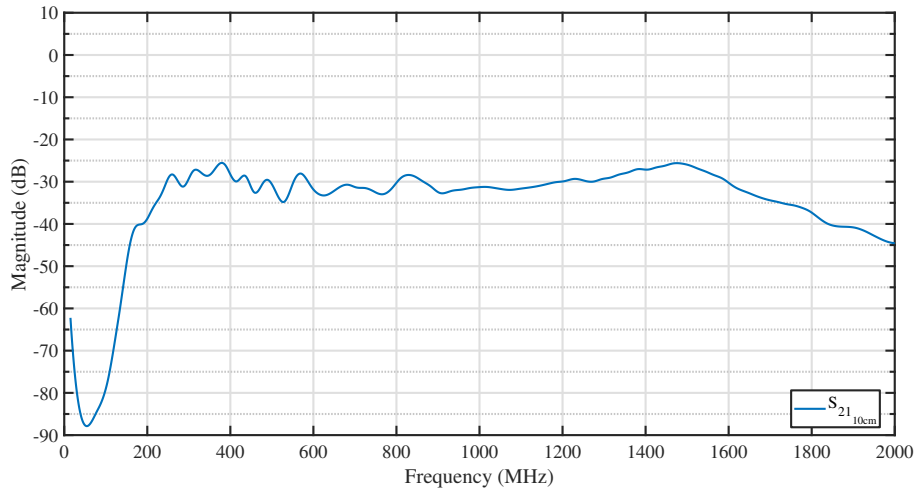
Figure 3.23: On-body attenuation for 10 cm distance (a) on the forearm.

In terms of path loss, a wide range of attenuation is reported in the literature under different circumstances. For instance, [43] proposes measurements under the same conditions: a VNA in combination with BalUns. Multiple distances are analyzed over a frequency range from 1 MHz to 100 MHz. The attenuation observed varies from -65 dB at 1 MHz to -10 dB around 30 MHz. In [16], the authors present a global attenuation of -40 dB, -45 dB and -60 dB for a transmission distances of 10, 40 and 120 cm (at 100 MHz) respectively, with capacitive coupling. They propose a configuration that is qualified as a hybrid. The transmitter (Tx) was battery powered while the receiver (Rx) is a spectrum analyzer. The difference between [43] and [16] could mainly be explained by a distinct ground between Tx and Rx in the second case. This topic is directly addressed in [45] where the authors compare grounded equipment to battery-powered systems. The grounded lab equipment offers around 20 dB more transmitted power than their battery-powered counterpart at 100 MHz. The measured attenuation is about -50 dB and -70 dB respectively. Those results from multiple investigations show two points. First, the attenuation observed with our setup is falling in the range of attenuation reported in the state of the art. Second, even with BalUn attempting splitting Tx and Rx grounds, the VNA does not offer a fully distinct setup for Tx and Rx. Consequently, another solution, fully battery-powered, will be necessary to characterize the channel under proper test conditions.

From the default configuration studied with the VNA, other locations and distances were investigated. The electrodes were positioned on the shin offering a very short distance between the electrode-set and the bone. A second location was explored: the biceps where the muscle volume is greater than the forearm and the shin. The distance between the electrode was kept constant (10 cm and 20 cm) and no significant variations were observed.

Figure 3.24 presents the difference in terms of path loss between two distances of 10 cm and 20 cm. For frequencies below 2 GHz, the measurements are similar but bouncy, no conclusion can be taken from such a comparison. For higher frequencies, a 6 dB difference is observed, falling into the classical expectation as the distance was doubled.

Figure 3.25 compares the simulated and measured electrode impedance on a restricted fre-
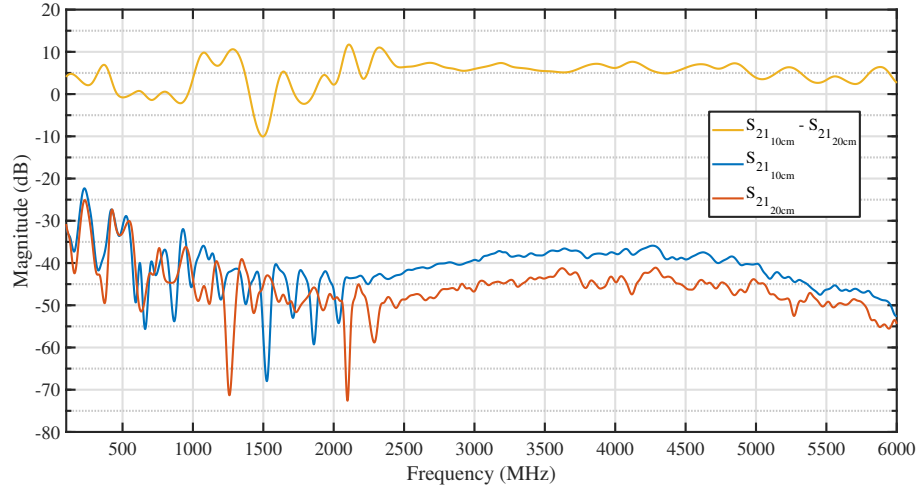
Figure 3.24: S_{21} measured on body, 10 cm (blue), 20 cm (orange) apart and their difference (yellow).

quency range. The results are similar which confirms the assumption made during the previous stage of our investigation: the EM electrode 3D-model is reliable as much as the human body representation with a single muscle layer.
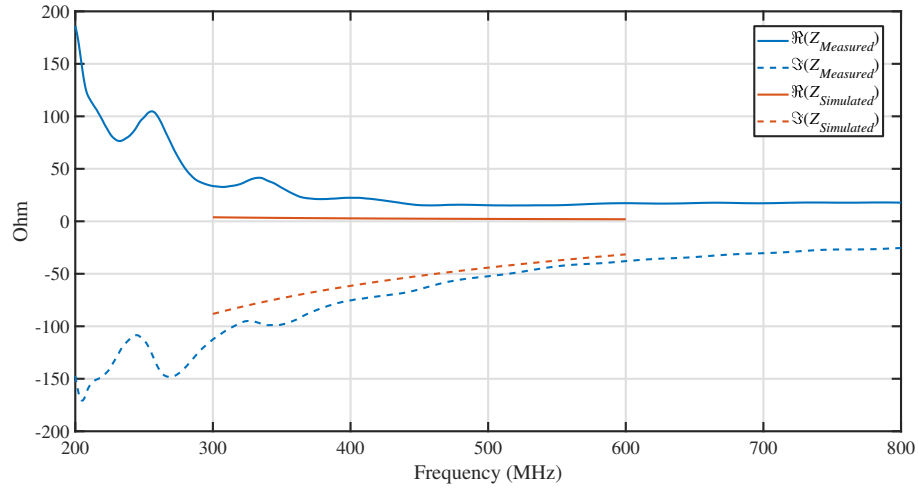
Figure 3.25: Electrode impedance simulated vs. measured with a VNA

The free-space and on-body VNA measurements were once again well aligned with the theoretical predictions and simulation results, in terms of behavior and bandwidth available. However, while performing a VNA measurement, Tx and Rx grounds are not split providing very optimistic results in terms of attenuation and no conclusion can be taken regarding the impact of distance on the path loss at the frequency of interest. A fully battery-powered approach is mandatory.

3.3.2 Prototype Implementation and In-Context System Measurements

The results obtained with the VNA were promising. However, the measurement limitation due to the VNA and the need to physically split the grounds (reference plane for the studied Tx and Rx), required the implementation of a battery-powered setup. From the literature [14], the equipment's ground plane size can significantly impact the measurement results. It was decided to look for a solution as small as possible. Consequently, portable instrumentation was excluded. Also, the smaller the test setup, the closer to a real implementation we get, thus more significant become the results.

3.3.2.1 Battery Powered Prototype BoM and Operating Mode

To prevent coupling, C-BCC should only be tested with an isolated power supply. Besides, the instrument ground plane size should be minimized to limit over-the-air coupling. A bigger reference plane will increase the coupling of the system to its environment. Consequently, it was chosen to use the small form factor solution based on the kit STEVAL-FKI433V2 [66]. This kit consists of a motherboard Nucleo Board STM32L053R8 on which is plugged an S2-LP radio daughter-board (figure (a) and (b) respectively). The Nucleo board embeds a Cortex-M0+ that controls the radio and allows data-download to a computer for processing. Both boards are powered by a single 3.6V battery (figure (c)). For our experiments, two of these modules were combined: one for transmission and one for the reception.

| (a) | (b) | (c) |
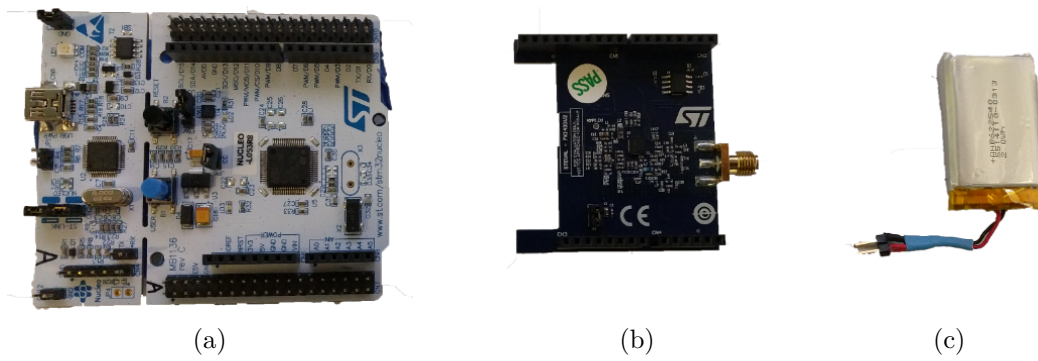
Figure 3.26: Prototype components: (a) Nucleo board, (b) Sub-GHz radio, (c) battery

The C-BCC electrodes are composed of two distinct parts as described figure 3.18. A 15 cm long SMA cable connects the electrode to the radio, without the addition of a matching network. The complete prototype is presented figure 3.27.
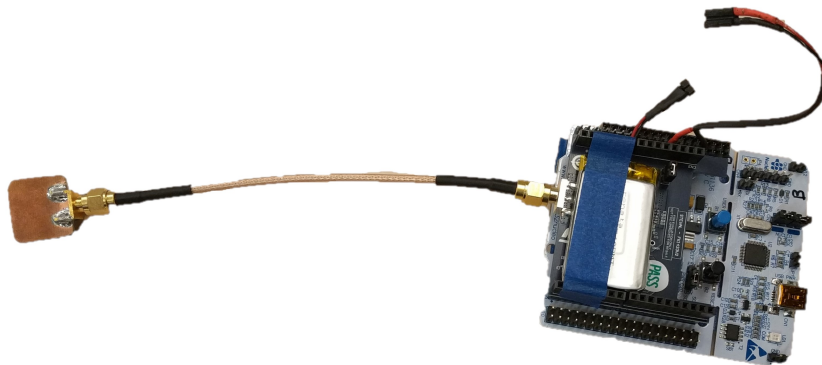
Figure 3.27: Assembled battery powered prototype

To measure the channel attenuation under different conditions, the Tx radio was set up to generate a continuous wave (CW) over the range of interest: from 420 MHz to 510 MHz by steps of 10 MHz. The Rx radio was programmed to store the Received Signal Strength Indicator (RSSi) values in the microcontroller flash memory on the motherboard.

No connection nor signal was shared between Tx and Rx, they are totally asynchronous. Both boards follow a 5 s cycle for each measured frequency. Once the cycle begins, the Tx waits for 750 ms before transmitting a continuous wave which lasts 3 s. At the end of the 5 s-cycle, the Tx switches to the following pre-programmed frequency and waits for the following cycle to begin. On the Rx side, as soon as the program is triggered, the board begins recording the RSSi value from the corresponding register, every 40 ms. A total of 116 samples are collected per frequency step. This phase lasts for 4.64 s. At the end of the cycle, the data are transferred to the microcontroller the flash memory. The radio switches to the following pre-programmed frequency and waits for the start signal. The start signal timing is kept fixed by interruptions from the on-board timer. The full measurement-set is manually triggered once, by an operator. The flexibility of this approach and the accuracy of the timer relax the synchronization constraint on the operator triggering the initial start signal on both TX and RX at the same time.

Before the measurement, a relative power calibration was performed. It consists of setting the output power of the TX radio to 0 dBm (an inaccurate value when measured with a precision instrument) and recording the RSSi on the Rx radio (when both are connected together with a direct cable), for all the frequencies of interest while both devices are connected with a female-to-female SMA connector. The radio offers a function that converts the RSSi to dBm; the measurement granularity is 1 dBm. In the end, the measured received power is 3 to 6 dB lower than the Tx settings (set to 0 dBm output power). Those losses are mainly due to the on-board matching network centered around 433 MHz.

In terms of data processing, the recorded values are read from the Nucleo board via the ST-Link and downloaded to the computer in binary format. Each memory block represents 128 values. The program resets them all to 0 before starting the recording. Consequently, it is simple and robust to detect a change in frequency as the program only stores 116 values out of the 128 available slots (12 zeros in a row). Out of the 116 samples recorder, only a portion of them corresponds to the signal transmitted from the Tx board since the recording lasts about 4.64 s while the CW is fed to the Tx electrode for only 3 s. The remaining recorded samples represent the ambient noise. From our experiments, only a few times the distinction between noise and the transmitted signal was difficult and should have been done manually, otherwise, the data processing was performed with MatLab, detecting the edge (in terms of RSSi) allowing automatic and fast computing.

3.3.2.2 Measurements in Free Space

The measurement in free space, as for the theoretical and simulation analysis, aims to provide a reference scenario for the new measurement setup. For consistency and repeatability purposes a stand was assembled and used for every free space measurements. It is portable, made of cardboard with a surface large enough to hold both boards. To limit the coupling between the two Nucleo boards (and the RF daughter-board), both were positioned with the longest distance possible between them. As stated earlier, a 15 cm cable connects each board to its electrode-set. The distance between the electrodes is measured from center to center. The measurement setup is presented in figure 3.28. The measurements were performed in a regular electromagnetic environment, facing ambient radiations and interferer.

The results obtained with the above setup are presented in figure 3.29, covering three distances (colors) and thee types of measurements (line style). The attenuation was measured for 10 cm (blue), 20 cm (orange) and 140 cm (yellow). For each distance-frequency pair, the results show variations in the recorded RSSi. To represent these fluctuations, the different reported values are plotted as a star on the graph. It gives the RSSi variation observed at glance and, unlike an error bar, with this method, the reader can tell the difference between an isolated extreme value and a real value hit multiple times during the recording session. The lines connect the average for each distance-frequency pair.

The solid lines represent the received power when the Tx board is transmitting. Given the

(a)   (b)
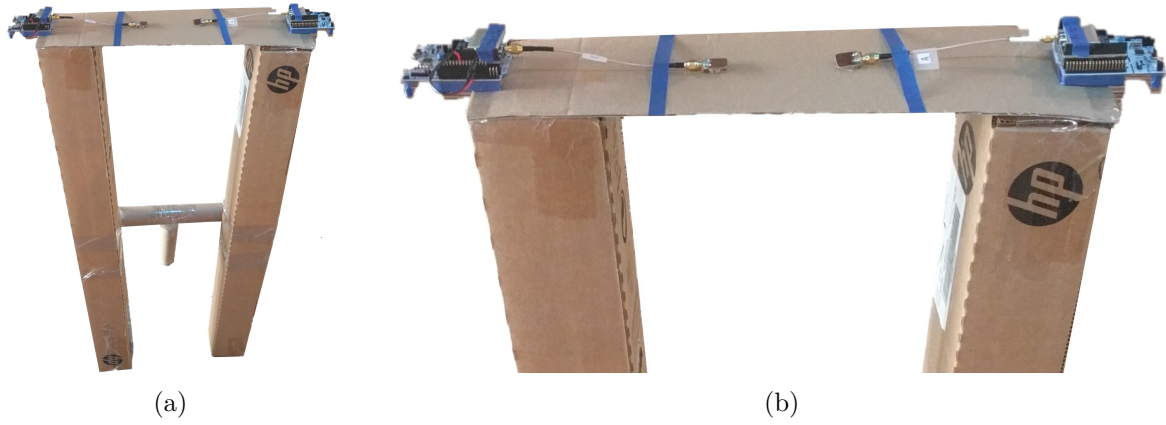
Figure 3.28: Prototype (a) test setup in free space, (b) zoom
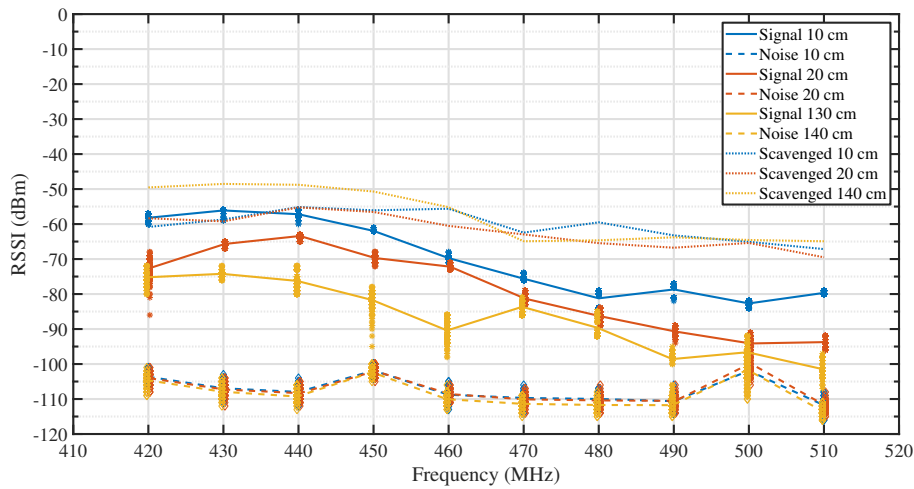
Figure 3.29: Free space attenuation over frequency

configuration, it corresponds to the channel attenuation as Tx is transmitting with an output power set to 0 dBm. For all three distances (10 cm, 20 cm, and 140 cm) the attenuation increases with frequency. The path loss increases by 20 dB to 25 dB over the frequency range of interest. The great similarity is observed in the results shape and trend for all three distances over frequency. It is interesting noting that the variability of the results also increases with distance; Less than 5 dB for 10 cm it can reach more than 10 dB at 140 cm.

Dashed lines are also plotted in figure 3.29. They represent the ambient noise, which is recorded while the Tx board is not transmitted. As expected, the distance between boards does not impact the sensed ambient noise and the curves superimpose almost perfectly on top of each other. The variability is also in the same range, a little less than 10 dB. Two frequencies, 450 MHz and 500 MHz are showing slightly and significantly higher noise with an average 5 dB and 9 dB more powerful than the surrounding frequencies. This behavior can be explained as the measurements were conducted in a regular environment and not in an anechoic chamber.

The last kind of data plotted in figure 3.29 is the "scavenged" signal, drawn with a dotted line. This signal is acquired by a sniffing setup pictured in figure 3.30. It is composed of an omnidirectional antenna plugged into a signal analyzer. The antenna was positioned 1 meter away from the cardboard setup center. The idea was to figure out and analyze how much power can be sensed by such a setup. The sniffed signal is stronger on the signal analyzer. All three plots (i.e. distances) are grouped. They also show an increasing attenuation with frequency. From this measurement, we can conclude that the electrode is a poor reception antenna for free-space communication. It behaves like a small dipole as predicted in the above sections.
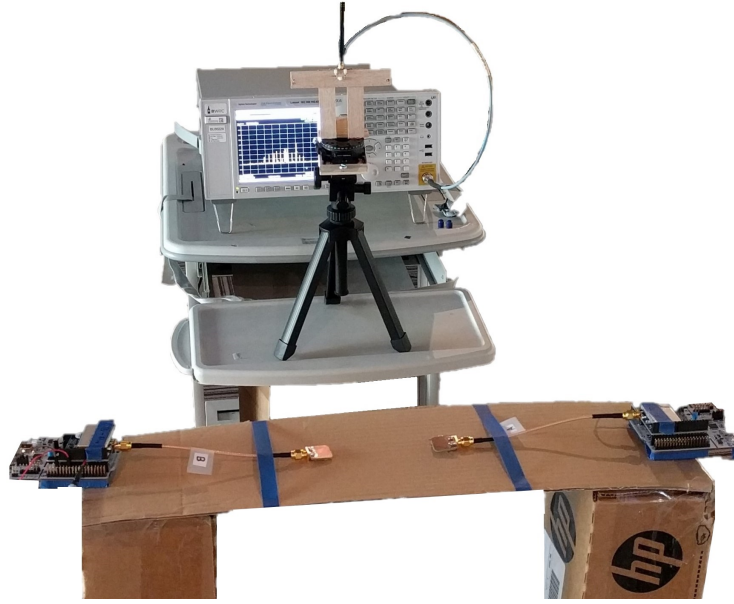
Figure 3.30: Free space measurement with sniffing setup.

3.3.2.3 Measurements on Phantom

Presented in figure 3.6(b), a 2.1 m-long water pipe, 5 cm in diameter, was assembled, filled with tap water, and sealed. The water pipe was positioned horizontally on two non-conductive wooden stands, about 80 cm from the ground. One of the tips was raised by an extra 5 cm, ensuring no air bubble within the transmission path of interest. The electrodes were centered on the pipe, limiting as much as possible any potential reflection and side-effect during the measurement. The setup and the measurement conditions are presented figure 3.31(a). A derived setup pictured figure 3.31(b), introducing electromagnetic absorbing foam avoiding reflection on the ground was also used to perform the measurements. The battery-powered prototype was located on top of the pipe and secured with a rubber band. The connection between the electrode-set and the pipe was ensured by the pre-gelled medical electrode. The path loss was recorded from 420 MHz to 510 MHz by steps of 10 MHz every 5 cm, from 5 cm to 50 cm. A closer picture is proposed in figure 3.31(c).

(a)

(b)

(c)
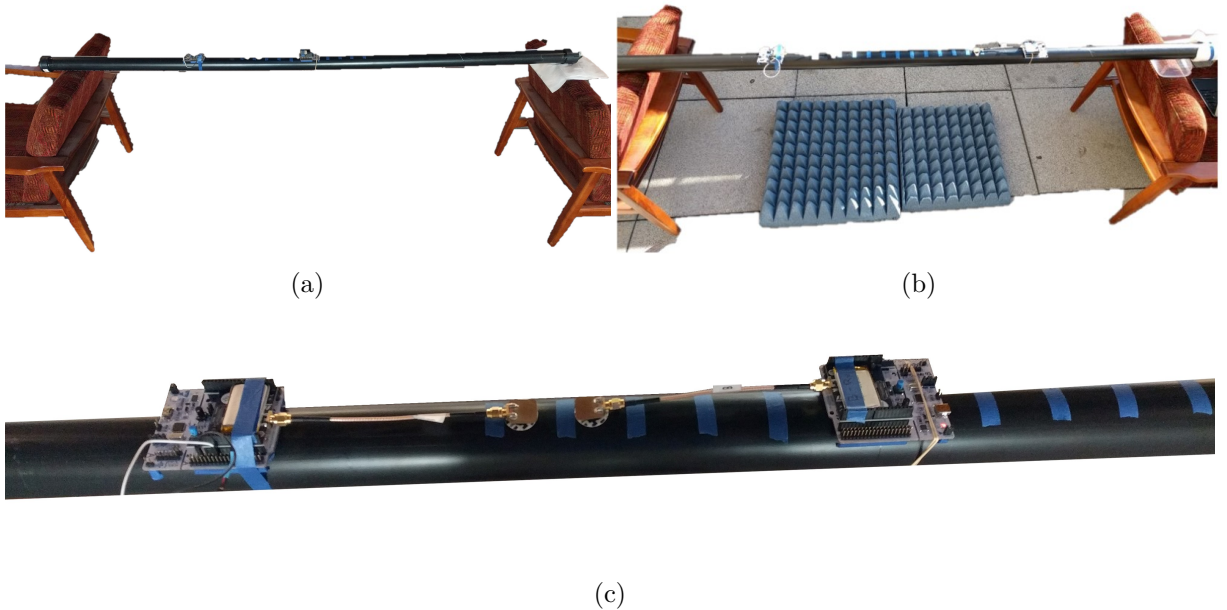
Figure 3.31: Prototype test setup: (a) on phantom, (b) with EM absorbing foam, (c) enlarged

The results are presented in figure 3.32 over distance for three different frequencies: (a) 420 MHz, (b) 450 MHz and (c) 510 MHz. Each sub-figure plots three curves: the simulated path loss in yellow and the measured attenuation with and without the foam in blue and orange respectively.

A weak measurement point is present for all frequencies at 30 cm in the configuration with foam (all frequencies are covered at once for a given distance and then the new distance is set). The Tx and Rx electrode might have been misaligned during the recording, and more specifically, one might have been tilted in comparison to the other. We know from the simulation results that the electrode is strongly polarized perpendicularly to the conductive surface. Consequently, a tilted electrode will suffer from an attenuated signal since a portion only will be recovered on the Rx side.

Besides the above-mentioned isolated result, the measurements under both circumstances and the simulation show a great agreement. Most results are contained with a 5-7 dB window and the trend over distance is similar. This result is key as it validates the model and the type of simulations performed, granting credit and confidence in the results obtained so far. It confirms the assumption and hypotheses made regarding the propagation mechanism mode.
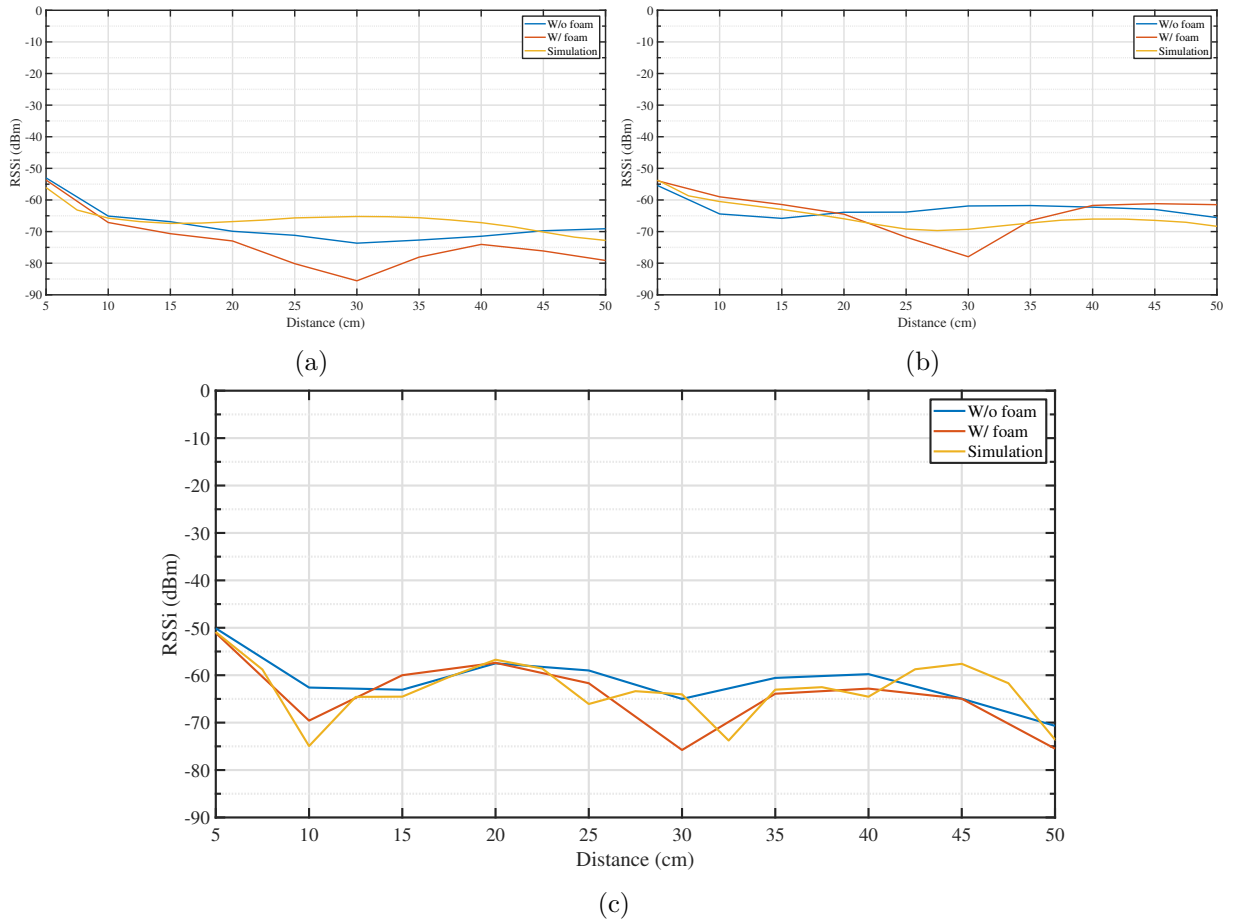
Figure 3.32: Path loss on pipe measured and simulated for (a) 420 MHz, (b) 450 MHz and (c) 510 MHz

The local maxima, minima, or the flattened portion of the curves correspond to the half-wavelength frequency of excitation in the air. For instance, at 510 MHz, the wavelength is $\lambda_{510} \approx 58.8$ cm, confirming a local minimum between 25 cm and 30 cm and foreseeing the following after 50 cm.

3.3.2.4 Measurements on Body

On-body measurements are the channel characterization final stage. The goal is to evaluate and conclude regarding the hypotheses and intermediate results we obtained from theory,

simulation, and measurements (in the lab and prototype-based). They were performed on a real human (volunteer), representing the closest situation from a real application under normal conditions.

All tests are performed three times under the same conditions for repeatability purposes and averaged for plotting. We explored multiple distances between electrodes on a human arm for the 10 different frequencies as previously introduced. The same subject was standing with both arms along the body (vertically). No other pre-gelled electrode but the two required were present on the body for each measurement (see Figure 3.33). Similar to the free space and on-phantom measurements, the prototype boards were positioned as far as possible from one another. A new pre-gelled skin electrode was ensuring the connection with the body, guaranteeing the same level of wetness and stickiness. The recording was performed from 5 cm to 50 cm by steps of 5 cm, from the wrist, and moving toward the shoulder. Paper tape was used to hold the boards in place during the measurement.
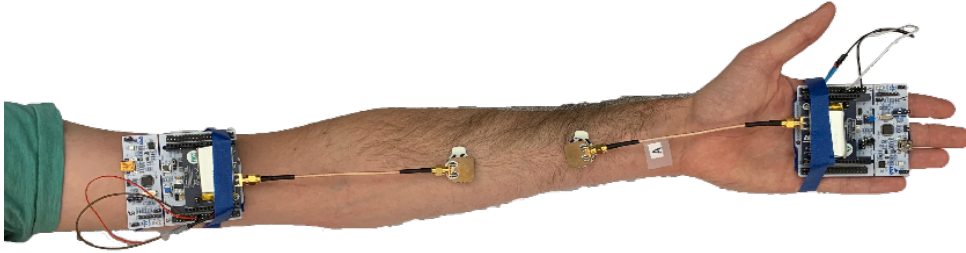
Figure 3.33: Prototype positioned on arm - Tx and Rx

The results are presented in figure 3.34(a) over distance for all the recorded frequencies. Besides a few data points such as 470 MHz and 480 MHz at 15 cm and 490 MHz, 500 MHz, and 510 MHz at 35 cm, all frequencies show a very similar pattern over distance in terms of path loss.

Theoretically un-predicted (neither from simulation), spikes are observed in the path loss over distance. While preliminary results were showing an exponential decay over distance, abrupt changes highlighting fewer losses in the communication channel are identifiable, for all frequencies evaluated. Two main reasons are suggested to justify such results. First, all analyses performed so far (theoretical, simulation, and measurements on phantom) were considering a homogeneous communication medium. The human body is far from being a single layer homogeneous medium. Seconding this hypothesis, all three spikes correspond to the following locations on the subject's arms: the elbow joint, biceps, and shoulder joints, 25 cm, 35 cm, and 50 cm away from the wrist respectively. Those particular locations are a complex interconnection of muscles, ligaments, and bones. The second reason takes into consideration the geometry and body shape. Studied in figure 3.15, the medium cross-section can significantly impact the path loss.

Those results can also be plotted over frequency for a given distance. Figure 3.34(b) presents the path loss for 20 cm, 30 cm and 40 cm communication distance for discrete frequencies from 420 MHz to 510 MHz. A flat and bounded path loss is observed over frequency within a 5 dB window for all three situations. Limited variability is recorded. However, it must be noted that RSSi variations are greater for frequencies around the open ISM band at 433 MHz. The ambient noise is also plotted, not differing much from one distance to another as expected. This observed behavior shows a great agreement with theoretical and simulation results (see figure 3.14). It confirms, under real condition, an interesting characteristic of C-BCC: a wide bandwidth available with solid and regular behavior over 100 MHz (in terms of bandwidth) and maybe more based on simulation results. The attenuation recorded with our setup does not exceed 75 dB at 45 cm. In comparison with the results obtained with the VNA earlier, the attenuation is 20 dB to 25 dB worse here (see figure 3.23 and figure 3.24). This difference was expected and already highlighted in [45].

(a)

(b)
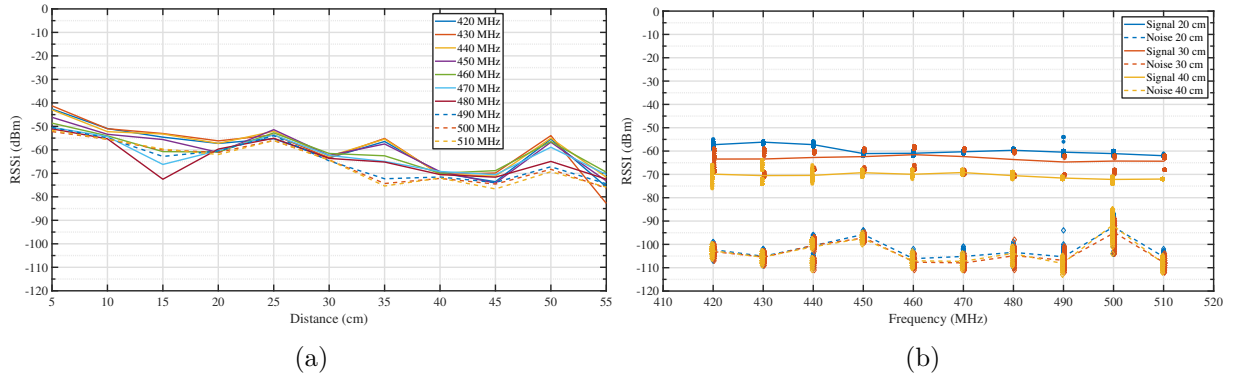
Figure 3.34: Path loss measured with the prototype: (a) for multiple frequencies over distance, (b) for multiple distances over frequency

In the previous scenario, the electrodes were located on the arm following a line-of-sight configuration. No obstacle was disrupting the communication path and a straight line was available between the transmitter and the receiver. A second on-body configuration was investigated: torso-to-back communication. It is one of the most delicate paths on a human body-deployed network (tissue absorbing radiations, shielding, non-line-of-sight, multi-path...).

The back-to-torso path loss is presented in figure 3.35 along with the 40 cm in line-of-sight attenuation as a reference. Besides the electrodes' locations, the test condition was identical. It is observed that the channel characteristics are showing high similarities with a low variability for each data point but a bit more spread out in terms of attenuation over frequency.
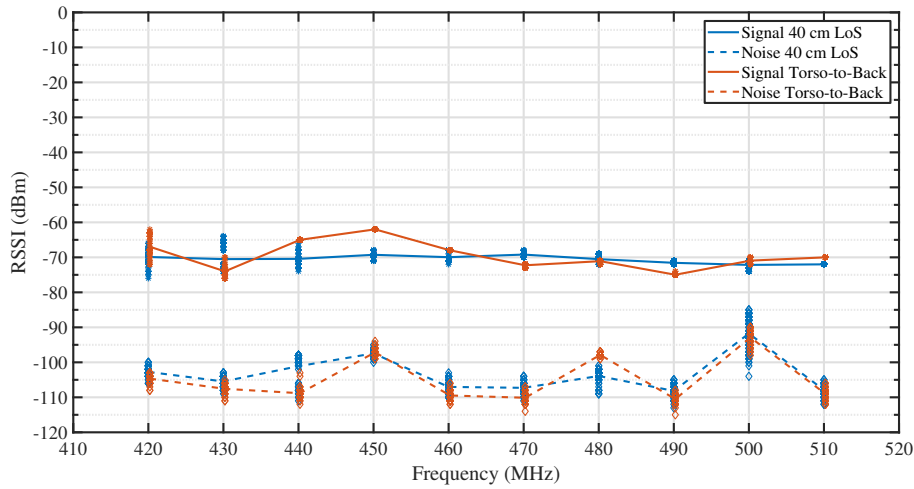
Figure 3.35: Path loss comparison, line of sight vs. non line of sight

The on-body results were presented above in a realistic situation (i.e. employing small form factor battery-powered prototypes) highlighting expected results from theory and modeling analysis for a fixed distance. A "free-space versus on-body" comparison under the same distance and frequency conditions was conducted. The idea was to verify one of the initial hypotheses suggesting that the human body could improve the path loss (i.e. fewer losses observed). Figure 3.36 presents the attenuation (solid lines) for a set distance of 20 cm over frequency in free space (blue) and on body (orange). The noise level is also plotted (dashed lines) as well as the scavenged power (dotted lines) which setup was presented figure 3.30. Under those circumstances, the free space path loss is at least 20 dB weaker (from 430 MHz to 440 MHz) and up to 40 dB worse (510 MHz) while running the same hardware. In terms of behavior over the considered frequency band, the on-body attenuation is almost flat (within a 5 dB window) while the variation in free space is spread over a 30 dB window (from the maximum to the minimum recorded). We observed a greater path loss variability on the body compared to the free space

situation for the same distance-frequency pair on-body. Even if the subject was standing still during the measurement, minor movements could tilt the electrodes, directly impacting the link quality. The on-body noise level is slightly higher (about 5 dB) over the entire bandwidth. The scavenged signal amplitude is showing a high degree of similarity for both measurements. However, the received power while the electrodes are located on-body is greater than the scavenge signal intensity. It is not the case for free-space measurements.
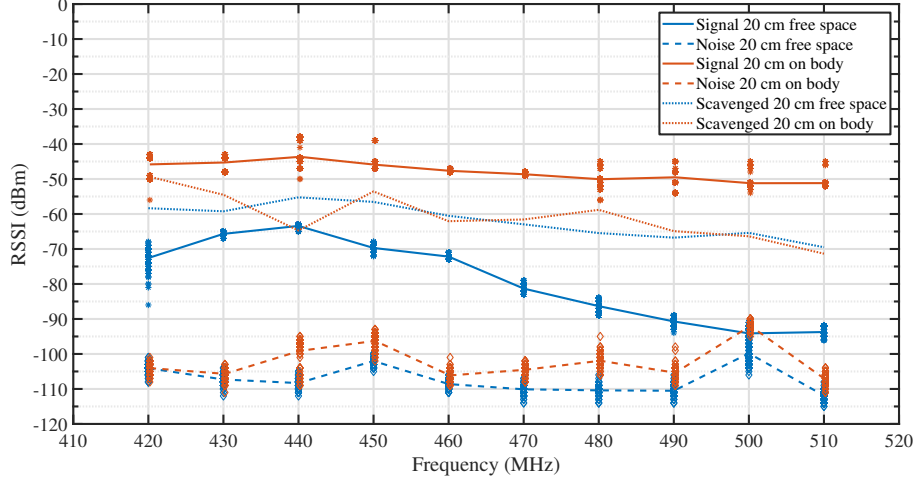
Figure 3.36: Path loss comparison, on body vs. free space

These last results conclude our on-body measurement phase and confirm Capacitive Body Coupled Communication behave as expected and even better with non-line-of-sight abilities.

3.3.3 Wrap-up

The channel characterization performed in this section showed expected behavior from simulation and both results were well aligned, in free space as well as on-body. A first stage path loss study was intended with the VNA despite the questionable validity of this method based on the state of the art results. The encouraging path loss recorded lead us to implement a fully-battery powered prototype for the transceiver and the receiver. This new and unique configuration proposed a testing and measuring environment with a high degree of similarity with potential product implementation, in terms of form factor and operating mode. The real channel loss was measured, facing a greater attenuation than with a VNA, as expected but still capable of establishing communication over the body. This ultimate channel characterization stage also confirmed the results obtained over the different steps of our investigation from theory to simulation.

With a fully characterized C-BCC channel, capable of enabling communication using the human body as a communication medium. The following section summarized our results and proposes a channel model.

3.4 Proposed Channel Model and Operating Frequency

The channel characterization performed and presented above lead us to gather all those results within an accessible yet realistic channel model. A significant part of this chapter, including the current section was published in [67] ("Capacitive body-coupled communication in the 400–500 MHz frequency band," in EAI International Conference on Body Area Networks. Springer, 2019, pp. 218–235) and presented at Bodynets 2019 conference, Florence, Italy.

3.4.1 Channel Model

Based on the results obtained from the channel characterization, great coherence was highlighted between theoretical, simulation, and measurement results. It validates the hypothesis

and understanding of the occurring propagation phenomena. Consequently, we sought for combining the fit introduced in section 3.2.3, figure 3.13 and the real measurement results from section 3.3.2.4, figure 3.34(a).

These measurements were split for each harmonic frequency and fed into a log-linear least-square fit in equation 3.7 according to the channel loss (L) model [17]:

$$L = \begin{cases} L_0 & d = d_0 \\ L_0 + \alpha_0(d - d_0) & d_0 < d < d_1 \\ L_1 + \alpha_1(d - d_1) & d_1 < d \end{cases} \tag{3.7}$$

with d the inter-electrode distance, L_0 the baseline channel loss at the shortest measured inter-electrode distance (d_0, 5 cm in this case), d_1 is the boundary distance where the transition between the quasi-static (QS) and surface wave regimes occurs. Following the analysis shown in Fig. 3.2, a boundary distance d_1=15 cm was determined for the studied frequencies on muscle. Hence, this value was chosen in the fit to determine the channel losses per unit distance α_0 and α_1 in both regimes.

Table 3.1 lists the parameters' values of the fit described in Eq. 3.7 for the following frequencies: 420 MHz, 450 MHz, 480 MHz, and 510 MHz.

Table 3.1: Channel loss parameters.

	420 MHz	450 MHz	480 MHz	510 MHz
L_0 (dB)	-43	-47	-49	-52
α_0 (dB/cm)	-1.2	-0.95	-2.1	-0.79
L_1 (dB)	-54	-55	-62	-59
α_1 (dB/cm)	-0.41	-0.37	-0.19	-0.45
σ (dB)	6.8	6.5	5.8	5.9

Fig. 3.37 shows the measured channel losses at 450 MHz with a fully battery-powered setup, as a function of distance along the arm of the subject. The baseline channel loss at 5 cm (L_0) is -47 dB, while the loss at the transition point L_1=-55 dB. The fit resulted in two distinct slopes defined by the channel losses per distance α_0=-0.94 dB/cm and α_1=-0.37 dB/cm. The standard deviation (σ, see Eq. 3.7) on the channel loss model is 6.5 dB. The results of this fit are in line with the model proposed in Equation (3.3) with a dominant QS wave near the electrodes (highlighted by a steeper slope), and the surface wave dominating the propagation after the transition point (lower curve coefficient). Ultimately, one can observe spikes in the channel loss at 25 cm, 35 cm, and 50 cm from the source. Those particular points correspond to the subject's elbow, biceps and elbow respectively. The could be explain by the human body non-homogeneity and potential interference. Finally, given the real measurement results, the model shows the main trends over distance.

Baseline channel loss increased with the frequency which is in line with [68]. Near-field losses over the distance between 0.8 and 2 dB/cm were measured. These were higher than the far-field losses which were between 0.2 and 0.5 dB/cm. These results are in line with the theoretical model detailed in section 2.

3.4.2 Operating Frequency

The operating frequency is a topic of importance while deploying Body Coupled Communication and especially Capacitive-BCC. Detailed in chapter 2, most reported work, and C-BCC implementations are operating at frequencies below 200 MHz. A classic and widely spread C-BCC representation in terms coupling and communication mechanism is presented figure 3.38 (similar to figure 2.14(b) from section 2). As mentioned in section 3.1.3, this representation is only valid for the lower part of the spectrum: a few tens of MHz [42].
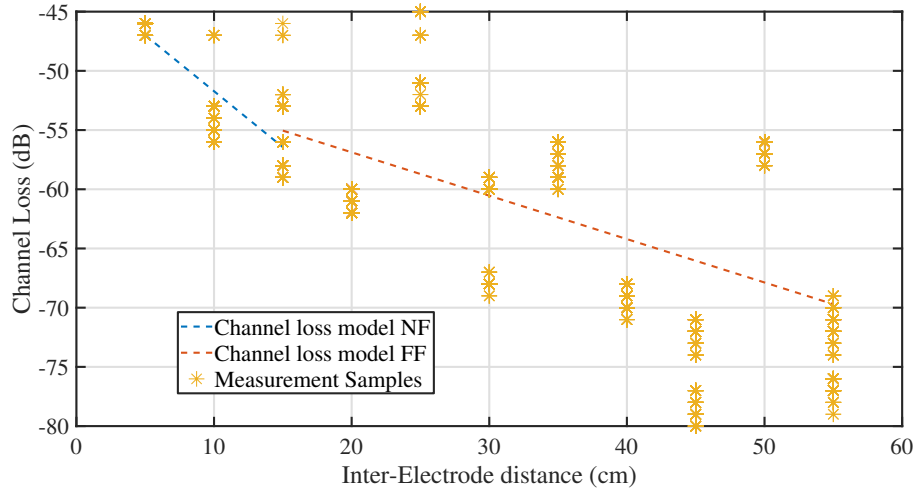
Figure 3.37: Path loss measured and channel model
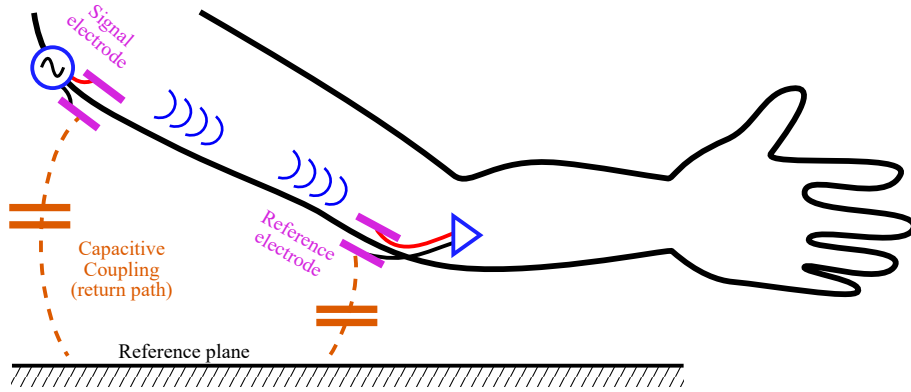
Figure 3.38: Common C-BCC representation mechanism

In fact, at a lower frequency, the wavelength is so important compared to the considered distance that the dominant propagation phenomenon is the quasi-static wave. Consequently, the capacitive coupling with the environment must be taken into account. Several publications and studies were relying on such model [13,14,42] and its derived electrical representation giving a good estimation.

However, within those publications, high sensitivity to the ambient noise was reported [15,42]. The distance with any device such as a fridge, vending machine... could significantly increase the noise in the communication channel [15]. Other implemented a shield around the transmission board to isolate the device from any interferer: efficient but very impractical.

Investigated and demonstrated in section 3.3, operating at higher frequency changes the physics behind the propagation. A signal frequency between 400 MHz and 500 MHz makes the surface wave becoming the dominant propagation phenomena as soon as the distance covered is greater than 12-15 cm. The immediate consequence is a major reduction of the channel sensitivity to ambient perturbations. The receive signal strength depends only to a very limited extend on the return path created by the coupling of the reference electrode to the environment. In practice, it increases the system robustness and relaxes the hardware constraints to mitigate body dynamics.

Increasing the frequency of operation showed another channel property: the wide bandwidth available offering a constant attenuation throughout the entire band tested. Our investigation (in theory and practice) confirmed a 100 MHz bandwidth when operating at 450 MHz (50 MHz on each side). This is much wider than any other reported work and enables pulse-based wide-band communication at 450 MHz. Depending on the pulse shape and duration, the occupied

spectrum in the frequency domain can be controlled as presented figure 3.39. The interest is dual: several data rates can be envisioned with the same hardware as it just depends on the pulse rate. Second, a wide-band approach helps for body shape mitigation. Figure 3.15 showed that the optimal frequency of operation depends on the limb size; wide coverage allows a consistent average behavior over the human body.

(a)   (b)
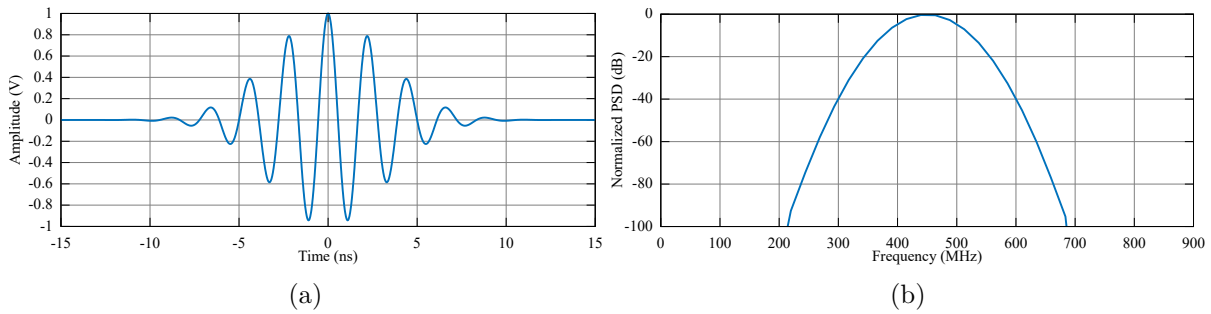
Figure 3.39: Pulse-based communication, (a) time domain, (b) frequency domain

A higher frequency of operation also allows a smaller electrode size, making the device more acceptable and comfortable for a wearer. It is important to take this aspect into account as the device aims to be widely deployed over a human body.

3.4.3 Wrap-up

The frequency of operation of 450 MHz seems to offer promising specifications to enable the communication over the human body with great robustness, low sensitivity to the environment, and an acceptable form factor in terms of electrode size. One can wonder why the frequency of operation is not even higher as it seems to bring only positive addition. In fact, the higher is the frequency the more attenuation we are facing, as depicted in figure 3.23 and 3.24. Consequently, the transmitted power needs to be increased, leading to higher power consumption and also higher radiated power in the air which is against one of the main interests of Body Coupled Communication.

3.5 Comparison with Other solutions

A wide variety of wireless technologies exists for implementing Wireless Body Area Networks (WBANs) as presented in section 2.1. However, it was still unclear how their performance compares in true on-body scenarios. The need for a rigorous and apple-to-apple comparison leads us to perform measurements for a single on-body reference scenario to analyze six different RF technologies in terms of path loss from 420 MHz to 2.4 GHz. The results presented in this section were part of a published study [68]: "A comparative study of on-body radio-frequency links in the 420 MHz – 2.4 GHz range," in Sensors, vol. 18, no. 12, p. 4165, 2018. This work was carried out by several Ph.D. students, postdocs, and researchers from Berkeley Wireless Research Center (BWRC - UC Berkeley, California), adapting their research to perform measurement on-body in the selected scenario.

3.5.1 Reference scenario

The aim of the reference scenario, similar to the one presented in section 3.3.2.4, was to compare path loss as a function of distance for the same given scenario using different wireless technologies for on-body communication at various frequencies. The IEEE 802.15.6 standard for on-body communication allows frequencies from 400 MHz – 3.5 GHz. The different wireless technologies considered, use frequencies from 420 MHz – 3 GHz. The path loss is defined here as the ratio of the received power and the input power as a function of distance. The reference scenario is depicted figure 3.40. A transmitter node (Tx) is located on the left wrist of a male subject (30 years old, height 191 cm, mass 83 kg) in an upright anatomical position.

Consequently, the Tx position was 93 ± 5 cm above the floor. A receiver node (Rx) is placed on the same arm at different separation distances (d) from the Tx. This attenuation (path loss) is measured over distance, from aperture to aperture along the arm, and is varied from 10 cm to 50 cm by 5 cm-steps. All measurements are executed in an indoor environment. This reference scenario is chosen as it represents a commonly targeted on-body application where a wearable device such as a prosthetic is worn on the wrist and communication along the arm with another body-worn RF node is required.
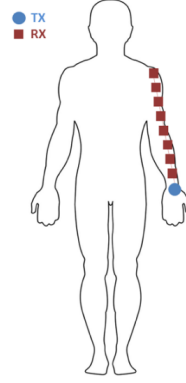
Figure 3.40: Reference scenario

3.5.2 Compared technologies

Six different wireless technology were studied. They are illustrated figure 3.41 and detailed below.
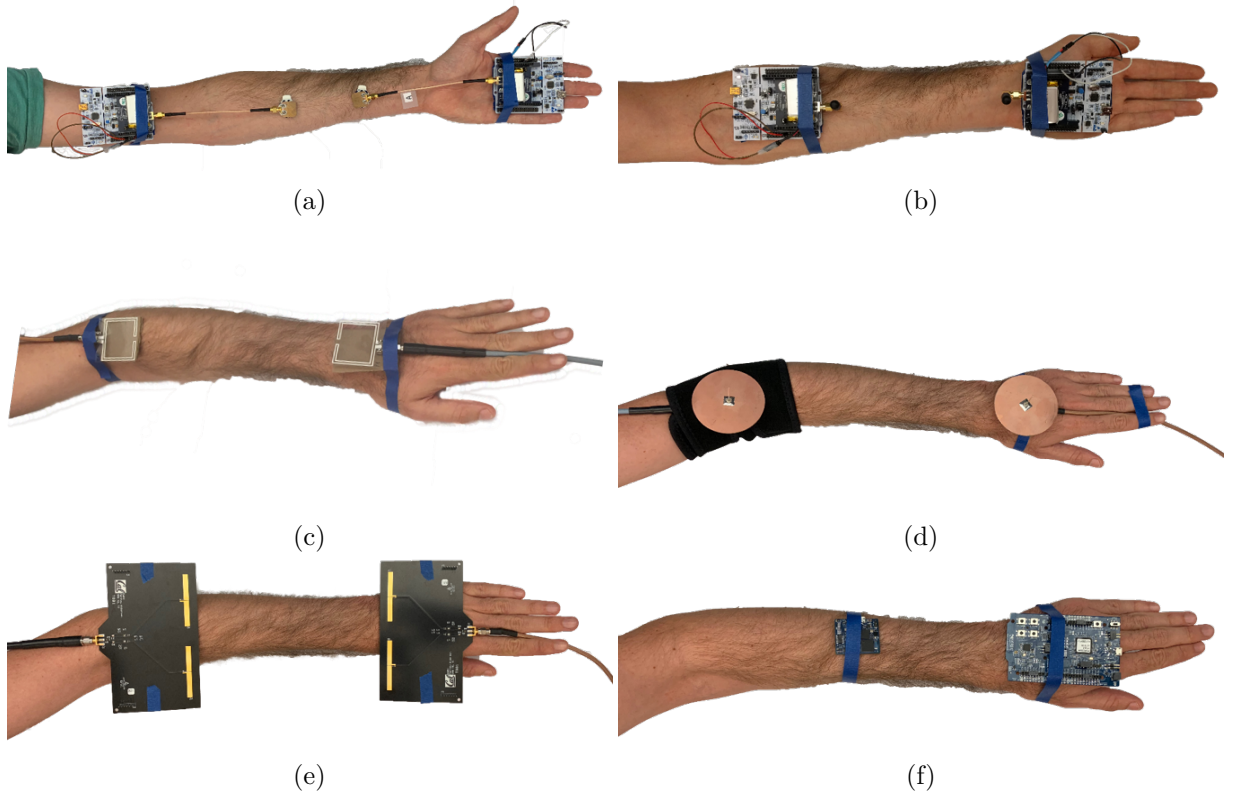
Figure 3.41: Technologies compared in the same scenario (a) 450 MHz BCC, (b) 450 MHz Monopoles, (c) 915 MHz Printed dipoles, (d) 2 GHz Monopoles, (e) 2 GHz Dipole arrays and (f) 2.4 GHz Bluetooth nodes

Pictured in figure 3.41(a) and (b), are respectively BCC and on-body monopole technologies,

both operating at 450 MHz. Their propagation mechanism is different, but they share the same hardware (apart from the coupling/radiating element). The prototype in place for measuring BCC is the battery-powered prototype introduced section 3.3.2.1. The on-body monopole version uses the same hardware with coupling electrodes replaced by monopole antennas provided within the development kit.

Pictured in figure 3.41(c), 915 MHz printed folded dipoles, about 41×45 mm, for UHF RFID were part of the comparison. UHF RFID is mainly used for passive wireless identification of objects. However, the new generation of the UHF RFID standard also allows for the passive transmission of sensor data from the tag (i.e. the remote, passive antenna-IC-sensor system) towards a reader (i.e. a powered system with an antenna and an RFID compatible radio [17]). This makes this technology an interesting option in WBANs since it allows one to place the energy source in a central hub and work with passive tag(s) on the other side of the link. The data were recorded with a VNA registering two-port S-parameters (S_{11}, S_{12}, S_{21} and S_{22}). For each position, 50 measurements were executed from 865 MHz to 965 MHz with 501 frequency steps (sweep time 5.3 ms). The antennas were placed on the body in two configurations: orthogonal to the skin and parallel to the skin.

The fourth tested technology is shielded monopole antenna at 2GHz as illustrated figure 3.41(d). They could overcome the de-tuning issue due to the proximity with the human body with their ground plane aligned with the body. For this research, path loss measurements are performed with radially symmetrical shielded monopoles, tuned at 2 GHz. This frequency was selected because it results in a considerably smaller antenna size in comparison to 420 MHz or 900 MHz antennas. The 2.4 GHz ISM band was avoided to prevent interference during our measurements. The design of the antenna is presented as follows: A 37.5 mm monopole sticks out of a 72 mm FR4 disk with a double-sided copper ground plane. The S-parameters are measured with the VNA described above. Each configuration is measured 50 times with a frequency span of 500 MHz – 3 GHz with 501 frequency steps (sweep time 5.3 ms).

To evaluate the on-body performance of RF antenna arrays, a linear antenna array consisting of two 2.05 GHz half-wavelength dipoles was used. The array has an antenna-to-antenna spacing of 75 mm (or approximately half a wavelength) and is arranged to maximize broadside radiation and minimize antenna interaction. Details of the array design can be seen in figure 3.41(e). Each matched dipole antenna is fed via an approximately one-wavelength long differential microstrip transmission line and terminated with an edge mount SMA connector. Each antenna in the phased array can be driven independently via its own SMA connector to steer the array's beam. These arrays were leveraged from the work done in [69]. Dipole antennas are chosen because they are an efficient solution for planar, uniform, linear arrays.

The last type of wireless communication evaluated is the widely used and deployed Bluetooth technology operating between 2400 MHz and 2485 MHz. For our study, two Bluetooth nodes, one custom-made transmitter [70] and a commercial receiver, were placed in the on-body locations shown in figure 3.41(f). The RX node registered RSSI values in dBm over time, which are treated as a proxy for received power in this study. 100 samples are retained per TX-RX separation distance.

3.5.3 Results

Each of the wireless technologies has a different method of (indirectly) registering received power on the Rx nodes. The latter are all converted to values in relative transmitted power: the ratios of the received power over the input power (P_{dB}) in dB. These are fed into a log-linear least-square fit for each technology using the two path loss models [71] in equation (3.8) and (3.9).

$$P_{dB}(d) = P_0 - 10n \cdot \log_{10}\left(\frac{d}{d_0}\right) + N(0, \sigma_p^2) \tag{3.8}$$

with P_0 the path loss at the reference distance d_0 of 10 cm, d the separation between Tx and Rx, n the path loss exponent, and $N(0, \sigma_p^2)$ quantifies the (zero-mean) path loss lognormal variance. σ_p is the standard deviation on the path loss model. This path loss model is used frequently when quantifying (on-body) path loss measurements in indoor environments [71]. While this model is simplistic, it uses only three parameters, and is therefore easier to interpret physically and allows an intuitive comparison over different frequencies and technologies.

An alternative model is given by equation (3.9):

$$P_{dB}(d) = P_0 + 10 \cdot log_{10}(e^{(-m_0 d)}) + N(0, \sigma_p^2), \qquad (3.9)$$

This second model uses an exponential loss in power as a function of distance. m_0, is the loss per unit of distance. $N(0, \sigma_p^2)$ is again a term quantifying the lognormal variance on the path loss, and P_0 is the baseline path loss.

These path loss models are fitted to our measured data per technology and frequency. Path loss is in general a good metric for important link parameters such as communication range, packet delivery ratio, coverage, required transmitted power, etc. [72]. Minimizing the path loss influence is therefore an important aspect of optimizing wireless links.

Following model 1, P_0 ranges from -14 dB for the folded dipole antenna at 915 MHz down to -62 dB for the 2.4 GHz Bluetooth nodes. Based on model 2, P_0 varies in a similar range from -13 dB down to -62 dB for the same technologies. The path loss exponent, n (only in path loss model 1) varies from 1.7 for Bluetooth up to 3.2 for the 450 MHz monopole. A lower value than other technologies was obtained with the antenna parallel to the body at 915 MHz where n is 0.57. The attenuation per unit of distance, m_0, in model 2, ranges from 0.23 dB/cm up to 0.52 dB/cm for the Bluetooth nodes and the 450 MHz monopole, respectively. Similarly to the path loss exponent, the 915 MHz parallel antenna technology shows a significantly lower value of 0.087 dB/cm. The lognormal standard deviation according to model 1 ranges from 1.3 dB at 2 GHz to 6.2 dB for BCC operating at 450 MHz. In model 2, these standard deviations go from 1.1 dB for the 2 GHz monopole to 6.2 dB for BCC as well. The path loss model parameters are summarized in table 3.2.

Table 3.2: Path loss models parameters.

Technology	Model 1			Model 2		
	P_0 (dB)	n	σ_p (dB)	P_0 (dB)	n	σ_p (dB)
420 MHz Monopole	-21	3.2	2.8	-19	0.52	3.6
450 MHz BCC	-52	1.8	6.2	-51	0.30	6.2
915 MHz Parallel	-44	0.57	2.6	-44	0.09	2.6
915 MHz Orthogonal	-14	2.5	1.9	-13	0.38	1.8
2 GHz Monopole	-19	2.0	1.3	-17	0.34	1.1
2 GHz Array	-25	2.4	1.3	-24	0.39	1.9
2.4 GHz Bluetooth	-62	1.7	1.8	-62	0.23	2.4

Figure 3.42 shows the path loss, normalized to P_0, for the seven studied conditions in the reference scenario. Excluding the measurements at 915 MHz with the antenna parallel to the skin, all path loss curves are clustered along with a similar trend. This particular mesurement is excluded due to its unexpected results, potentially due a favorable configuration of the antennas in a line of sight on a standing still subject. None of the path loss models predict a loss exceeding 25 dB over 40 cm propagation along the arm.

The baseline path loss (P_0) varies severely between the different studied technologies. In general, those configurations with an antenna orthogonal to the skin surface (monopole at 450 MHz, printed antenna orthogonal to the skin at 915 MHz, and monopole at 2 GHz) have a lower initial
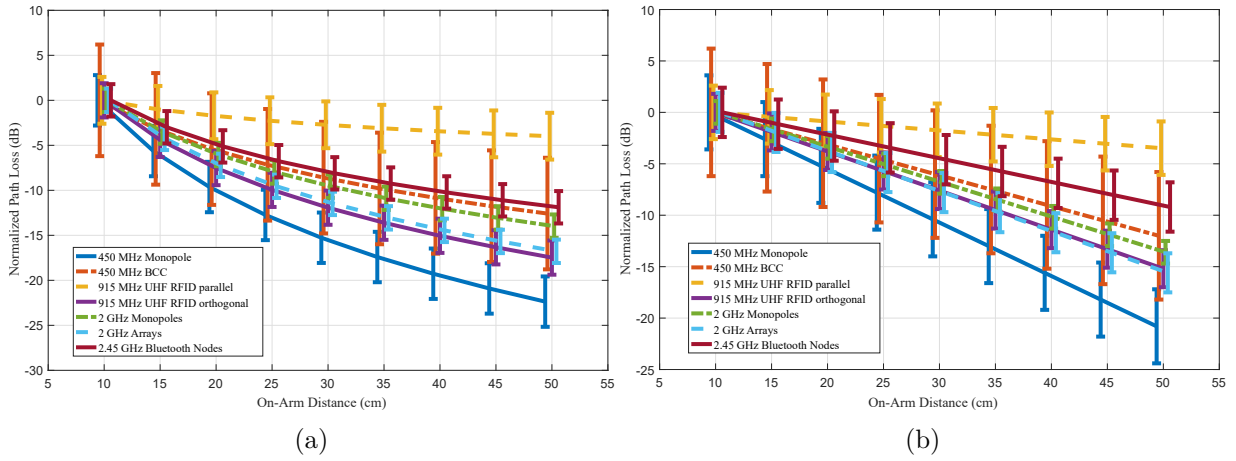
Figure 3.42: Normalized path loss models as a function of distance in the reference scenario (left arm) for the seven studied configurations: (a) Model according to equation (3.8), (b) Model according to equation (3.9). The lines indicate the models described in Table 3.2, while the "error bar" are standard deviations (slightly shifted for figure clarity).

path loss than the other studied techniques at the same frequencies. P_0 is similar for the 2 GHz antenna arrays and the 2 GHz monopole. Their size and operating frequency being similar, these results were expected. Their attenuation per unit distance is also in the same range. The same observation is made for Bluetooth. However, it suffers from a higher initial loss which is primarily due to the usage of ceramic and PCB antennas, optimal for board integration at the cost of higher losses.

3.5.4 Conclusion on compared technologies

The sub-GHz RF orthogonal technologies (915 MHz antenna orthogonal and 450 MHz monopoles) provide the highest P_0. This is explained by three factors: lower frequency of operation, the optimized configuration where both antennas linear polarization were parallel, and a relatively high distance between antenna and body due to the test setup decreasing the impact of the body on the measurement, as shown in [73]. Table 3.2 highlights two groups: (i) technologies well described and fitted with our theoretical model, (ii) BCC, where the results variance is greater. This variance can be explained by the C-BCC sensitivity to movement due to the electrode design. A variation in the contact strength between the electrode and the skin changes the impedance, impacting the channel loss. Furthermore, a movement could tilt one electrode in comparison to the other, also impacting the channel attenuation. This effect was observed at discontinuities (elbow and shoulder) in the medium since BCC uses the body itself as a communication channel. BCC, due to its topology without matching network due to the direct on-body contact and communication mechanism, presents one of the lowest P_0. BCC appears less efficient than regular RF in a line of sight configuration. Its attenuation over distance is greater but its flatness over a wide frequency band is higher (in comparison with narrow band communication mechanism). Besides, the electrodes used, offer a smaller form factor, are parallel to the body, and do not require any kind of matching network. An important observation is that none of the studied technologies shows a path loss variation of more than 25 dB over a propagation distance of 40 cm. Simultaneously, the differences in P0, even within the same frequency, can be larger than this added path loss over 40 cm. This indicates that the selection of a proper antenna/electrode configuration is extremely important in designing an on-body link.

RF path loss over distance has been measured for six different technologies operating for frequency included in the range: 420-3GHz in a reference on-body scenario: from wrist to shoulder on the left arm. The additional path loss caused by propagating over the arm is smaller than 25 dB for all studied technologies. The baseline path loss at a minimum separation distance

of 10 cm varies between -13 dB and -62 dB and can thus be tuned or optimized by selecting the right RF technology and on-body configuration. The path loss exponents (n= 1.7-3.2) and the propagation loss over distance (m_0= 0.23 – 0.52 dB/cm) are in line with literature [71, 73–76]. These values are relatively close to one another, which indicates that for propagation along the arm (10 to 50 cm) the expected path loss can essentially be considered as frequency independent in this frequency range. Propagation on the limbs experiences significantly less path loss than propagation along the front and back of the torso.

In a conclusion, besides the "entry fee"(P_0), higher for BCC, this technology seems to offer competitive results, especially in a non-line of sight configuration. It is the only one within this comparison offering such a small and convenient form factor, making it a great candidate for system prototype implementation. However, a lot of research and work is still required to improve the coupling element (electrode) to improve the baseline path loss and make the electrode, even more, user friendly.

3.6 Conclusion

This chapter was a dedicated study on Capacitive Body Coupled Communication (C-BCC). Heterogeneous results were available from the state of the art, mostly at a frequency of operation below 200 MHz. It was difficult to gather all the available data within one place with a clear outcome. Nevertheless, C-BCC gave us a glimpse of a great potential to build the Human Intranet. We decided to conduct a full study on this communication mechanism, from theory to in-situ measurements, along with electromagnetic simulations and laboratory investigations.

Given the electrodes' topology, the first hypothesis consisted of considering it as a small dipole. The electromagnetic behavior of small dipole in free space being well known and described, it was used as a reference situation. To predict the on-body electrode behavior as well, we applied the rules of physics for a small dipole on a conductive surface. Based on those theoretical references, we conducted our first calculations, applying to the conductive surface the muscle dielectric properties. The outcome predicted the surface wave dominance as the propagation mechanism for a distance greater than 12 cm for the studied frequency ranges 400 MHz to 500 MHz.

Electromagnetic simulations were conducted. The idea was to validate the theory as well as estimating the future measurement results. Consequently, the electrodes simulated were following a real and implementable design. Free space simulations were performed in first place followed by the on-phantom configuration. The former highlighted a small dipole behavior of our electrode as foreseen in theory while the latter highlighted longer range and stronger E-field magnitude on body than in free space. Other interesting observations were made in terms of behavior over frequency. C-BCC presented a wide frequency range with a fairly flat response to an excitation with a simple electrode. Ultimately, the intrinsic specifications of our electrodes were highlighted such as their impedance and strong polarity.

Those promising simulation results lead us to extend our study by performing measurements on the real electrodes in the laboratory. The electrodes behaved exactly as expected in simulation, validating the results obtain with HFSS and in theory. The small dipole approach was correct. Besides, the flat response over frequency was also highlighted. However, with grounded equipment, the measured path loss was suffering from the electrodes coupling issue, as both reference planes were connected via the equipment.

We assembled a fully battery-powered prototype (transmitter and receiver) to overcome the issue above mentioned. Based on a Nucleo board, we implemented a program capable of self-performing the measurement over a frequency band as wide as 90 MHz by controlling a sub-GHz radio. The prototype was built as similar as possible to a potential future product with a form factor as small as possible. We confirmed the small dipole electrode behavior and their pour ability to perform as an antenna. However, the on-body results were much better, from 20 dB

to 45 dB less attenuation for a distance of 20 cm, highlighting a good coupling and the identified propagation mechanism. We concluded on the idea that the human body was acting as a waveguide, enhancing the propagation, increasing the E-field strength and propagation range. We also confirmed the C-BCC ability to perform non-line of sight (LoS) communication such as torso-to-back, with results similar in terms of attenuation to 40 cm in LoS.

All those results were gathered within a channel model based on real measurement results. Besides, we justified the interest of targeting an operating frequency higher than the state of the art. In fact, with a center frequency of 450 MHz, we access a wide bandwidth as well as a low environmental sensitivity due to the surface wave dominance as the propagation phenomena.

Ultimately, C-BCC was compared to five other technologies, all evaluated over an on-body reference scenario (on the arm communication). C-BCC performed comparably to the others regarding the normalized results. It suffers from higher insertion loss but offers a lower attenuation per unit distance. The insertion loss issue can be addressed by improved electrodes and adaptability to the human body by taking advantage of technologies such as flexible or printed electronics. Last, but not least, C-BCC is the only compared technology offering such a small form factor and a wide bandwidth, two desirable characteristics to build the Human Intranet.

To conclude, C-BCC is a promising communication mechanism for the given application. Our study presents a thorough analysis of the mechanism enabling the communication and the characteristics to expect from such a technology.

4. NETWORK TOPOLOGY

The Human Intranet (HI) is, first and foremost, a network. Chapter 3 dealt with characterizing the Capacitive Body Coupled Communication technology and its ability to enable communication over the human body. Within the current chapter, different network architectures are reviewed based on published studies to establish the Human Intranet skeleton topology. Existing and standardized communication protocols are then investigated. Their specifications make them difficult to apply as is. Nevertheless, several concepts are extracted and reused to build a custom and HI-dedicated solution: a synchronization scheme based on the heartbeat.

4.1 Network Architecture

A network architecture establishes the way the nodes communicate together. It can be very diverse, its selection depends on the network mode of operation (single hop, multi-hop...), functioning requirements (power consumption, security, latency...), and physical deployment (fix or moving node location, connection/disconnection possible...). Different network topologies are studied and their respective characteristics are reviewed. Based on the options analyzed, the Human Intranet skeleton is then established and used as the reference architecture. Its proper characteristics and vocabulary are defined.

4.1.1 Topologies, reliability and Quality of Service (QoS)

A network topology usually belongs to one of the four following families: Star, Mesh, Ring, or a mix called hybrid [77]. Generic representations are proposed in figure 4.1.

A Star network is built around a main node called a Hub. All devices (or nodes) within the network are connected to the hub via a dedicated connection. Direct communication from a node to another is not permitted: all transmitted information must go through the hub. A star network is fairly easy to deploy and offers a low complexity on the peripheral nodes with a single connection. It enables low power consumption on the peripheral nodes as they only communicate when required. However, the hub complexity is much higher as it manages as many links as the number of nodes in the network. If the hub is faulty, the whole network is out of service.

A mesh network is built following the opposite approach. All nodes within the network are connected with a dedicated link. Each node can establish a one-hop communication with all others. It brings the highest level of redundancy and robustness as there is always a way around if a link becomes unavailable. It also offers the possibility for two distinct pairs of nodes to communicate simultaneously without interfering with each other if the physical channel allows it. However, it comes at the cost of complexity as the number of links to establish per node increases linearly with the number of nodes. The total number of links existing within the network increases exponentially ($n(n-1)/2$) with n the total number of nodes.

A ring topology is built following a sequential succession of point-to-point links between two nodes, where the last one is connected to the first one, closing the loop. This type of network is very simple and each node only has two links. However, reaching a node requires multiple hops unless the target is adjacent, limiting data traffic. If a link becomes unavailable, the loop is open and the data traffic issue becomes worse as only one route becomes available.

A hybrid network is a smart mix of the above topologies. It is customized to meet the system needs and adapts to the deployment and other application-related constraints. It requires more complex management as several local scenarios must be covered.
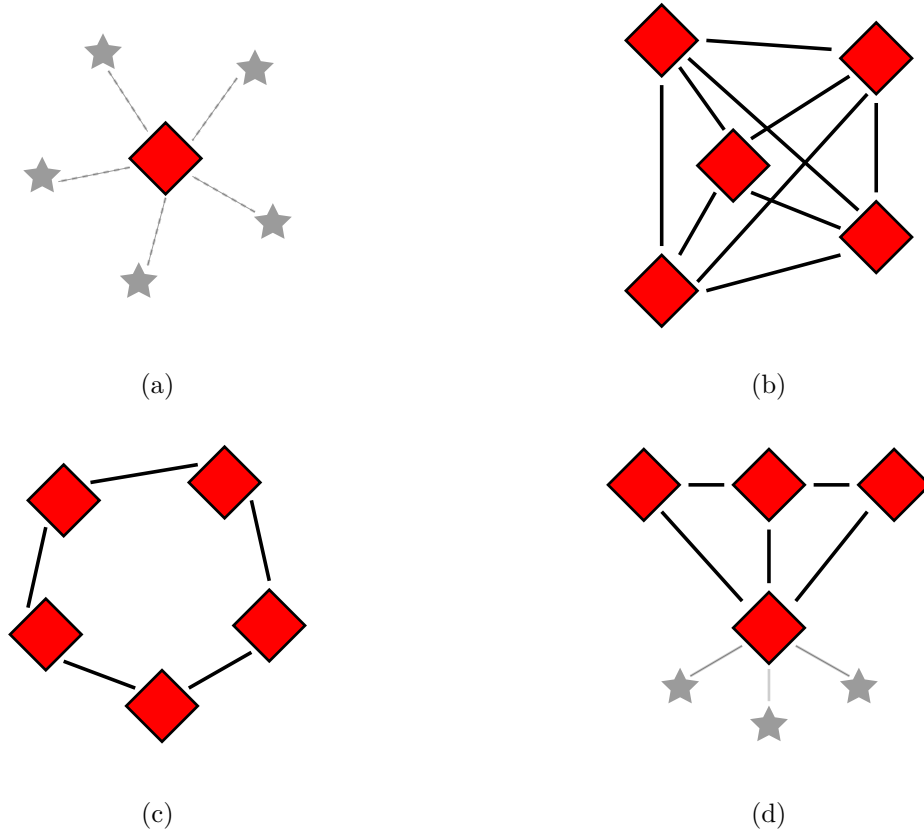
Figure 4.1: Network topologies representation: (a) Star, (b) Mesh, (c) Ring and (d) Hybrid (example).

The Quality of Service is the network's ability to transmit a message from the sending node to the final destination within a given time in addition to a critical chronological order. For instance, a classic use case is a voice or music streaming over the network. The packets must reach their destination quickly enough, keeping the real-time operation mode but also in the order of transmission for intelligibility purposes. It depends on the network architecture (number of routes available, ongoing traffic...) but also on the MAC layer (Medium Access Control) which manages the hardware resources available in the network. The QoS approach described above is also applicable in case of an emergency. Detecting and transmitting the emergency status requires the minimum travel duration as well as the highest processing priority to trigger a relevant response within the lifetime of the emergency.

Besides the QoS introduced above, two other metrics of importance must be considered: the throughput capability and the overall reliability. The latter depends on the network architecture as presented earlier but also on the packet management and routing driven by the MAC protocol and the network layer. A high-reliability degree usually comes along with a higher node complexity and a small payload-to-exchanged bit ratio due to the route decision. It comes to the cost of low throughput and high power consumption due to redundant transmission and higher output power settings.

Choosing the Human Intranet network architecture is critical and a QoS-, Reliability- and Throughput-trade-off is required to optimize the overall efficiency, enabling application critical implementation along with ultra low power nodes.

4.1.2 Human Intranet Skeleton

Star network topology is very common in WBAN with the central node (or hub) collecting data from the peripheral nodes (or sensors) deployed around the body [19]. Star topology

management is included in the IEEE 802.15.6 standard [20]. Unfortunately, despite its simplicity, a star (only) network may not be the best fit to implement the Human Intranet. Body dynamics and coverage may be challenging issues to mitigate with such a topology. On the other hand, a mesh architecture offering multiple routes between two nodes and redundant links, addresses those issues [78], increasing the overall power consumption, reducing the network lifetime as it operates on battery.

This topic is thoroughly addressed in [19]. This publication presents a Human Intranet-oriented approach and established the network capabilities in terms of Packet Delivery Ratio (PDR) and Network Lifetime. The authors considered the network copied on figure 4.2(a) for their analysis. They took into account N nodes with a heterogeneous mix of sensors and actuators, following either a star or a mesh topology. The attenuation between nodes was following a channel model dedicated to electromagnetic waves. The transmitting node output power is set as a parameter influencing the PDR. TDMA and CSMA MAC protocols were compared for a given network topology. For better readability, the authors applied their simulation results with real nodes characteristics copied on figure 4.2(b).

CSMA stands for Carrier-Sense Multiple Access. Under this MAC protocol, the node intending to communicate first checks the absence of on-going traffic by sensing the power level within the communication band(s). TDMA stands for Time-Division Multiple Access. This MAC protocol grants access to a shared communication channel by allocating time slots to the different users.

This study was used as a reference for its clarity, wide State-of-the-art analysis, and directly applicable results to our common objective: build the Human Intranet.
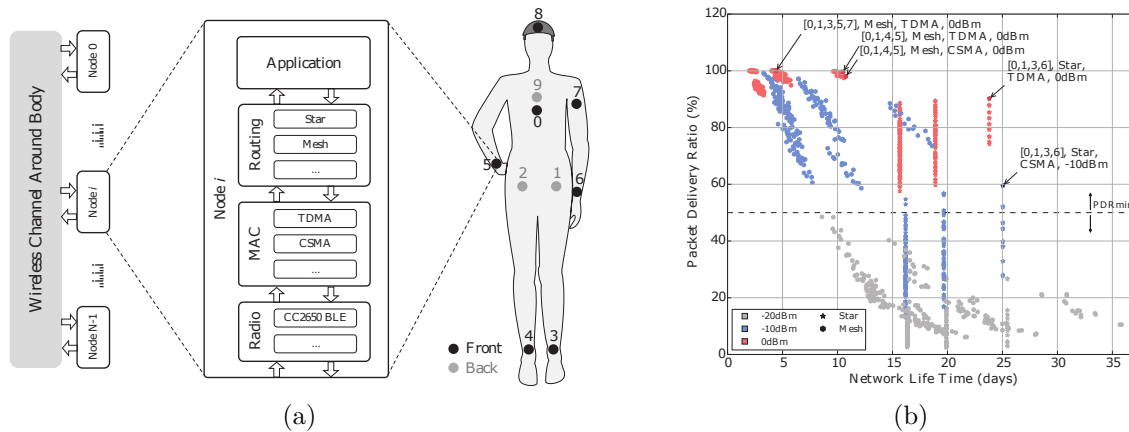
Figure 4.2: Figures taken from [19]. (a) Human Intranet diagram simulated, (b) Reliability and lifetime of the feasible network configurations matching their optimization problem.

The authors point out the best results for a given situation with arrows on figure 4.2(b). The indicated numbers represent the nodes numbers included in the simulated network. From the latter figure, we learn that star topologies tend to be less power-hungry to the cost of a lower PDR unless the radiated power is increased. Following the opposite behavior, meshed networks can reach up to 100% PDR (with an extra node included) to the cost of the network lifetime. The takeaway is the following: early definition of the network requirements leads to the best architecture choice for a given application.

In order to establish the best network topology to build the Human Intranet, Table 4.1 lists a wide variety of bio-signal sensors and the amount of data they can generate based on their sampling rate and resolution [79–81].

From Table 4.1, two types of nodes can be derived: those generating a limited and those generating a significant amount of data. Temperature and heart rate monitoring sensors provide

Table 4.1: Sensor data generation rate

Signal	Sampling rate (Hz)	Resolution (bit)	Data generation rate (bit/s)
Temperature	0.2-2	12	2.4-24
Chemicals	10	12	120
Heart rate	10	12	120
Biometric Z	10-20	12	120-240
Respiration rate	20	12	240
Oximetry	60	12	1440
ECG	120-250	12	1440-3000
Motion (/axis)	100-250	12	1200-3000
Neural recording (/channel)	10k - 30k	12	120k - 360k

from a few to hundreds of bit/s while motion sensing or neural recording can stream from thousands of bit/s and up to 25Mbit/s for a 64-channel implant.

Between those two types of nodes, the recording and transmission capabilities do not require the same hardware, access to energy, and computing capabilities. We accordingly define and split them into two distinct families following their type: "Leaves" and "Hubs". A leaf is meant to be a sensor, following simple implementation, ultra-low power, and energy-efficient. A hub, however, is more sophisticated, embeds extended computing and processing capabilities. It performs more complex sensing. Given its intrinsic characteristics, a hub is also entitled to be an "active node": an actuator.

Following the analysis from [19], the data generation rate from table 4.1 and the subsequent nodes splitting, we imagined a "mesh of star" hybrid network topology. The meshed (or partial mesh) network interconnects the hubs together. As they carry the nodes' intelligence and decision ability, the hubs deal with the highest amount of data and critical information. A meshed (or partial mesh) connection brings the required robustness and reliability. On the other hand, hub-centered, the leaves are connected to a single hub according to a local star topology. It serves the purpose of low power and low complexity implementation from the leaf standpoint. It reduces the number of nodes requiring frequent battery charge in the network and potentially allows a battery-less sensor to be connected. A mesh of star topology brings robustness and extends the end nodes' battery life, keeping a high achievable data rate as depicted in figure 4.2(b). Those characteristics are desirable to build the Human Intranet. An example of such a hybrid network architecture is proposed in figure 4.3. We define a "cluster" as the local star structure composed of a hub and its dedicated leaves.

Displayed on the figure, the link nature and the node-to-node range are detailed below, within section 4.3.3.

4.1.3 Wrap-up

Within this section, existing network architectures and their main characteristics were introduced. From the state of the art and [19] in particular, a clear PDR to network lifetime trade-off was also highlighted. To establish a relevant network architecture for the Human Intranet, two nodes categories were created: Hub and Leaf. The most demanding nodes in terms of data generation, computing power, and, indirectly, access to energy belong to the former while the simpler and low power counterpart belongs to the latter. A hybrid topology is consequently proposed, offering a star topology from leaves to their only and dedicated hub while the interconnection from hub to hub is ensured with a mesh or partially meshed architecture.
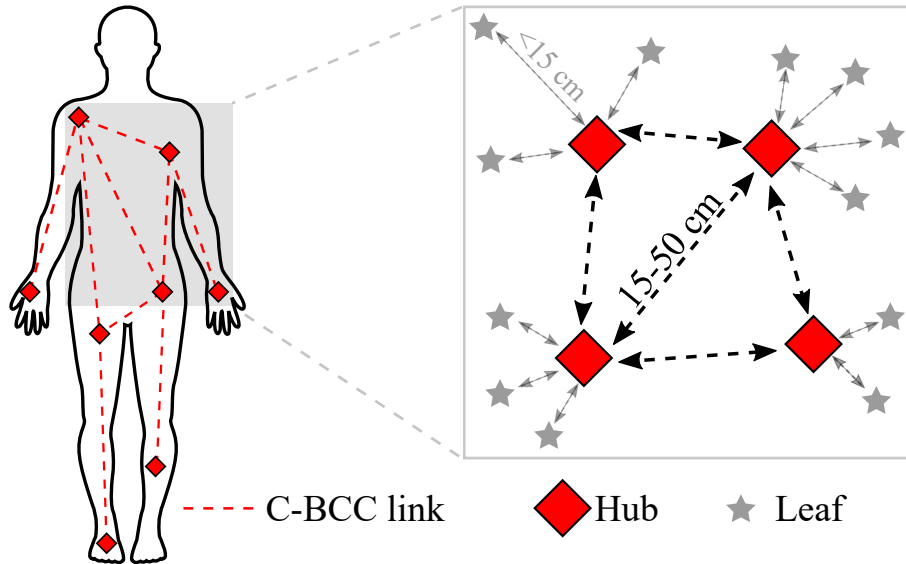
Figure 4.3: Human Intranet Network architecture example.

4.2 Communication protocol

The nodes' deployment, along with their interconnections were presented above within section 4.1. The physical layer ensures the signal propagation such as the channel characterized previously in Chapter 3. A MAC (Medium Access Control) layer, however, is of high importance as it administers the nodes access to the communication channel within the network. An appropriate MAC protocol is essential to build efficient communication in terms of throughput, power consumption, latency... Within this section, two IEEE standards are reviewed and a common low power synchronization technique based on the heartbeat is presented.

4.2.1 WBAN IEEE 802.15.6 and WPAN IEEE 802.15.4

The Institute of Electrician and Electronics Engineers (IEEE) established multiple wireless communication standards such as WiFi and Bluetooth for instance. We'll be reviewing the main characteristics of the following standards: IEEE 802.15.4 [53] and IEEE 802.15.6 [20] dedicated to Personal Area Network (PAN) and Body Area Network (BAN) respectively. They both present specifications, potentially fitting the Human Intranet needs. A comparison summary is given in table 4.2, at the end of the section.

The IEEE 802.15.4 standard, is committed to LR-WPANs which stands for Low Rate-Wireless PAN. It specifies the physical as well as the MAC layers and is the cornerstone for ZigBee [82], 6LoWPAN [83] communication protocols among others.

It offers low power and rate communications, targeting in particular, embedded devices like sensor nodes for instance. This protocol is applicable to star network and supports peer-to-peer topology. Combining the latter with multi-hops routes could offer a greater coverage [84]. The communication can be triggered following an un-slotted CSMA-based (Carrier-Sense Multiple Access) mechanisms, with a continuous-time base, or, following a slotted CSMA mechanism within a time-delimited frame [83]. The latter requires a network master entitled to keep all nodes synchronized [53]. The master (or coordinator) broadcasts beacons grouping the time frames within a superframe (time between two consecutive beacons). Guaranteed time slots can be reserved, dedicating some time for a specific node to communicate.

In terms of frequency of operation, the standard proposes narrow-band communication within the 868 MHz and 915 MHz bands in addition to the 2.4 GHz one. The available data rates span from 20 kbit/s to 250 kbit/s, using one of the following modulation: O-QPSK, BPSK, or ASK.

The IEEE 802.15.4 standard also covers Ultra Wide Band (UWB) as a physical layer tech-

nology [84, 85]. In this case, the signal is spread over a band as large as 500 MHz, implying a low power spectral density. Three bands of operation are defined in the standards for IR-UWB (Impulse Radio-UWB). The first and only sub-GHz band covers the 250–750 MHz range while the others operate at 3.1–5 GHz and 6–10.6 GHz. The standards also define 16 channels out of which 1 must be supported by the device and related to its band of operation. Those channels are 0, 3 and 9, operating respectively at f_{ch_0}=499.2 MHz for the sub-GHz band, f_{ch_3}=4.4928 GHz and f_{ch_9}=7.9872 GHz for the upper bands [53]. The standards also define the preamble code length and the channel allocation for both upper bands, potentially allowing multiple communication ongoing simultaneously without coexistence problem [84]. The data rates with such technology range from 0.11 Mbit/s to 27.2 Mbit/s [53].

The IEEE 802.15.6 standard is however targeting body-centered technologies and networks. Healthcare applications are one of the most important focus, along with wellness and entertainment. It aims at describing the specifications for the PHY and MAC layers [86], similar to the previously introduced IEEE 802.15.4 standard. It covers multiple frequency bands as well as communication mechanisms such as UWB, NB (Narrow-Band), and Human Body Communication (HBC). The standard also details three security levels based on the authentication and encryption mechanisms in place. In terms of network topology, the IEEE 802.15.6 standard is devoted to star topology or a two-hop extended star networks [20, 86]. In any case, one and only one hub (i.e. main/central node/coordinator) must be established within the network [20].

The IEEE 802.15.6 standard MAC layer covers in addition to CSMA, a TDMA frame structure. A combination of both, CSMA and TDMA is also permitted [86]. The frames are defined as the time interval between two consecutive beacons. The hub is in charge of the nodes synchronization and network association. Three hubs-managed modes are established [20, 86, 87]:

- **Beacon mode with beacon periods (superframes):** The beacon initiating the superframe is transmitted first. It is followed by the first set of EAP (Exclusive Access Phase), RAP (Random Access Phase), and MAP (Managed Access Phase). The scheme is repeated a second time and followed by a second beacon and unique CAP (Contention Access Phase). This mode is depicted in figure 4.4.
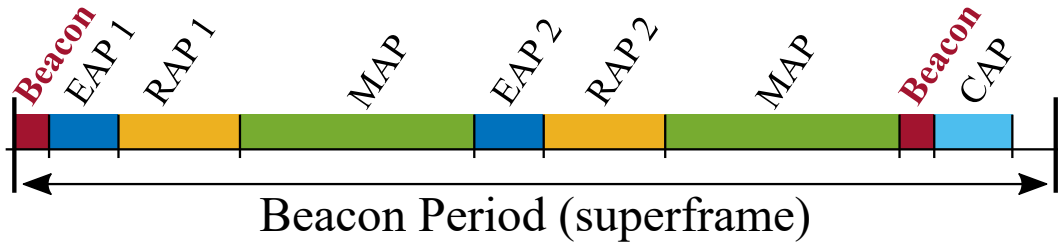
Figure 4.4: Layout of access phases in a beacon period (superframe) for beacon mode.

- **Non-beacon mode with superframes:** The superframe is bounded by two beacons defining a single Managed Access Phase (MAP). This mode is depicted in figure 4.5.
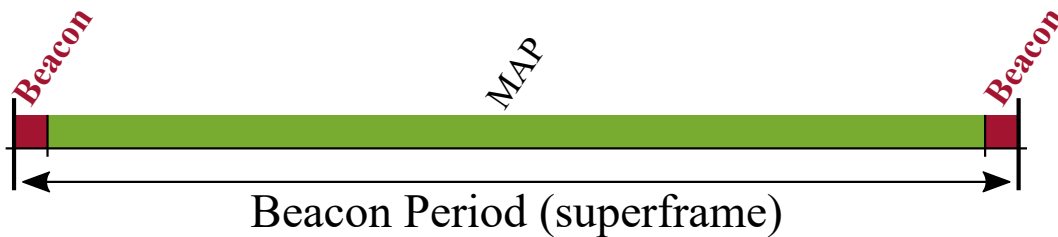
Figure 4.5: Layout of access phases in a superframe (beacon period) for non-beacon mode.

- **Non-beacon mode without superframes:** No superframe is defined as no beacon is sent. It follows unscheduled bilink allocation intervals. A node may treat any time interval as EAP or RAP with CSMA-based random access.

In terms of security, three levels are specified as follows [20, 86, 87]:

- **Level 0: unsecured communication.** This is the entry level. The transmitted frames are not secured by any mean. It does not provide any of the following measure: message authenticity and integrity validation, confidentiality and privacy protection, and replay defense.

- **Level 1: authentication but not encryption.** The data exchanged are not encrypted but the frames are securely authenticated. The following measures are included: message authenticity and integrity validation and replay defense. Hence, no confidentiality nor privacy protections are in place.

- **Level 2: authentication and encryption.** At this level, in addition to level 1, the frames are encrypted. All the above-mentioned measures are now included.

Introduced earlier, the IEEE 802.15.6 standard covers the following physical layers: UWB, NB, and HBC [20]. The NB PHY covers the ISM bands in the 400's MHz, 800's MHz, 900's MHz, and 2400's MHz. The channel bandwidth varies from 300 kHz to 1 MHz. The highest achievable data rate is 971.4 kbit/s in the 2400's MHz band.

The UWB PHY is divided into two band groups: low- and high-band. The former includes three channels from 3.494 GHz to 4.493 GHz while the latter contains 8 channels from 6.489 GHz to 9.984 GHz. All channels are 499 MHz wide. Each band has a mandatory channel that must be included in a compliant device. The available data rates for the UWB PHY span from 202 kbit/s with an FM modulation and up to 15.6 Mbit/s with a differentially coherent modulation. The mandatory channels are locked on 0.4875 Mbit/s.

The third PHY is HBC. It specifies the implementation of Electric Field Communication (EFC). The frequency of operation is centered in 21 MHz. The data rate is predefined and ranges from 164 kbit/s to 1.31 Mbit/s. The data are spread in the frequency domain using frequency selective spread codes before transmission. The transmitted frame contains all the required information (in the header), for the receiver to decode the message. Given the low frequency of operation, and to avoid any interference with vital bio-signal, the transmit spectral mask is asymmetric and sharper for the lower part of the spectrum. A representation is given in figure 4.6.
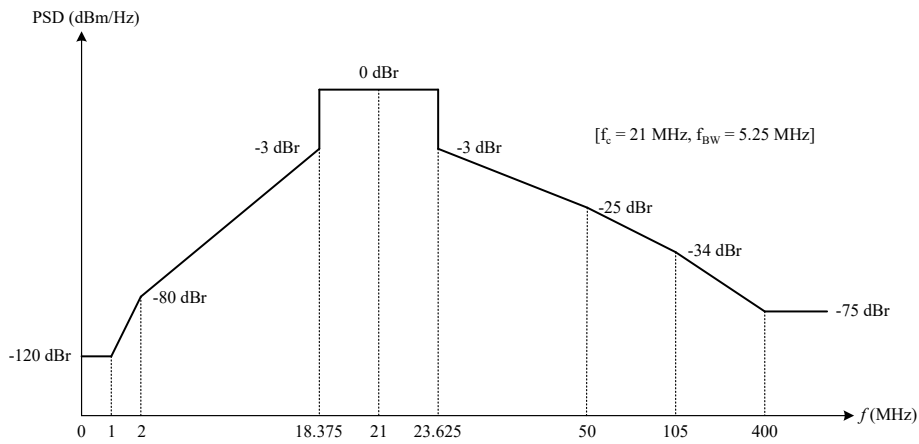
Figure 4.6: HBC spectral density mask, both according to the IEEE 802.15.6 standard. Taken from [20].

The IEEE standards introduced above cover Personal and Body Area Network. They offer multiple PHYs (UWB, NB, HBC) and MACs (TDMA, CSMA, bounded or not) mainly applicable to star network topologies. Those standards are not applicable as-is to the Human Intranet due to the network requirements such as its data rate and hybrid topology. The physical layer characterized earlier does not fit any of the standardized band in terms of frequency of operation

and bandwidth. It is worth noting that the lower UWB band (250-750 MHz) from the IEEE 802.15.4 standard encompasses the frequency band characterized in chapter 3. However, it is much wider, loosing the advantages of the surface wave dominance on the lower part of the spectrum. Nevertheless, many of their underlying concepts will be reused, extended, or customized: TDMA and beacon-based superframes for instance.

Table 4.2: IEEE 802.15.4 & IEEE 802.15.6 comparison

Specifications	IEEE 802.15.4 [53]	IEEE 802.15.6 [20]
Network Topology	Star Peer-to-peer	Star Two-hop extended star
MAC	Un-slotted CSMA Slotted CSMA + Beacons[1]	CSMA TDMA TDMA & CSMA
Network Master/hub	[1]Network master required	Only 1 hub
Mode of operation	Guaranteed time slot possible	Beacon mode w/ superframe Non-beacon mode w/ superframe Non-beacon mode w/o superframe
Supported PHY	Narrow Band (NB) Ultra Wide Band (UWB)	Narrow Band (NB) Ultra Wide Band (UWB) Human Body Communication (HBC)
NB PHY Specifications	868 / 915 / 2400 MHz 20 - 250 kbit/s	433 / 868 / 915 / 2400 MHz 75.9 - 971.4 kbit/s
UWB PHY Specifications	250-750 MHz / 3.1-5 GHz / 6-10.6 GHz 500 MHz bandwidth 0.11-27.2 Mbit/s	3.5-4.5 GHz / 6.5-9.9 GHz 500 MHz bandwidth 0.2-15.6 Mbit/s
HBC PHY Specifications	N/A	21 MHz 0.16-1.3 Mbit/s
Security level	N/A	0: Unsecured 1: Authentication w/o encryption 2: Authentication w/ encryption

4.2.2 Wake-up Receiver and Duty Cycle Approach

The previous section dealt with different communication protocols and their specificities. The standards propose different options to set up communication between nodes. Under all circumstances, the Rx node must be listening while the Tx nodes are transmitting the message. Extra listening duration in comparison with the transmit window is a waste of power. A very common and widely spread architecture to optimize the power consumption consists of implementing a Wake-up Receiver (WRx) within the Rx node [88]. Its principle and range of interest are studied in this section.

An Rx chain must meet some requirements which can be application- or standard-specific such as the sensitivity or selectivity for example. Consequently, optimizing the radio power consumption is limited. The Wake-up receiver principle lies in spreading the channel sensing and payload receiving functionalities in two dedicated blocks. The former is executed by the WRx. Its role is to sense the communication channel, sniffing for a specific message (i.e. a wake-up beacon), to wake-up the main radio. Despite the similarities with a classic Rx architecture, the WRx is meant to be lower power, only capable of receiving a short wake-up beacon with simple modulation, usually OOK [88]. The main radio is then in charge of the message reception which data rate, modulation, and input power can be different from the wake-up beacon.

Multiple modes of operation exist: Always-ON (AO-WRx) and Duty-Cycled (DuCy-WRx)

[89, 90]. The former proposes a simpler approach. The WRx is always running and sniffing for a wake-up beacon. Energy is saved as long as the WRx power consumption is lower than the main radio. This approach can be optimized from a consumption standpoint by duty-cycling the WRx. The idea is to limit the amount of energy consumed listening when unnecessary. Duty cycling a WRx can be implemented either synchronously or asynchronously. The synchronized duty cycling requires a network-shared timer, capable of periodically waking up the WRx. The objective is to open a periodic window, capable of triggering a communication upon request. On the other hand, the asynchronous approach, each WRx within the network autonomously wakes-up and operates as usual. No common clock is shared. An illustration of the different modes is proposed in figure 4.7.
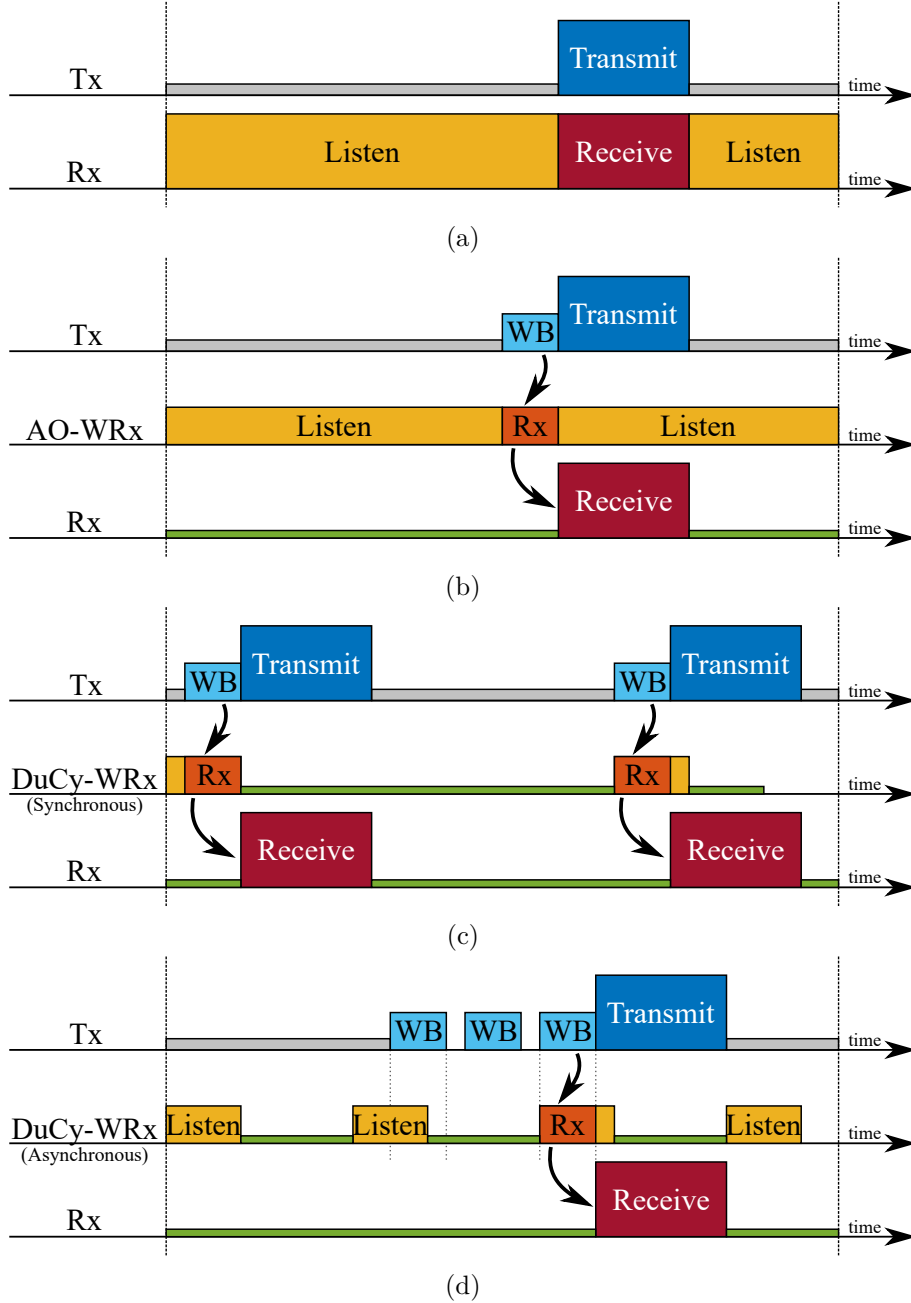
Figure 4.7: Communication principle (a) without Wrx, (b) with an AO-WRx, (c) with a synchronous DuCy-WRx and (d) with an asynchronous DuCy-WRx.

Always-ON WRx have the advantage of being capable of catching the wake-up beacon with no additional latency, detection condition, and miss-detection aside. The energy consumption can be higher than a duty-cycled counterpart. The latter saves power by waking up periodically,

to the cost of an additional timer. The embedded timer specifications need to be carefully defined to perform synchronous wake-up for all nodes within the network. If a node gets desynchronized, the overall system is inefficient as the considered node constantly misses all transmitted wake-up beacon. No clear rule can be applied regarding the WRx type required. The implementation efficiency is application-specific, an inappropriate architecture can reveal very inefficient or even worse in terms of power consumption and additional latency.

The Duty-Cycled approach presented in [89] is mathematically modeled and deeply analyzed in [90]. In the latter study, the authors included the WRx design characteristics such as the main radio and WRx power consumption (active and sleep mode), sleep time, wake-up beacon length, and their influence on the system behavior. Those parameters were used to compute system optimizations targeting energy savings for a simple network with light traffic conditions. A symmetric single-hop communication is considered here. The study also includes probabilities of misdetection and false-positive, impacting directly the power consumption and latency as a re-transmission is required.

The authors take a regular RX radio as a reference scenario to compare their optimized Ducy-WRx (see figure 4.7(c)) as well as AO-WRx (see figure 4.7(b)). The first take away from this study is a matter of relative power consumption between the WRx and the associated radio. The greater is their power consumption difference the more efficient becomes the WRx (both, Always On and Duty-Cycled) architecture. The duty cycle ratio is the key parameter for an optimized DuCy-WRx configuration. The approach is given seeking for the optimal sleep time, directly linked to the duty cycle ratio.

The optimal sleep time depends on multiple system parameters, such as the size of the network, the inter-packet arrival duration, and the header length among others. It increases with network size, longer wake-up beacon (WB) transmission time but decreases with traffic and packet length. In other words, a longer sleep duration compensates for energy-hungry configuration to a certain point where the sleep duration becomes the source of an excessive number of re-transmission wasting even more energy.

Under the same situation (with identical hardware running), the Ducy-WRx approach offers a great advantage in terms of power consumption as it trades off energy against larger latency. The optimal sleep time becomes bounded as soon as a maximal system latency is required, limiting the energy savings.

Two additional system specifications are also derived from this study. First, a DuCy-WRx optimal listening window lasts for the equivalent of two WB, one inter-WB duration, and an acknowledgment message. This result is important as the DuCy-WRx power consumption tightly depends on the listening duration. The second deals with the WB itself. Longer preamble and node address improve the decoding errors observed for shorter headers. However, beyond the optimal length, it increases the WB duration and the overall system power consumption as presented above.

Wake-up receivers and DuCy-WRx offer an energy-efficient synchronization solution. It can achieve major energy saving in comparison to AO-WRx and regular Rx architectures. Simulation results from [90] a 64% and 96% power consumption improvement respectively for a given scenario. DuCy-WRx show limitations when the average inter-packet duration decreases (i.e. increasing traffic), with the network size, or when a maximal latency is required. Those parameters directly impact the overall efficiency and require fine-tuning. Given the targeted applications and their versatility, they do not represent the typical use-case and the DuCy-WRx lack of flexibility is problematic. Despite their advantages, WRx are difficult to implement as-is for the Human Intranet.

4.2.3 Wrap-up

Multiple communication protocols and synchronization solutions were presented. They bring great communication mechanisms to the table but their implementation for the human intranet employing C-BCC seems difficult. The frequency of operation as well as the bandwidth differs from the standard. The data rate requirement is much higher than the listed options. In terms of synchronization, the Human Intranet constraints are too tight to efficiently deploy WRx as is. However, if the concepts on which rely all those solutions can be customized and adapted to our application, most of the existing ideas could then be reused.

4.3 Heartbeat-based Synchronization and Communication Protocol

Positioned as a platform augmenting human capabilities, including life support applications, the Human Intranet must operate faultlessly. It relies on a robust architecture, capable of mitigating different network topologies [19] enabling high throughput and low latency [91, 92] while being power efficient. The existing IEEE standards introduced earlier are good in terms of communication reliability and security but have blocking limitations in its implementation: 1- or 2-hop network topology and heavy synchronization requirements limit its flexibility and significantly impacting its efficiency. This section introduces the basis for a novel MAC protocol, benefiting from the heartbeat as a synchronization signal. Highlighting promising results in [93], the heartbeat-based synchronization theory is presented in combination with a puncture-based communication. The required hardware is also presented.

A significant part of this section dealing with the heartbeat synchronized communication was published in [94]: "Heartbeat-Based Synchronization Scheme for the Human Intranet: Modeling and Analysis," in *2020 IEEE International Symposium on Circuit and System.* This work has also been presented at the IEEE ISCAS 2020 conference. A deriving MAC protocol has been proposed and published in [95]: "Energy Efficient Heartbeat-Based MAC Protocol for WBAN Employing Body Coupled Communication," in *IEEE Access, vol. 8, 2020, Special Edition on Body Area Networks.*

4.3.1 Synchronization principle

The heartbeat-based synchronization requires all nodes to detect the heartbeat and use it as a time reference. A "superframe" is defined as the elapsed time between two consecutive heartbeats. This approach is similar to the beacon mode from the IEEE 802.15.6 standard except that no node is required to broadcast the synchronization beacon. Within the superframe, subframes can be defined and scheduled following a TDMA-like (Time Division Multiple Access) structure. A high level block diagram is presented in figure 4.8. Specific and periodic actions can be scheduled at the beginning of each superframe. It offers a similar capability to the Guaranteed Time Slot from the IEEE 802.15.4 standard or the scheduled access (in a Manage Access Phase) in the IEEE 802.15.6 standard studied earlier.
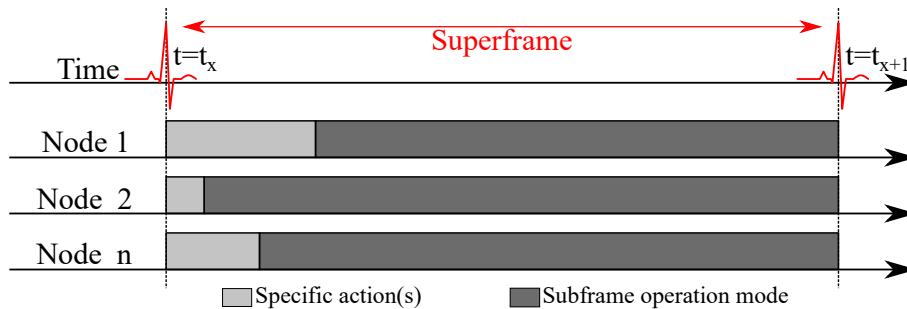
Figure 4.8: Heartbeat synchronization ans superframe principle

Bio-signal synchronization brings several advantages as the coordination signal (i.e. the heartbeat) is not generated but sensed by the system. The synchronization is operated without communication bandwidth allocation, ensuring constant channel availability. Given the short and periodic communication pattern (i.e. superframe occurrence), heartbeat synchronization offers robustness against nodes malfunction, random disconnections, and network expansion (or reduction). A node can resume normal operation as early as it is synchronized which is possible almost instantaneously. From a healthcare and wellness standpoint, the heartbeat is the health condition and physical activity image. Specific actions (see figure 4.8) are performed more often at no extra cost for the network. Ultimately, encryption keys can be derived from the shared signal as presented in [96]. This topic was not studied and is not covered in this manuscript.

This principle can be extended following the "lighthouse" concept. A node capable of sensing the heartbeat could act as a broadcasting point within the network, transmitting a synchronization beacon wirelessly. It offers several possibilities: (i) including nodes without heartbeat sensing capability, (ii) managing the synchronization beacon frequency of occurrence: more or less frequent, and (iii), ensuring the proposed MAC protocol compatibility with several communication technologies.

4.3.2 Deployment principle

To enable a heartbeat-based synchronization, it requires that all nodes embed a heartbeat detection capability. It can be performed using multiple techniques [97]:

- **Electrical sensing**. It requires at least two electrodes in which potential difference is amplified and filtered. Ultra-Low Power (ULP) implementations were demonstrated [98]. This solution is interesting as it can operate with low supply voltage and the processing chain can be included in a SoC. However, it faces three majors difficulties: (i) not suitable for limbs extremities [21, 99], (ii) body movements adding extra noise and impedance change from the skin-electrode interface [98] and, (iii) low frequency pass-band filtering ability 5-15 Hz [100].

- **Vibration sensing**. As the heart beats and the blood flows, they generate mechanical pressure on the veins and arteries resulting in a small yet detectable motion. Accelerometers/MEMS (Micro-Electro-Mechanical Systems) can sense the motion facing extra noise due to body movements as well and could necessitate high operating voltage [101, 102]. It can theoretically be positioned almost anywhere on the body as long as body motion does not outweigh the blood displacement amplitude in the frequency band of interest.

- **Light sensing**. This technique indirectly senses the heartbeat by analyzing the blood-reflected light emitted by the source LEDs [103, 104]. This alternative is robust to body motion and electromagnetic noise and can be located on limb extremities as long as a vein is close enough to the skin layer. However, it shows limitations under bright conditions and is usually more power-consuming than the above-mentioned solution.

Distant heartbeat acquisition has also been demonstrated in [105]. This technique is not applicable as the detection is performed off-body.

Even if electrical sensing is not achievable all around the body, it is the selected solution for the rest of our analysis. Several reasons led us to this choice: (i) This technique is well known and described in the medical literature; (ii) the state of the art of such method presents ULP implementations; and (iii) the same electrodes can be employed for heartbeat sensing and Capacitive Body Coupled Communication, optimizing the form factor and the integration for a future product.

On a macroscopic scale, the principle is not complex and many heartbeat detection options are available. However, on microscopic analysis, many details must be taken into account to establish the minimum system requirements for this synchronization scheme to be attractive.

Synchronization relies on optimizing the timing alignment between nodes. Regarding our synchronization scheme, two main misalignment families can be listed. The first source of inaccuracy is the heartbeat detection "absolute date". We define the absolute date as the virtual time reference when any event occurs. It can be considered as the ideal, but the unrealistic case, where all actions are triggered on time without inaccuracy. The electrical signal sensed by each node is caused by a chemical reaction leading to myocardium contractions [106]. This signal propagates from the heart within the human body. In the literature, only [107] studied the ECG propagation speed. The authors came to the conclusion that the minimal traveling speed was greater than: $v_{HB_{min}} \geq 250$m/s. This minimum value is taken as the propagation speed to perform worst-case scenario analysis. Given the Human Body dimensions, the propagation cannot be neglected. We describe it as the "heartbeat skew", which corresponds to the difference in terms of time of arrival among all the concerned nodes. The second source of timing misalignment comes from the TDMA-like communication within a superframe. To operate properly, a local time source is required for all nodes, dividing the superframe into sub-frames. This local and embedded clock slightly varies from node to node. Consequently, adding extra uncertainty regarding the local time. Those timing errors are thoroughly covered within chapter 5.

The above description highlights the need for a local clock. One can wonder what is the added value of the heartbeat detection feature and why the local clock is not enough on its own for performing the synchronization task. Long-term clock accuracy can be problematic especially without the use of a crystal (bulky) while offering ultra low power implementation with a minimum absolute accuracy. The heartbeat synchronization drastically reduces the maximal duration between two reset operations. A regular heart rate (HR) falls in the range from HR_{min}=36 beats per minute (bpm) to HR_{max}=210 bpm [108, 109]. In other words, the superframe duration T is greater than $T_{min} \geq 0.29$ s and lower than $T_{max} \leq 1.67$ s. This unique property relaxes the constraints on the timing solution. The behavioral analysis is conducted within the next section.

4.3.3 Human Intranet Communication protocol

Presented in Figure 4.3, the network architecture is a mesh of star. A leaf is connected to a single hub, also called "parent hub". A hub, however, can be connected to multiple leaves and hubs simultaneously.

There are many options in developing a wireless network that spans the human body, each of which has its advantages and challenges. Often heterogeneous approaches combining multiple communication modalities are required. Considering the needs formulated in this chapter, one option that addresses both the upper and lower performance requirements is the use of Human-Body Coupled Communication in the 400 to 500 MHz frequency band, characterized within chapter 3. While this choice is not essential, it helps in providing a unifying perspective.

In [67] and in chapter 3, we established that a C-BCC solution operating in the 400-500 MHz frequency band (with a center frequency of 450 MHz) offers some distinct advantages. At these frequencies, surface waves are the dominant propagation mechanism, making the channel less sensitive to changes in the environment and to coupling with external references. Its form factor is smaller and more convenient for the end-user than antenna-based RF technologies. Its attenuation per unit distance is also lower [68], at the cost of higher insertion loss. Its specifications are recalled below.

From measurements [67], it was established that a bandwidth of at least 100 MHz is available with flat attenuation. The derived channel loss model is presented in (4.1), and its parameters (as measured at 450 MHz) are enumerated in Table 4.3.

$$L = \begin{cases} L_0 & d = d_0 \\ L_0 + \alpha_0(d - d_0) & d_0 < d < d_1 \\ L_1 + \alpha_1(d - d_1) & d_1 < d \end{cases} \tag{4.1}$$

Table 4.3: Channel loss model parameters

Frequency (MHz)	L_0 (dB)	α_0 (dB/cm)	L_1 (dB)	α_1 (dB/cm)	σ
450	-47	-0.95	-55	-0.37	6.5

σ is the standard deviation of the measurement compared to the theoretical fit, explained by the non-homogeneity of the medium (i.e. the human body). L_0 expresses the loss for the shortest distance recorded at $d_0 = 5$ cm. L_1 represents the loss at $d_1 = 15$ cm, transition distance between the quasi-static (QS) and surface wave regimes.

To take full advantage of such bandwidth, pulse-based communication is envisioned. Given the pulse's shape and duration, the occupied spectrum in the frequency domain can be controlled as presented figure 4.9. It brings several advantages:

- A wide data rate span can be achieved with the same hardware as it just depends on the pulse period of occurrence.

- A wide-band approach helps for body shape mitigation. Figure 3.15 showed that the optimal frequency of operation depends on the limb size; wide coverage allows a consistent average behavior over the human body.

- It allows an aggressive transmitter duty-cycling leading to energy-efficient data transmission.
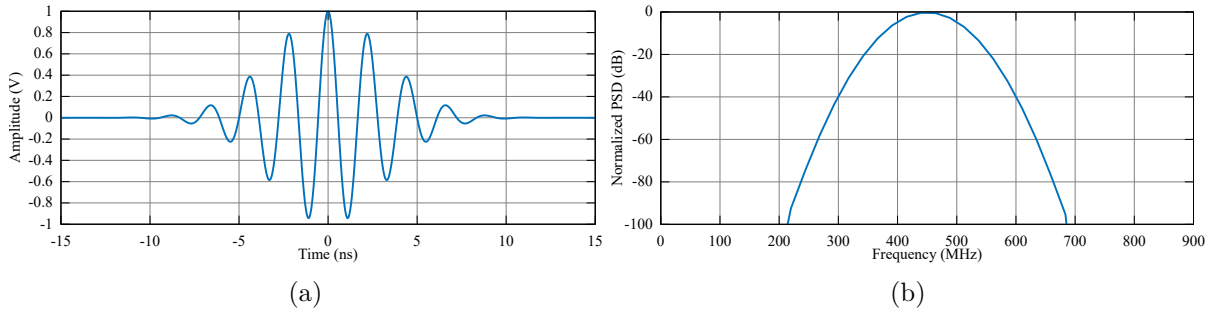
Figure 4.9: Pulse-based communication, (a) time domain, (b) frequency domain

Based on the analysis from [110], for a windowed-cosine pulse model, a 20 ns Gaussian pulse in the time domain corresponds to a 150 MHz-bandwidth signal at -10 dBc in the frequency domain. With a simple modulation such as OOK or BPSK transmitting 20 ns pulses, the maximum theoretically achievable data rate is 50 Mbit/s.

Given the architecture presented in figure. 4.3, the type and amount of data exchanged from Table 4.1, the channel characterization results from [67] and the pulse-based communication centered on 450 MHz, the hub-to-hub communication data rate is set to 50 Mbit/s with BPSK modulation scheme. The leaf-to-hub link is however set to 100 kbit/s with the OOK modulation scheme. It offers a good trade-off between the transmission time of a given message and the achievable transmitter energy efficiency, relaxing the constraints on the leaf timing.

The receiver sensitivity S is calculated in (4.2) as a function of the integrated thermal noise N_{th} (in dBm) over the bandwidth of consideration BW (see (4.4)) [111].

$$S = N_{th} + NF + SNR_{req} \qquad (4.2)$$

where NF is the receiver noise figure and SNR_{req} is the required signal-to-noise ratio expressed in (4.3) as a function of the desired data rate DR.

$$SNR_{req} = \frac{E_b}{N_0} + 10 \cdot log_{10}\left(\frac{DR}{BW}\right) \quad (4.3)$$

$$N_{th} = 10 \cdot log_{10}(K \cdot T \cdot 10^3) + 10 \cdot log_{10}(BW) \quad (4.4)$$

For a usual noise figure of $NF = 6$ dB, a bandwidth of $BW = 150$ MHz, a ratio $E_b/N_0 = 14$ dB and a data rate of $DR = 100$ kbit/s and $DR = 50$ Mbit/s, the sensitivity becomes respectively:

$$S_{100\text{kbit/s}} = -104\text{dBm} \ \& \ S_{50\text{Mbit/s}} = -77\text{dBm}$$

In terms of geometry, the leaf-hub distance is limited to 15 cm while the inter-hub separation ranges from 15 to 50 cm, about an adult arm length. This configuration allows a large coverage of a human body and limits inter-cluster interference.

In terms of path loss, it is calculated from equation 4.1, that the leaf-hub signal attenuation is not greater than 55 dB. Given a receiver sensitivity of -104 dBm and a 3 dB margin, the minimal output power the leaf transmitter should radiate is about -46 dBm. Applying the same calculation, the hub transmitter output power should be around -10 dBm.

The data traffic flows through the network as follows: the main traffic takes place between hubs in a bi-directional manner with the highest data rate achievable. It is the default situation. On the other hand, the amount of data generated by a leaf is limited as presented in Table 4.1.

The C-BCC single-channel network in combination with a heartbeat-synchronized communication, implements a "puncturing" capability, prioritizing the main traffic while enabling scheduled leaf-to-hub communication, ensuring frequent but non-obtrusive data upload. The puncturing approach requires sub-frames scheduling. A sub-frame is defined by its start time, the time elapsed from the beginning of the superframe, and its duration. The principle is illustrated with a simple 2-node example following a 200 ms periodic communication in figure 4.10. The global behavior is very similar to TDMA (Time Division Multiple Access).
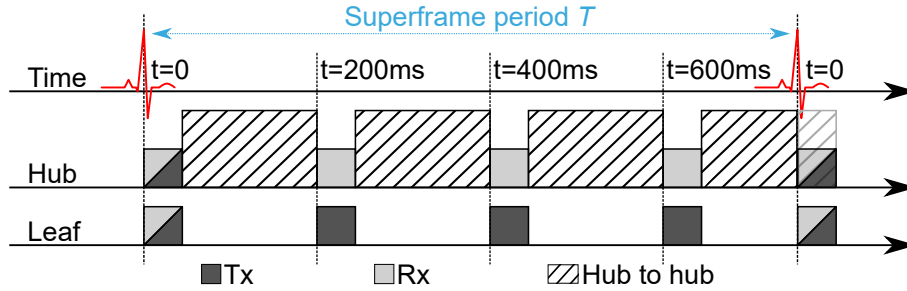
Figure 4.10: Superframe example with periodic puncturing and listening window.

Figure 4.10 presents a bi-directional communication as its first sub-frame. It enables the possibility for a hub to send data to its leaves, such as sending updates for instance. This particular communication slot is scheduled at the very beginning of each superframe. Only an individual leaf can be addressed at a time within each local star network. This constraint is not problematic as a leaf update is a rare event. Ultimately, a cluster-wide mass update could be envisioned with a local broadcasting address.

The above-introduced communication scheme relies on the networks' heartbeat synchronization ability. Figure 4.11 presents a leaf's heartbeat based synchronization block diagram. The signal reception and transmission are included as Rx and Tx respectively while the leaf purpose (data acquisition...) is modeled as "system". The synchronization chain is depicted with two blocks. The heartbeat detector (HB detector) translates the ECG signal into a digital output, resetting the timer. In parallel, the receiver is switched ON for a short period allowing the leaf

update. The second block is a timer. It generates periodic ticks, triggering a transmission based on its counter auto-reload value. This scheme is repeated continuously until the next heartbeat.
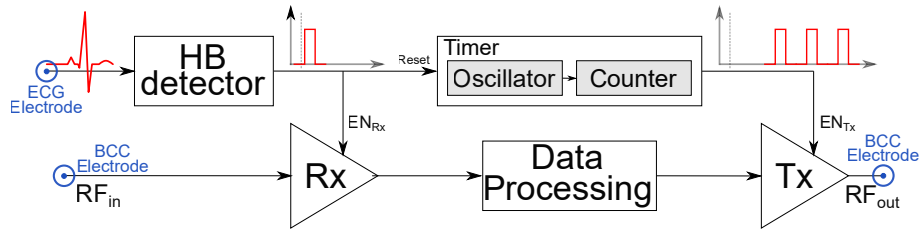
Figure 4.11: Synchronization functional block diagram.

The challenge of such a communication protocol lies in the nodes' synchronization efficiency. The adequate coordination scheme optimizes three major parameters: the channel availability, the system power consumption, and its latency. The channel availability, expressed as a percentage, is defined as the ratio between the hub-to-hub communication duration over the total considered communication period. Since the objective is to optimize the entire system, the power consumption calculation takes into account all nodes included in communication (i.e. at least a transmitter and a receiver). The latency represents the time elapsed from data availability to its transmission. Those metrics are studied in detail in chapter 5. All three are tightly dependent on the "timing accuracy". The timing accuracy represents a node's ability to keep its local time as close as possible from a virtual absolute time of reference.

4.3.4 Wrap-up

A heartbeat-based synchronization concept was introduced as well as its deployment principle. Multiple heartbeat-sensing methods were proposed enabling heartbeat detection almost all over the human body. A dedicated communication protocol was proposed, combining heartbeat-based synchronization, punctured communication, and C-BCC and its channel specifications as a physical layer. The limits of such a synchronization scheme and its consequences on the communication and the system were highlighted.

4.4 Conclusion

This chapter studied the different possibilities to build a network suitable for The Human Intranet. The network architecture is of first importance as its nature could limit the system performance. A detailed analysis was conducted on different network topologies applicable. However, a network topology cannot be chosen ignoring the system constraints in terms of reliability, robustness, geometry, energy consumption, applications, physical layer, MAC protocol, and use cases.

The Human Intranet skeleton was established following a mesh of star topology (or hybrid). Such an architecture resulted from the combination of the different network topologies capabilities and the study from [19]. The latter deals with the non-trivial trade-off between reliability (packet delivery ratio) and energy consumption (network lifetime). Moreover, we investigated the different types of node which could be involved in the network. A cleared trend appeared regarding their respective data generation rate based on their refresh period and resolution. Two distinct categories emerged: (i) nodes with a below-hundreds of kbit/s data generation rate, and (ii) those generating multiple thousands and above kbit/s. The former could be implemented following a simple and ULP topology while the latter would require consequent access to energy and computing capabilities. Such a partitioning shows high compatibility with the mesh of stars selected above. The smaller and simpler nodes are then called leaves, connected to a unique and more complex counterpart named hub. The leaves-hub connections operate as a star network while the hub-to-hub network is meshed or partially meshed.

Following the architecture selection, existing standardized communication protocols were studied. The goal was to understand their different mode of operation, root principle, and conclude regarding their compatibility with our application and network structure. Both IEEE standards: 802.15.4 [53] and 806.15.6 [20] are not suitable as-is, as none cover a mesh of star architecture or the frequency of interest highlighted in chapter 3.

A Human Intranet-dedicated MAC protocol was required. Many channel access methods [112] (e.g. TDMA) and synchronization implementations (e.g. RTC) already exist. However, exploiting the heartbeat as a synchronization signal has rarely been considered, the only prior related work is [93]. It offers unique advantages such as being available from the subject at no extra energy and transmission cost and adapting automatically to the wearer's physical activity. The synchronization principle was detailed. It operates based on superframes (similar to IEEE Standards) defined as the duration between two consecutive heartbeats. Various heartbeat sensing modalities were introduced: electric, light, sound, and pressure. This synchronization scheme is (almost) applicable all over the human body given the detection methods listed. Our investigation did not cover the compatibility and complexity in interfacing devices carrying different heartbeat detection technologies. The electric signal processing is the only one capable of reusing C-BCC electrodes to interface the human body.

Ultimately a puncture-based heartbeat-synchronized communication protocol was proposed including C-BCC specificities as the physical layer. Its limits were identified and their impact on the communication was established. The following chapter will introduce those non-idealities with a mathematical model, along with simulation results, bringing in-depth analysis.

5. System Level Simulation

Chapter 4 reviewed different network architectures, communication protocols, and synchronization mechanisms. Our analysis led to a mesh of star topology, heartbeat synchronized network, featuring a puncture-based communication. The current chapter aims at mathematically modeling the heartbeat-based synchronization, including the blocks non-idealities. The performance is evaluated following specific metrics and system specifications are derived. Ultimately, a comparison with a duty-cycled wake-up receiver is conducted.

5.1 System Architecture Model and Non-Idealities

This section presents the heartbeat synchronization with a mathematical model for each of the following blocks: the heartbeat detector (HBd), the timer, and the transmitter/receiver. The approach follows two steps: first, the expressions are given in the "ideal" configuration. It is assumed that all blocks are perfect. The second step consists of developing the former model into a realistic mathematical description. The building blocks non-idealities are considered.

5.1.1 Heartbeat Detector

The Heartbeat detector is the first block of our synchronization chain. Its purpose was introduced in chapter 4: it translates the ECG signal into a digital output.

According to [21], the ECG is defined as follows: "The electrocardiogram (ECG) is the recording of the electrical activity generated during and after activation of the various parts of the heart. It is detected by electrodes attached to the skin". The ECG pictured in figure 5.1 is a fairly complex signal, however, the heartbeat detector only focuses on identifying the R-wave from the QRS complex. The R-wave is the signal portion of the greatest amplitude and is also referred to as "the peak" within this manuscript.
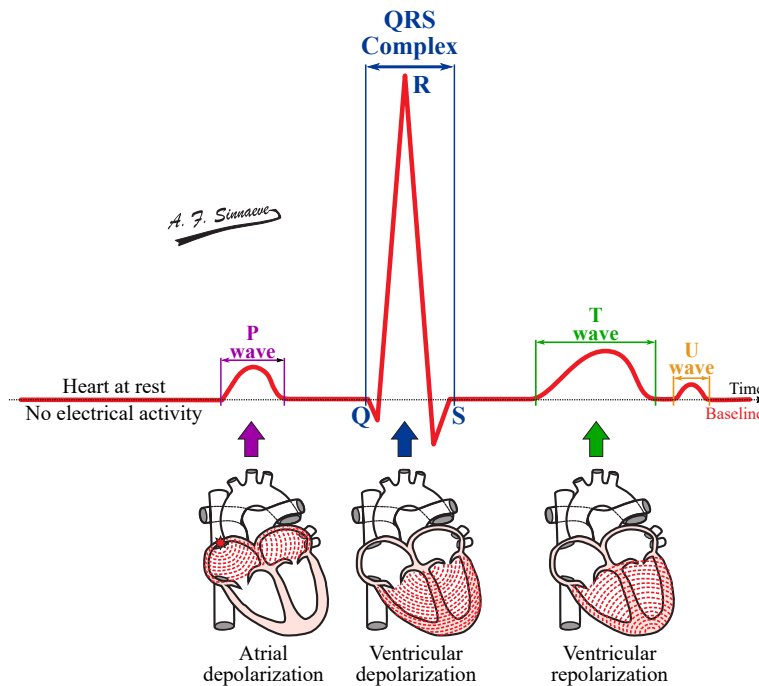
Figure 5.1: ECG representation and the QRS complex - Picture taken from [21].

The heartbeat detector generates a system-level synchronization signal from the heartbeat. No ECG extraction capability is granted to this block simplifying its structure and the embedded features required.

To date, one of the best implementations in terms of robustness, power consumption is proposed in [98]. The authors implemented a 58 nW heartbeat detector, featuring a 66 dB Common Mode Rejection Ratio (CMRR) (required as they perform a 2-lead acquisition), combined with a motion tolerant timing extraction capability. They demonstrated the ability to detect regular and weak ECG signals: as low as 30 µV. Ultimately, the R-wave maximum amplitude timing is accurately estimated, freeing our analysis from modeling the detection time inaccuracy on a given node.

From a synchronization standpoint, the main source of inaccuracy related to heartbeat detection is the signal propagation delay. From the state of the art, only [107] studied the ECG propagation speed within the human body. The authors did not precisely measure the signal propagation speed v_{HB} but rather a lower bound: $v_{HB} \geq 250$ m/s. Although it's not an accurate velocity, it is a guaranteed lower bound, required to perform the worst-case analysis.

Given the minimum propagation speed highlighted above, the "heartbeat skew", Δt_{HB}, is defined as the absolute detection time difference between two nodes intending to communicate. For instance, two nodes A and B, at a distance d_A (d_B respectively) from the heart would detect the beat at t_{d_A} (t_{d_B} respectively). The nodes' interdistance d is: $d = |d_A - d_B|$. The heartbeat skew is only a function of the nodes' inter distance d, and is then calculated in equation (5.1).

$$\Delta t_{HB} \leq \frac{|d_A - d_B|}{v_{HB}} = \frac{d}{v_{HB}} \tag{5.1}$$

The heartbeat skew is sketched in figure 5.2 on a time and distance scale.
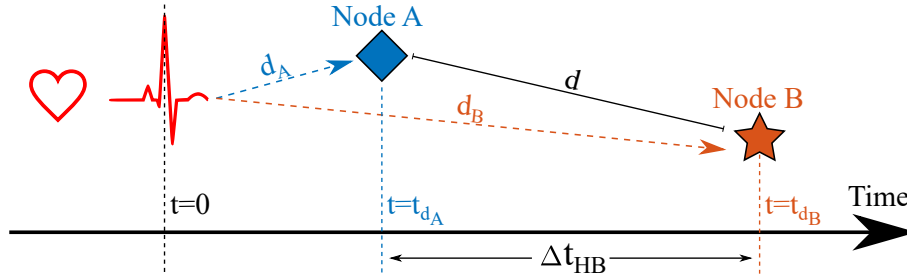
Figure 5.2: Heart beat skew representation

In terms of power consumption, the HBd is modeled in our analysis with a static power consumption P_{HB_d}. Its average power consumption and its corresponding contribution to the considered system total power consumption is proportional to its running time. The hardware specifications for efficient detection are out of the scope of our research, although it has been extensively studied in the literature.

The heartbeat period of occurrence or heart rate (HR), fluctuates over time, following the physical activity for instance. We define as a local variability, two consecutive inter-heartbeat duration time difference. It is limited and can be modeled following a normal distribution with a standard deviation of $\sigma = 30$ ms [113]. A global variability is established and refers to the HR upper and lower bounds. It is assumed to fall in range from $HR_{min} = 40$ beats per minute (bpm) to $HR_{max} = 200$ bpm [108, 109]. It corresponds to a superframe (inter-heartbeat) duration T of: $T_{200bpm} = 300$ ms and $T_{40bpm} = 1500$ ms. The average heart rate for an adult in good health ranges from 60 bpm to 100 bpm [114]. For specific analysis, an average HR of 80 bpm will be considered in our analysis unless otherwise specified.

Given the global and local variability introduced above, a duty cycle scheme can be implemented to optimize the HBd power consumption. It can be statically or dynamically executed.

The former would turn the block off for a fixed duration of 250 ms (static) while the latter would adapt given the last recorded superframe duration and the standard deviation (dynamic) from [113].

The heartbeat detector model specifications are summarized in Table 5.1 below:

Table 5.1: Heartbeat detector model specifications

Function	Power Consumption	HB Skew	HR Range	Duty Cycle
ECG peak detection only	P_{HB_d}	$\Delta t_{HB} \leq d/250\ s$	40 - 200 bpm	Capable Static/Dynamic

5.1.2 Timer

The timer block is in charge of dividing the superframe into sub-frames. More specifically, it triggers periodic leaf-to-hub communication. To fulfill its purpose, the timer is composed of two sub-blocks: an oscillator and a counter as depicted in figure 5.3. The former generates a periodic pattern identified and counted by the latter. The preset counter auto-reload value allows action triggering after a predefined number of detected cycles. In terms of power consumption, the timer is modeled in our analysis with a static power consumption P_{timer}.
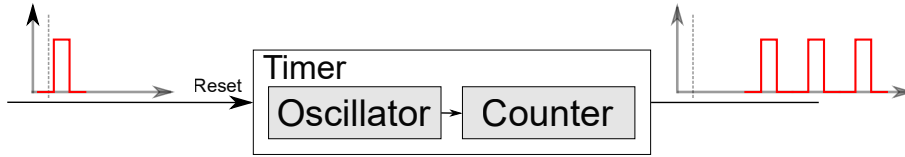
Figure 5.3: Timer block diagram

The heartbeat synchronization triggers a regular timer reset, at the beginning of each superframe upon the heartbeat detection. Such a feature limits the inaccuracy accumulation over the running time. The period of reference now becomes the superframe duration. For consistency and reliability purposes, only the worst-case scenario is considered when $HR_{min} = 40$ bpm and $T_{40bpm} = 1500$ ms.

The timer suffers three different sources of inaccuracy: (i) the oscillator frequency offset and counter granularity, (ii) the oscillator frequency drift, and (iii) the oscillator accumulated random jitter. Sometimes modeled together as those phenomena occur simultaneously, in this case, all three are detailed within individual sections. It facilitates modeling and lowers its complexity.

5.1.2.1 Oscillator Frequency Offset and Counter Granularity

An oscillator is defined (among others) by its nominal frequency of operation f_0. It is the designed running frequency at which it (precisely) oscillates in the ideal case. However, several causes such as design technique, manufacturing process, and temperature of operation lead to an effective oscillation frequency slightly differing from f_0.

We want to provide a system-level mathematical model consistent with the studied function. A compensation feature is proposed to improve the timing accuracy, modifying the modeled function as follows. The oscillator is directly connected to the counter incremental input. A custom, one-time calibration can be performed by adjusting the counter auto-reload value. It counterbalances the actual frequency of oscillation f_{osc} with the total number of cycles, bringing the inaccuracy down to the counter granularity. The oscillator/counter combination translates the frequency offset into a time uncertainty $\Delta t_{counter}$, which eventually equals a single oscillator period (see equation 5.2):

$$\Delta t_{counter} = \frac{1}{f_{osc}} \tag{5.2}$$

The oscillator offset frequency, as well as its combination with a calibrated counter, is deterministic. While the inaccuracy sources are diverse, their subsequent variations are predictable and their amplitude is bounded.

5.1.2.2 Oscillator Frequency Drift

The oscillator offset frequency introduced above is considered constant for a given device. Its variation over time is modeled here as the oscillator frequency drift. It expresses the slow oscillation frequency variation over time as represented in figure 5.4(a). In the frequency domain, according to Leeson's model, the low-frequency noise is converted into a $1/f^3$ phase noise around the carrier [115]. It is depicted in figure 5.4(b), as the close-in phase noise.
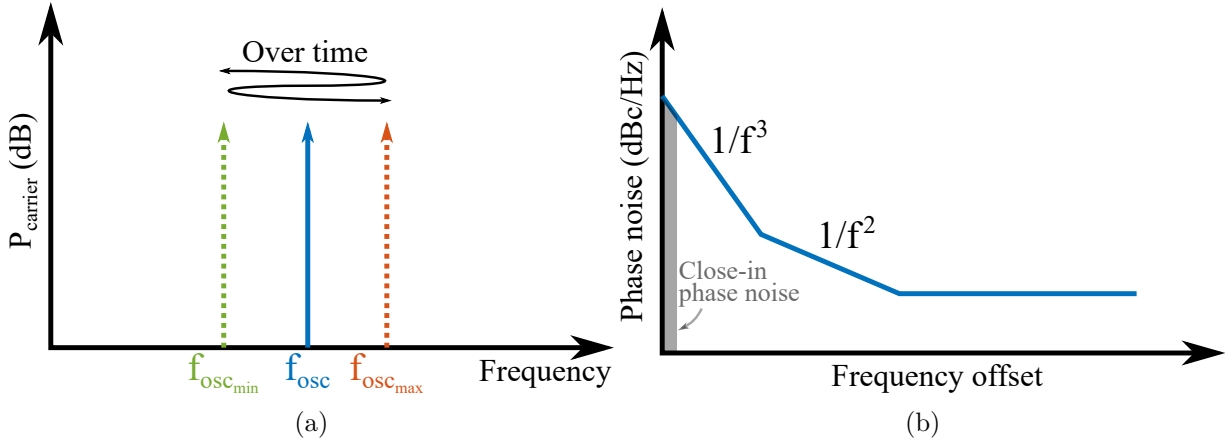
Figure 5.4: (a) Frequency variation in the frequency domain. (b) Drift identification in Leeson's phase noise model representation

Similarly to the oscillator frequency offset, its drift is deterministic and bounded. Its maximum frequency deviation is calculated as a ratio in ppm, $Drift_{osc}$, of the theoretical frequency of oscillation. It corresponds to the uncertainty in terms of the number of cycles over a million. The resulting inaccuracy, Δt_{drift}, is given in (5.3).

$$\Delta t_{drift} = Drift_{osc} \cdot \frac{1}{f_{osc}} \tag{5.3}$$

The worst scenario occurs when the oscillator drifts uniformly over time to reach its upper (or lower) bound at the end of the considered superframe (i.e. cycle duration). The consequent timing inaccuracy increases over time (in terms of absolute value).

5.1.2.3 Oscillator Accumulated Random Jitter

The oscillator random jitter is probabilistic and by definition unpredictable [115]. It impairs every clock cycle duration as the clock edge fluctuates in comparison to theoretical time of occurrence. It is also often referred as a "cycle-to-cycle variation" as two consecutive cycles' edges are not identical.

The random jitter follows a Gaussian normal distribution $f_j(t)$ given in equation (5.4) [115]. Within the current analysis, the distribution's mean value μ is null ($\mu=0$) as the drift introduced earlier is considered as a distinct parameter.

$$f_j(t) = \frac{1}{\sigma \cdot \sqrt{2\pi}} \cdot e^{-\frac{(t-\mu)^2}{2\sigma^2}} \tag{5.4}$$

where σ is the variance RMS value.

Modeling and considering the cycle-to-cycle jitter is appropriate in data transmission and decoding as it could significantly impact the BER. An eye diagram is the plot of choice in such a situation.

Given our application (a timer) the accumulated random jitter is a more relevant metric as the timer goes off only once the counter reaches its auto-reload value. Therefore, the fluctuations in the oscillator's period are not pertinent while its accumulation is.

It is worth noting that the distribution's mean value is null. Combined with the phenomena randomness, the accumulated random jitter tends to equal its average (null in our case).

All clock cycles are independent as the edges fluctuations from one cycle does not provide any information regarding the following. Consequently, the accumulated random jitter also follows a Gaussian normal distribution [116, 117]. Its variance σ_N only depends on the number of oscillations N as stated in equation (5.5) and the variance RMS value from equation (5.4).

$$
\begin{aligned}
\sigma_N^2 &= \sigma_1^2 + \sigma_2^2 + ... + \sigma_{p-1}^2 + \sigma_p^2 \\
&= N \cdot \sigma^2
\end{aligned}
\tag{5.5}
$$

The final accumulated random jitter Gaussian distribution $f_{j_N}(t)$ is given in equation (5.6).

$$
\begin{aligned}
f_{j_N}(t) &= \frac{1}{\sigma_N \cdot \sqrt{2\pi}} e^{-\frac{(t-\mu)^2}{2\sigma_N^2}} \\
&= \frac{1}{\sigma \cdot \sqrt{N} \cdot \sqrt{2\pi}} \cdot e^{-\frac{t^2}{2N\sigma^2}}
\end{aligned}
\tag{5.6}
$$

The above theory has been numerically verified with Matlab. The random jitter tends to reach its mean value as the number of cycles (i.e. oscillation periods) increases. The calculations were performed for a 50 ms duration for multiple oscillator frequencies, which changes the total number of cycles N. For all selected frequencies (from $10\,\text{kHz}$ to $1\,\text{MHz}$), 10'000 iterations of a normal distribution with $\mu = 0$ mean and a variance $\sigma = 1$ are generated. For each iteration, the average cycle duration (i.e. oscillation period duration) is calculated. For each frequency, the cycle duration variance over the 10'000 iterations is computed and plotted in figure 5.5 (blue solid line). Along the computed accumulated random jitter variance per cycle, figure 5.5 also plots the theoretically predicted value of $\sigma_N = \sigma/\sqrt{N}$ (dashed orange with $\sigma = 1$). We observe that both curves are superimposed, confirming the theoretical expression from equation (5.6).

The Matlab code is available in appendix A.

Comparing both Gaussian distribution expressions (5.4) and (5.6), we observe t the number of cycles impact's on the accumulated random jitter distribution. Its probability density function (PDF) is more spread out: larger variance (see equation (5.6)) and lower amplitude.

Since the accumulated random jitter is probabilistic, the only way to appropriately take it into account is to consider the resulting inaccuracy as a function of the global variance σ_N. The window size as a function of the variance and its corresponding coverage probability are presented in table 5.2.

Table 5.2: Variance and coverage probability for a Gaussian normal distribution

Window size	σ_N	$2\sigma_N$	$3\sigma_N$	$4\sigma_N$	$5\sigma_N$
Coverage (%)	68.269	95.450	99.730	99.994	99.999
Not covered (ppm)	317'311	45'500	2'700	63	<1
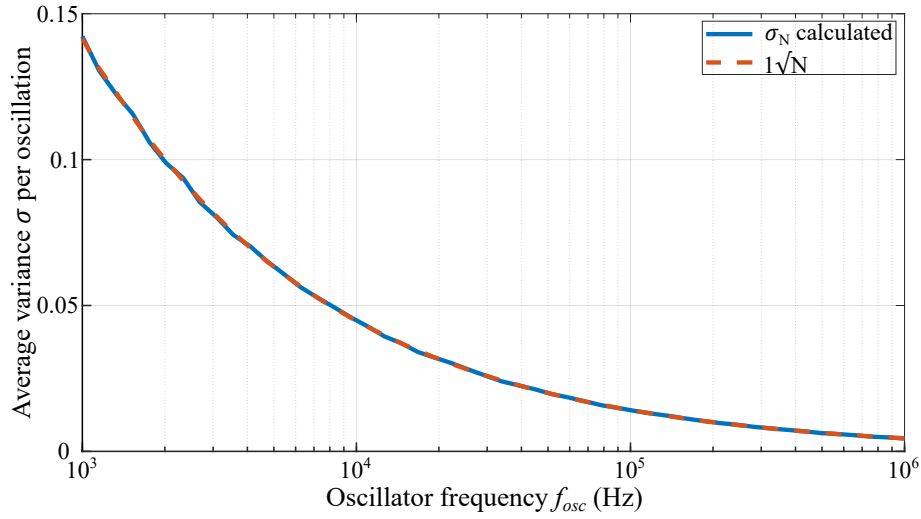
Figure 5.5: Accumulated random jitter as a function of frequency for a fix duration of 50 ms

Given the results from table 5.2, the considered inaccuracy in regards to the oscillator accumulated random jitter $\Delta t_{jitter}(t)$ is taken equal to four times the global variance. Such window size brings the probability of not covered events as low as 0.0063% (or 63 ppm).

The resulting inaccuracy is expressed in equation (5.7). As the variance is a function of the number of oscillations and their individual variance, it also expresses as such. It helps in defining the design specifications as the random jitter is usually given for a single cycle.

$$
\begin{aligned}
\Delta t_{jitter}(t) &= 4 \cdot \sigma_N \\
&= 4 \cdot \sqrt{N} \cdot \sigma \\
&= 4 \cdot \sqrt{f_{osc} \cdot t} \cdot \sigma
\end{aligned}
\tag{5.7}
$$

The timer model specifications are summarized in Table 5.3 below:

Table 5.3: Timer model specifications

Function	Power Consumption	Offset frequency timing error	Frequency drift timing error	Accumulated random jitter timing error
Trigger periodic communication	P_{timer}	$\Delta t_{counter} = \frac{1}{f_{osc}}$	$\Delta t_{drift} = Drift_{osc} \cdot \frac{1}{f_{osc}}$	$\Delta t_{jitter}(t) = 4 \cdot \sqrt{f_{osc} \cdot t} \cdot \sigma$

5.1.3 Transmitter and Receiver

Introduced in chapter 4 with the wake-up receiver principle, exchanging synchronization data could be mandatory. Also, to properly evaluate the overall system power consumption, it makes sense to take into account the payload data exchange for a given situation. Following such an approach permits to highlight the contribution and overhead of each block involved, especially those dedicated to synchronization.

The transmitter and receiver models are basic as their evaluation is not covered in this manuscript. However, from a system standpoint and for a future design implementation, their power consumption, P_{Tx} and P_{Rx}, are calculated as a function of their energy efficiency $\mathcal{E}_{Tx}$ and $\mathcal{E}_{Rx}$ (in J/bit). A common communication data rate D_R is assumed. The transmitter power consumption is given in equation (5.8). The latter is only running while transmitting data.

$$P_{Tx} = \mathcal{E}_{Tx} \cdot D_R \tag{5.8}$$

Regarding the receiver, its power consumption is calculated following the same equation (with its own parameters). Introduced earlier, the receiver may operate during listening windows without receiving data. During those listening phases, its power consumption is considered equal to a regular data reception, as the receiver is fully operational. Consequently, it is calculated as a function of its running time.

The transmitter and receiver models specifications are summarized in Table 5.4 below:

Table 5.4: Transmitter and receiver model specifications

Function	Data rate	Energy efficiency	Power Consumption
Data transmission	D_R	$\mathcal{E}_{Tx}$	$P_{Tx} = \mathcal{E}_{Tx} \cdot D_R$
Data reception	D_R	$\mathcal{E}_{Rx}$	$P_{Rx} = \mathcal{E}_{Rx} \cdot D_R$

5.1.4 Synchronization Margin

The above section introduces the system non-idealities regarding both synchronization blocks: the Heartbeat Detector and Timer. All four sources: the heartbeat skew, the oscillator frequency offset, the oscillator frequency drift, and oscillator random jitter directly impact the individual node timing accuracy (With respect to, for example, a locked timing reference).

Those different phenomena are taking place at node scale. In a two-node configuration (a hub and a leaf), the inaccuracy observed on the leaf is independent of the timing error occurring on the hub. For robustness purposes, a worst-case approach is followed. The worst-case scenario considers all timing errors accumulated and set to their maximal value. It means that the node local time is different from the absolute true time, within the range detailed earlier. In addition, these accumulated errors could either make a node "faster" or "slower" than predicted. This approach aims to replicate a realistic scenario from a timing standpoint.

Our system is synchronized on the heartbeat but each node within the network embeds its own time reference. The latter is to a certain extent inaccurate (as detailed above). A workaround to compensate for the nodes' relative time-difference consists of setting up a "synchronization margin" within the communication schedule. The idea is for the receiver node, to open the listening window earlier than ideally necessary. Such an approach frees the transmitter to validate the destination node's status as it is guaranteed by nature.

Figure 5.6 shows a simple 2-node example where the leaf's local timing reference runs slightly faster than expected while the hub's goes slower. Both were meant to communicate a $t = t_1$ from the last detected heartbeat. Since both nodes are independent, the hub has no information regarding its time difference with the leaf.
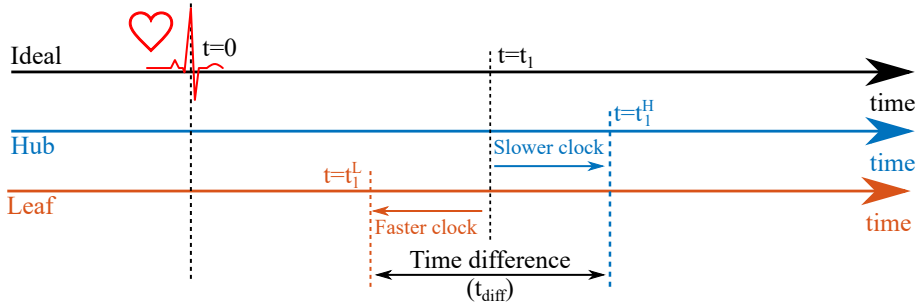
Figure 5.6: Time difference example in a 2-node configuration, due to the embedded time reference inaccuracy.

Considering the most common communication pattern where a leaf uploads data to its parent hub, a significant part of the message could be missed if the time difference t_{diff}, highlighted in figure 5.6, is not compensated for. In this example, both nodes are meant to communicate at $t = t_1$. However, the leaf local clock runs faster, leading to a data transmission starting at $t = t_1^L$. On the other hand, the hub is late and only starts listening at $t = t_1^H$. Consequently, the data transmitted during $t_{diff} = t_1^H - t_1^L$ are lost. The synchronization margin concept is based on triggering the listening window earlier than planned making sure the receiver is in listening mode when the data transmission starts. In the specific example from figure 5.6, the synchronization margin M_{tot} should be at greater than: $M_{tot} \geq t_{diff}$.

Optimizing the synchronization margin duration optimizes the whole system. Taken too long, energy is wasted and the average throughput is lowered. Taken too short, it increases the probability to miss data and indirectly increases the power consumption as a second transmission is necessary. In the following, the time difference t_{diff} is precisely estimated in a worst-case scenario (as introduced earlier) and the synchronization margin calculated to ensure the receiver readiness under all circumstances.

We defined the leaf inaccuracy, Δt_{Leaf}, as its maximum time difference with the absolute true time. From the example given in figure 5.6, it is expressed as: $\Delta t_{Leaf} = t_1 - t_1^L$. Similarly, the hub inaccuracy is defined as Δt_{Hub}, and is equal to: $\Delta t_{Hub} = t_1^H - t_1$ (see figure 5.6).

The worst-case approach ensures a maximal value in regards to the synchronization margin, thus covering all other cases. Also, the data transmission is triggered as soon as the leaf's local timer goes off. Consequently, we consider:

- The leaf is located closer to the heart. It detects the heartbeat first.

- The leaf local timing block runs faster, triggering the communication ahead of schedule.

- The Hub is located further away from the heart. It suffers the heartbeat skew.

- The Hub local timing block runs slower, triggering a listening window behind schedule (without compensation).

Based on the configuration stated above and the different inaccuracy sources introduced earlier we can write:

$$\Delta t_{Leaf} = \Delta t_{counter} + \Delta t_{drift} + \Delta t_{jitter} \tag{5.9}$$

and

$$\Delta t_{Hub} = \Delta t_{counter} + \Delta t_{drift} + \Delta t_{jitter} + \Delta t_{HB} \tag{5.10}$$

Finally, from (5.9) and (5.10),the synchronization margin and the time difference (t_{diff}) become:

$$\begin{aligned} M_{tot} \geq t_{diff} &= \Delta t_{Leaf} + \Delta t_{Hub} \\ &= 2 \cdot (\Delta t_{counter} + \Delta t_{drift} + \Delta t_{jitter}) + \Delta t_{HB} \end{aligned} \tag{5.11}$$

Equation (5.11) presents the maximum time difference between two nodes, in the worst possible case where all sources of timing variations are accumulated with opposite consequences on both nodes. This time difference is the minimum synchronization margin (M_{tot}) to apply to the communication schedule to guarantee the receiver operation.

The above analysis considered a pair of node where the leaf was located the closest from the heart, and thus sensing the synchronization signal first. However, from a deployment standpoint, the relative nodes' location is not guaranteed. A hub can be positioned the closest from the heart

instead. Similarly, a hub can be ahead of schedule compared to its leaves. Such configuration, depicted in figure 5.7, does not undergo any synchronization issue but suffers from an extended listening window. In this second scenario, the hub is ahead of schedule while the leaf is late. Their relative time difference t_{diff} is represented in figure 5.7. However, the hub can't predict such a delay and applies the synchronization margin M_{tot} calculated in equation (5.11). In the specific case (i.e. presented figure 5.7), the hub opens a listening window at $t = t_{listen}$ and starts receiving data at $t = t_1^L$. The elapsed time is called the "wait time", t_w, and is defined in equation (5.12).

Figure 5.7: Synchronization margin applied on hub ahead of schedule, extending the wait time.

$$
\begin{aligned}
t_w &= t_1^L - t_{listen} \\
&= M_{tot} + t_{diff}
\end{aligned}
\tag{5.12}
$$

This combination of extreme conditions (depicted in figure 5.7) is rare but possible. Our later analysis and simulations (presented within section 5.3) are considering a maximum wait time $t_w = M_{tot} + t_{diff}$ where the maximum relative time difference is: $t_{diff} = M_{tot}$. Consequently, the results obtained will represent the least favorable yet minimum achievable performance.

5.1.5 Wrap-up

Within this section, the different blocks fulfilling the synchronization function based on the heartbeat were described. The heartbeat detector and timer blocks operation mode have been detailed to highlight their non-idealities. An equation-based mathematical model was proposed for all of them. Ultimately, from a behavior standpoint, those non-idealities led to the introduction of a synchronization margin. The latter is mandatory given the heartbeat-based synchronization principle to ensure both communicating nodes' timing alignment. This mandatory guard interval was also modeled to compensate for the timing error from the non-idealities identified earlier. Those models will be driving the upcoming system quantitative analysis.

5.2 Metrics

The synchronization scheme efficiency is evaluated by three metrics:

- The latency

- The system power consumption

- The channel availability

All three are detailed below. Their mathematical models are established under two circumstances: the "ideal" and "realistic" case. The former does not take into account any loss. The reception time is taken equal to transmission duration. The ideal model does not suffer time

or energy waste. On the other hand, the realistic case includes the system non-idealities in terms of timing, as presented in section 5.1. It models the non-idealities by introducing the synchronization margin in the system equations.

The metrics and their associated mathematical equations are given below for a local star network connecting n leaves to a single hub. For consistency and comparison purposes, all the time- and superframe-dependent equations provided within this section are normalized to a superframe duration T.

5.2.1 Latency and additional synchronization time

The latency represents the time elapsed between two data upload. Within the heartbeat synchronization scheme, the latency is a system parameter. It is set to a coherent value given the application, the type of sensor, and the current activity. Section 4.3 (from chapter 4), presents a bi-directional communication capability for leaves. The latter gives the hubs the ability to update a leaf's latency setting dynamically. In the example given in figure 4.10 the latency setting is set to 200 ms.

The "additional synchronization time" is defined as the time elapsed between the transmitter readiness and the receiver availability. Such an additional time is required for asynchronous nodes to be fully settled for communication.

Heartbeat-coordinated nodes are aligned on an out-of-system clock and thus synchronized. Besides, the synchronization margin (introduced earlier) implemented within the communication schedule, enforces that no additional synchronization time is required. Such a synchronization mechanism is deterministic by nature.

5.2.2 System Power Consumption

We call "system" here all the nodes involved in the data exchange at cluster-level. At least one hub and one leaf are required to form a cluster. The system power consumption calculation takes into account each individual node and provide system-level numbers.

Fully symmetric nodes are considered, whether they operate in Tx or Rx mode. Such assumption is possible as we focus on the synchronization scheme efficiency and inter-cluster communication (i.e. only leaf-hub). In addition the hubs behave following the leaves' capabilities in terms of data rate. Ultimately, the required synchronization and timing functions are mandatory on all nodes. The generic node architecture is presented in figure 4.11.

The power breakdown for all nodes in the ideal case is the following:

- Heartbeat detector: P_{HB_d}

- Timer: P_{timer}

- Radio:

  - Transmit mode: P_{Tx}

  - Receive mode: P_{Rx}

The radio power consumption P_{Tx} (or P_{Rx}), depends on its energy efficiency $\mathcal{E}_{Tx}$ (or $\mathcal{E}_{Rx}$), the data transmission rate D_R as presented in equation (5.8). Given the periodic communication scheme, the radios (Tx and Rx) are not operating continuously. Following such a principle, the data are stored in the leaf's memory and transmitted all at once. The quantity of data exchanged is modeled by a "Data Generation Rate", D_{gen}. It corresponds to the node's average data production over time, as a constant flow.

The periodic upload relies on the latency setting, Lat, (introduced above) and the corresponding number of full puncturing events per superframe $N_p = \left\lfloor \frac{T}{Lat} \right\rfloor$. D_{gen} and Lat drive the

transmitter ON-time T_{Tx}, calculated in (5.13) for a single leaf.

$$T_{Tx} = \left\lfloor \frac{T}{Lat} \right\rfloor \cdot \frac{D_{gen} \cdot Lat}{D_R} \tag{5.13}$$

In the ideal scenario, for n leaves uploading their data toward a hub, the corresponding power consumption, P, is given in equation (5.14).

$$P_{ideal} = (n+1)(P_{HB_d} + P_{timer}) + (P_{Tx} + P_{Rx}) \cdot \frac{1}{T} \sum_{i=1}^{n} T_{Tx} \tag{5.14}$$

The realistic configuration corresponds to the ideal scenario degraded by the wait time t_w required to ensure the node timing alignment. In chapter 4, the periodic and punctured-based communication scheme was introduced. As a synchronization margin is required for each data exchange, the total wait time, T_w, depends on the number of puncturing events per superframe, N_p, as presented in equation (5.15) (for a single leaf).

$$T_w = N_p \cdot t_w \tag{5.15}$$

Consequently, the realistic system power consumption is given in equation (5.16).

$$P_{real} = P_{ideal} + P_{Rx} \cdot \frac{1}{T} \sum_{i=1}^{n} T_{w_i} \tag{5.16}$$

The objective is to minimize the system power consumption and especially the overhead due to the node synchronization. For readability purposes, the system power consumption calculated as P_{real} in (5.16) will be noted P_{sys}.

5.2.3 Channel Availability

The channel availability (CA), expressed as a percentage, is defined as the ratio between the hub-to-hub communication duration, $t_{hub-to-hub}$, over the superframe period, T, as calculated in equation (5.17).

$$CA = \frac{t_{hub-to-hub}}{T} \tag{5.17}$$

From a calculation standpoint, the channel availability's complement is the total transmission time, T_{Tx}, from the n leaves surrounding a hub. Over a superframe period, the channel availability in the ideal scenario is calculated in equation (5.18).

$$CA_{ideal} = 1 - \frac{1}{T} \sum_{i=1}^{n} T_{Tx_i} \tag{5.18}$$

Similarly, the realistic CA model suffers from the synchronization margin and is driven by equation (5.19).

$$CA_{real} = CA_{ideal} - \frac{1}{T} \sum_{i=1}^{n} T_{w_i} \tag{5.19}$$

The idea is to maximize the CA. However, by definition, a CA of a 100% is not relevant as it means that the studied hub does not communicate with its leaf.

5.2.4 Wrap-up

Three evaluation metrics were introduced in this section. They aim at qualitatively describe the communication between nodes within the framework of the Human Intranet. All three were expressed mathematically, integrating the different functional block models introduced earlier. A two-step approach was followed, increasing the level of complexity from an "ideal case" to a "realistic scenario". The latter taking into account the identified system non-idealities. Ultimately, all presented equations follow the worst scenario, leading to the worst, yet achievable, result with such a synchronization scheme.

5.3 Simulations and Comparison with Duty-Cycled Receivers

Our heartbeat-based synchronization scheme and the associated functional blocks were mathematically modeled above. This section presents the results from the equation driven analysis. It aims at evaluating the proposed synchronization scheme performance and permits a quantitative comparison with a common duty-cycled radio mechanism. All results are given in a realistic scenario.

A significant part of this section dealing with the heartbeat-based synchronized scheme was published in [94] ("Heartbeat-Based Synchronization Scheme for the Human Intranet: Modeling and Analysis," at the International Symposium on Circuit and System 2020) and presented at the ISCAS2020 conference.

5.3.1 Heartbeat-Based System Level Simulations

To perform such a quantitative analysis, assumptions are made regarding the hardware specifications. Those hypotheses rely on state-of-the-art implementations, although, conservative values are considered. The selected system parameters are listed in Table 5.5 (unless otherwise stated).

Table 5.5: System Parameters

Description	Symbol	Value	Unit
Oscillator jitter variance	σ	1	μs
Oscillator drift	$Drift_{osc}$	500	ppm
Heart beat detector power consumption [98]	P_{hbd}	100	nW
Timer power consumption [118]	P_{timer}	100	nW
Tx energy efficiency	$\mathcal{E}_{Tx}$	100	nJ/b
Rx energy efficiency	$\mathcal{E}_{Rx}$	100	nJ/b
Communication data rate	D_R	100	kb/s
Data generation rate (from leaf)	D_{gen}	1000	b/s
Leaf-Hub distance	d	15	cm
Latency (input parameter)	Lat	200	ms
Heart rate	HR	80	bpm

Detailed within the previous section, the proposed synchronization scheme's outcome depends on the wait time, t_w (see equation (5.12)), itself a function of the synchronization margin, M_{tot} (see equation (5.11)). The latter takes into account the system non-idealities, in particular the counter and the accumulated random jitter timing errors, $\Delta t_{counter}$ and Δt_{jitter} respectively. Both are tied to the oscillator unlocked frequency.

The first system parameter to define is the optimal oscillator's frequency. Figure 5.8 presents the contribution of all sources of inaccuracy as well as their accumulation. The results are given for a superframe duration of 750 ms, corresponding to an 80 bpm heart rate. Consequently, a

frequency of oscillation, $f_{osc} = 10$ kHz is selected to minimize the maximum time difference per puncturing event.
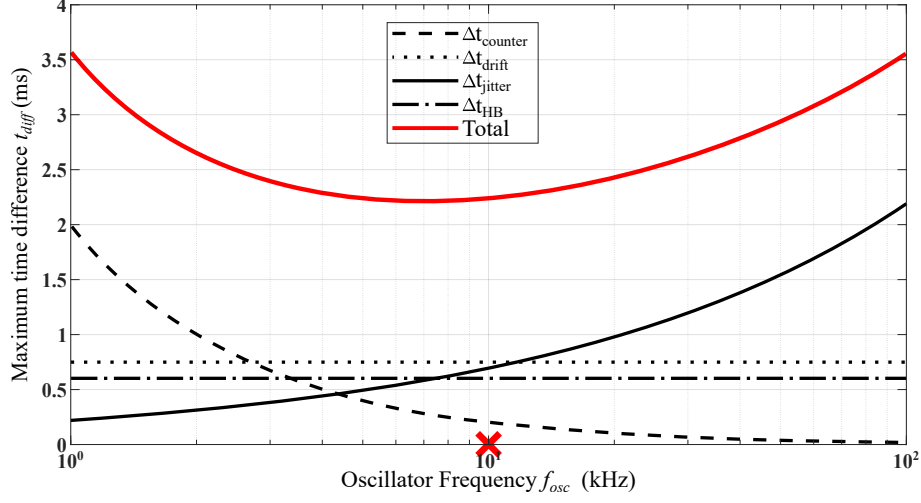
Figure 5.8: Maximum time difference, t_{diff}, as a function of the oscillator frequency.

The oscillator's frequency being set, the resulting timing error from its associated drift and accumulated random jitter, $\Delta t_{drift}(t)$, and $\Delta t_{jitter}(t)$ respectively, are functions of the superframe duration. Figure 5.9 highlights the the maximum wait time, t_w, (as defined in equation (5.12)) considered for each puncturing event, for multiple superframe durations (i.e. heart rate). The inaccuracy sources' individual contributions are specified by the color code.
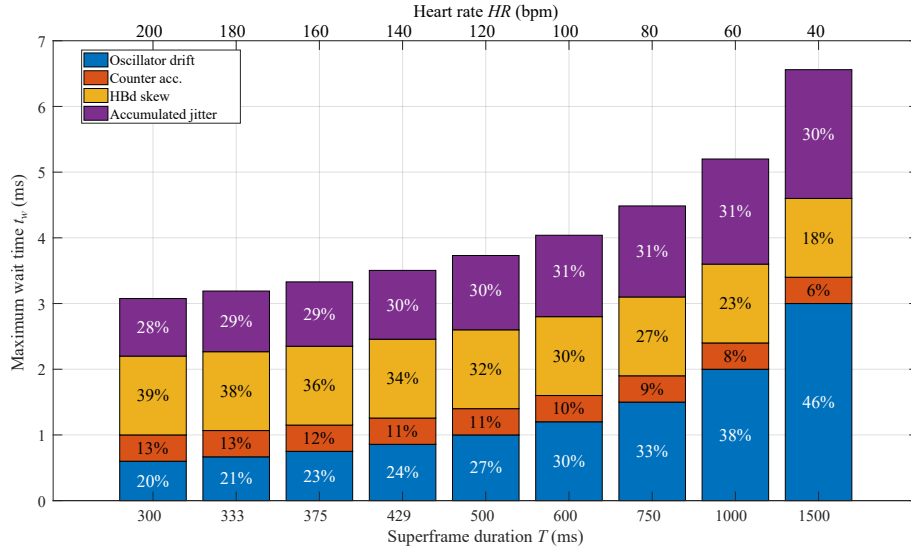
Figure 5.9: Maximum wait time t_w and associated inaccuracy sources' contribution.

From this plot, one can observe that the heartbeat skew is the major contributor for superframe durations below 600 ms (i.e. $HR \geq 100$ bpm). On the other hand, the frequency offset narrowed down to one period of oscillation by adjusting the counter auto-reload value, is the least contributor. The drift and accumulated random jitter show similar consequences on the wait time, due to the optimized oscillator frequency.

One of the three metrics introduced in section 5.2, was the latency. Given the heartbeat synchronization mechanism and the puncturing approach combination, the latency becomes a system parameter. In other words, it is a "user-defined" system input, not an uncontrolled outcome. Such latency management grants our system a deterministic behavior, suitable for time-critical applications.

To understand its impact on the system in terms of channel availability and power consumption, the latency parameter is swept from 50 ms to 300 ms by steps of 50 ms. A 50 ms latency setting corresponds to duration short enough for real-time [91, 92], and critical applications. On the other hand, 300 ms does not exceed the minimal superframe duration of 300 ms while the heart beats at 200 bpm.

Figure 5.10 presents the channel availability for a hub-leaf pair. Its mathematical expression was given in equation (5.19). The wait time was set to its maximal value of $t_{w_{max}} = 2 \cdot M_{tot}$. The results are plotted as a function of the superframe duration for multiple latency settings. For a given latency, the channel availability decreases with the superframe duration. This is directly due to the greater timing inaccuracy for longer superframe as depicted figure 5.9.

For a given superframe duration, the channel availability is inversely proportional to the transmissions' frequency of occurrence. A shorter latency setting increases the number of puncturing events per superframe, thus increasing the total wait time, T_w (accumulation of t_w), finally degrading the channel availability.
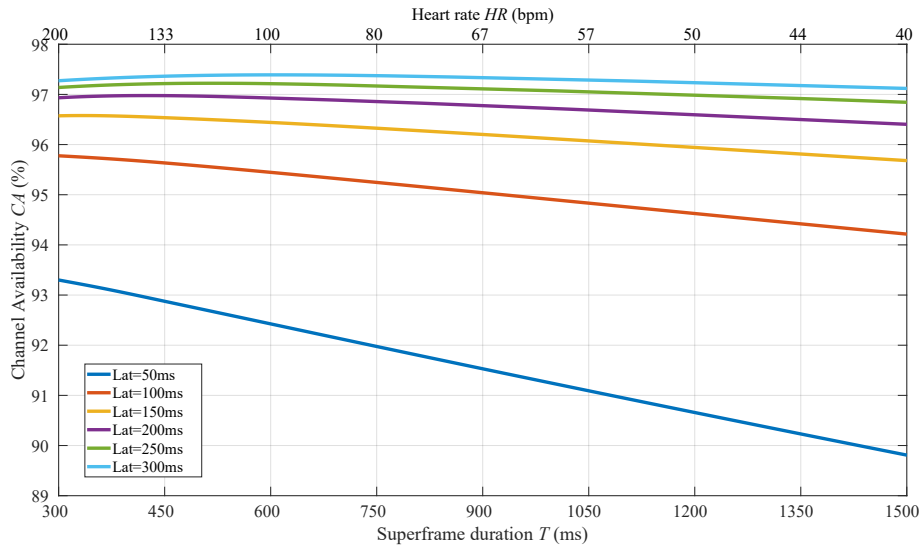
Figure 5.10: Channel availability for multiple latency settings.

Figure 5.11 presents the system power consumption, P_{sys}, for a set of two nodes: a hub and a leaf. The equation leading those results was presented in (5.16), $t_{w_{max}}$ considered.

The results are plotted as a function of the superframe duration for multiple latency parameters. For a given latency setting, the system power consumption increases with the duration of interest. The reason is simple, the wait time t_w per puncturing event increases with the superframe duration, as depicted in figure 5.9, increasing the system power consumption. It is noteworthy highlighting that doubling the superframe duration does not double system power consumption since t_w is not constant over time.

Alike the channel availability, for a fixed heart rate, the system power consumption is inversely proportional to the transmission frequency. In both cases, the root cause is the same: total wait time, T_w. A low latency provides a more responsive system against a (significant) system power consumption increase and channel availability degradation.
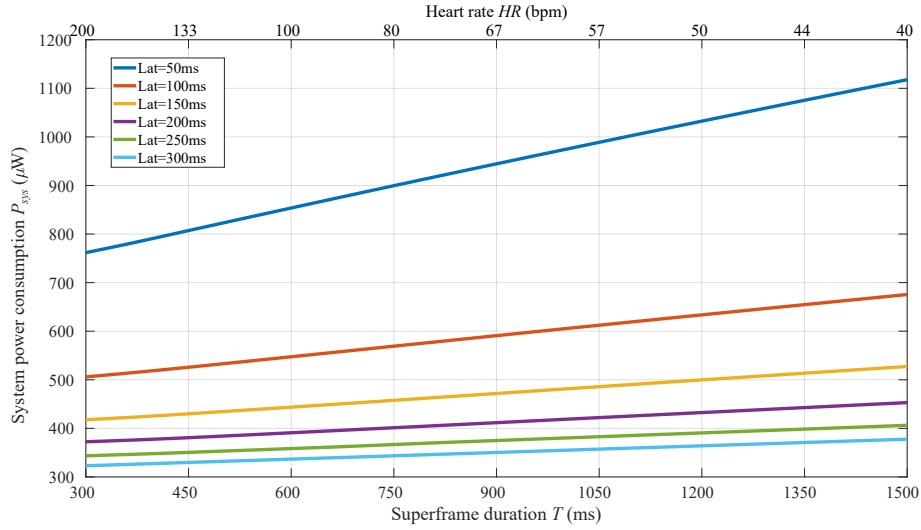
Figure 5.11: System power consumption for multiple latency settings.

The system power consumption breakdown is presented in figure 5.12 over latency for a heart rate of 80 bpm. It is split into two categories where the total wait time, T_w, corresponds to the receiver power consumption while running without receiving data, as defined in equation (5.15). It represents on it own between 41% and 78% of the total system power consumption. The total wait time is the major contributor while the heartbeat detector and timer blocks are negligible (see table 5.6). It is worth noting that the total system power consumption increases for a latency setting of 250 ms while the trend is to decrease with latency. This is since such a superframe duration (750 ms) perfectly equals 3 uploads events for a latency set to Lat=250 ms. It is a calculation artifact.
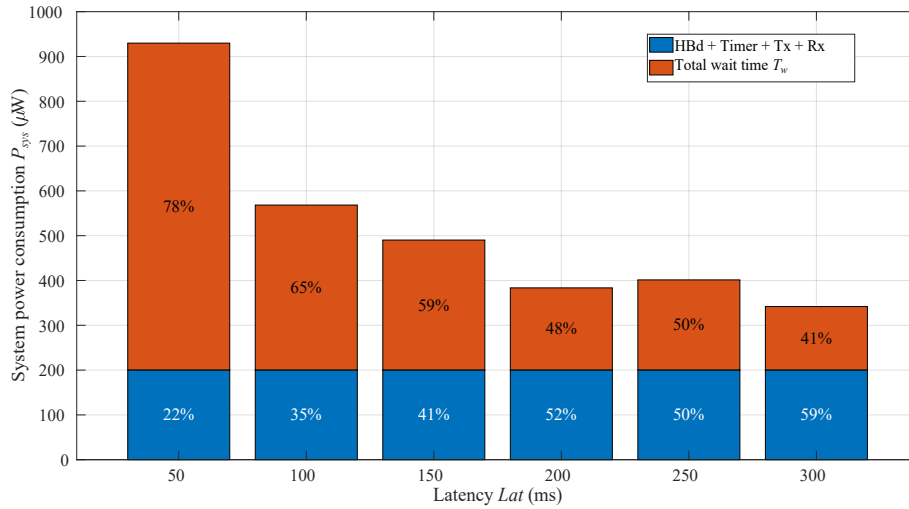
Figure 5.12: System power consumption breakdown.

Table 5.6: System power consumption breakdown numerical values

Latency	50 ms	100 ms	150 ms	200 ms	250 ms	300 ms
Heartbeat detector	0.02%	0.035%	0.04%	0.05%	0.05%	0.06%
Timer	0.02%	0.035%	0.04%	0.05%	0.05%	0.06%
Transmission	10.8%	17.6%	20.4%	26.1%	24.9%	29.3%
Reception	10.8%	17.6%	20.4%	26.1%	24.9%	29.3%
Total wait time T_w	78.5%	64.7%	59.1%	47.8%	50.1%	41.4%

Combining the above results with the inaccuracy sources' contribution from figure 5.9, one can notice that a calibration mechanism compensating for the heartbeat skew could improve the total wait time by 27%. An evolved calibration mechanism could also establish the position of each node relative to the heart. Such a feature would dispense the synchronization scheme from doubling the maximum time difference, t_w, offering an additional improvement of 50% in the system power consumption. For a latency of $Lat = 200$ ms and a heart rate of $HR = 80$ bpm, the system power consumption would decrease from $P = 383.5 \, \mu W$ down to $P_{cal} = 266.61 \, \mu W$, achieving a 30.5% global power saving.

We focused our analysis so far on the system. It took into account a hub/leaf pair. Figure 5.13 analyzes the power consumption from a leaf only. Given the communication scheme, a leaf's power consumption is only spread over three blocks: the heartbeat detector, the timer, and the transmitter. Figure 5.13 presents the transmitter's power consumption ratio over the leaf data generation rate D_{gen}. The latter represents the average amount of data to transmit from an embedded sensor for instance.
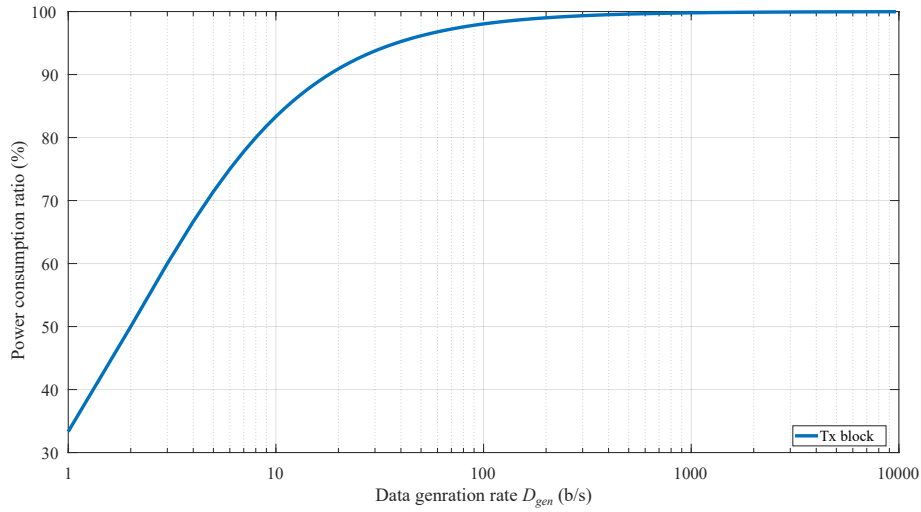
Figure 5.13: Leaf power consumption (HBd, timer and Tx only).

From this figure, it becomes clear that the synchronization blocks' power consumption (HBd and timer) is negligible compared to the transmitter power consumption. In fact, the latter represents 50% of the leaf's power consumption if it transmits an average of 2 bit/s. This ratio becomes greater than 80% for an average communication of 10 bit/s. Such results lead to the conclusion that it would be more relevant to improving the transmitter's energy efficiency than optimizing either of the synchronization blocks as it is by far, the most consuming block on a leaf.

5.3.2 Duty-Cycled Approach

A duty-cycled receiver is a common power saving solution. It consists of disabling a node's receiver and periodically turning it ON. Its principle is thoroughly detailed within section 4.2.2. The wake-up beacon duration, t_{WB}, is a function of the wake-up beacon length, WB, and the data rate (from table 5.5), $D_R : t_{WB} = WB/D_R$. For simplicity purposes, we considered the wake-up beacons only containing the transmitter and receiver nodes' addresses, 8 bits each [90]. The inter-wake-up beacon duration, $t_{I_{WB}}$, was derived from [90], equals to the switch time, t_{sw}, from sleep to transmit (Tx) mode and half a wake-up beacon duration (avoiding almost continuous wake-up beacon firing) as details in equation (5.20).

$$t_{I_{WB}} = t_{sw} + \frac{t_{WB}}{2} \tag{5.20}$$

The listening window duration, t_{list_DuCy}, is then defined in equation (5.21), as a function

of the above listed parameters.

$$t_{list_{DuCy}} = 2 \cdot t_{WB} + t_{I_{WB}} \tag{5.21}$$

In order to perform a fair comparison with the heartbeat-based synchronization scheme, no acknowledgment phase was considered since the probability of error were not models on both schemes. The corresponding probability error model is not yet available for our C-BCC for the frequency of operation of interest.

Additional system parameters, regarding the duty-cycled receiver, are listed in Table 5.7 (unless otherwise stated).

Table 5.7: System Parameters

Description	Symbol	Value	Unit
Wake-up beacon length	WB	16	b
Wake-up beacon duration	t_{WB}	160	µs
Switch time from sleep to Tx	t_{sw}	5	µs
Inter-wake-up beacon duration	$t_{I_{WB}}$	85	µs
Listening window duration (5.21)	$t_{list_{DuCy}}$	405	µs

The typical use-case introduced in figures 4.10 and 5.7 with a heartbeat-based synchronization is presented in figure 5.15 with a duty-cycled receiver. It details its principle and modeling parameters. For comparison purposes with the heartbeat synchronization scheme, only a leaf and a hub are involved. To mimic the HB-sync behavior, two phases are identified. Phase 1 is dedicated to hub-to-hub communication while phase 2 is reserved for leaf-to-hub uploads. It is assumed that the hub is triggering the data upload from the leaf by sending the wake-up beacon. Unlike the Heartbeat-based synchronization, the duty-cycled configuration requires an additional synchronization time, t_{sync}, as defined within section 5.2.
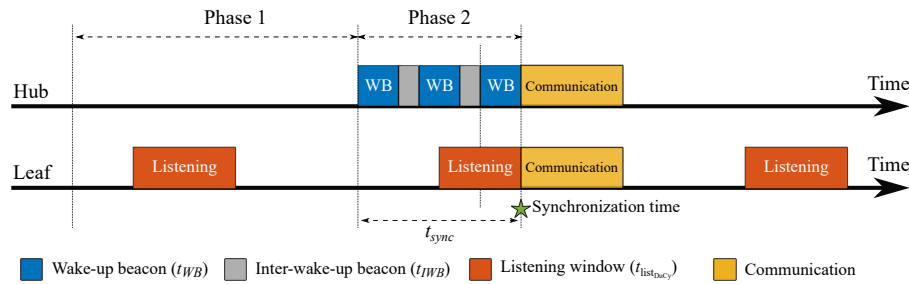
Figure 5.14: Duty-cycled receiver principle and associated additional synchronization time.

The additional synchronization time is not predictable as both nodes are asynchronous. It is of first importance to accurately model this extra time to establish its consequences at the system level, on all three metrics, within the framework of our research. As it is a probabilistic problem, we are interested in calculating the average additional wait time, t_{sync}, as the probability of receiving a full wake-up beacon knowing the listening window's probability of occurrence.

Figure 5.15 proposes a graphical representation for computing the average synchronization time $\bar{t}_{sync}$. For the solution to be generic, it does not deal with numerical values but with Time Unit (TU). All proportions are kept as detailed above. They are summarized in table 5.8.

Four different successive time-frames are pictured: $t=0$, $t=3$ TU, $t=6$ TU and $t=9$ TU. They represent all possible configuration as in this example, our system's listening window, T_{listen}, is 10 TU-periodic. The duty-cycle ratio is set to 50% as an example. For each configuration three listening windows, k-1, k and k+1, are presented to take into account the repetitive and periodic

Table 5.8: Duty-cycled problem solving time unit allocation

Description	Wake-up beacon	Inter-wake-up beacon	Listening window
Duration (TU)	2	1	5

leaf's listening behavior. We focus on the kth listening window. If the wake-up beacon falls within the time-frame from $t=0$ until $t \leq 3$ TU (noted "1"), then the synchronization would occur at the end of the first wake-up beacon, represented by the green star. This continuous timing alignment is discretized by the wake-up beacon full reception. The behavior is comparable for $t=3$ TU and $t=6$ TU. The last configuration is slightly different as it only lasts for 1 TU since the listening window occurs periodically. For $t>10$ TU, the configuration becomes the same as $t=0$.
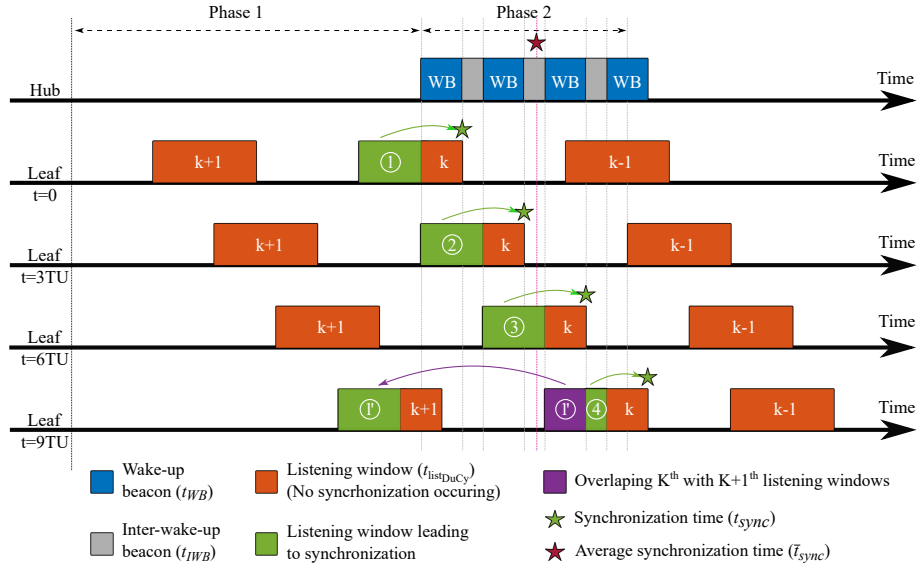
Figure 5.15: $\bar{t}_{sync}$ modeling and calculation. Example with $DuCy=50\%$.

Let's mathematically express the average additional synchronization time, $\bar{t}_{sync}$. It corresponds to the sum of probability, P_k, for a configuration to occur, multiplied by the elapsed time from the beginning of the synchronization (i.e. phase 2), as expressed in equation (5.22). The latter is a function of the duty cycle $DuCy$, the wake-up beacon duration, t_{WB}, and the inter-wake-up beacon duration $t_{I_{WB}}$.

$$\bar{t}_{sync} = \sum_{k=1}^{N} P_k \cdot t_{sync_k} \tag{5.22}$$

where:

- The probability, P_k, of catching any wake-up beacon but the last one is: $P_k = P_{WB_k}$ for $k \in [1; M]$

- M is defined as the maximum number of full wake-up beacon fitting within the listening period, T_{listen}, such as: $M = \left\lfloor \frac{T_{listen}}{t_{WB}+t_{I_{WB}}} \right\rfloor$

- The probability of catching the last wake-up beacon is: $P_k = P_{WB_N}$ for $k = N$ and $N = M + 1$

It must be noted that the beginning of the listening window may occur at any time with an equiprobability on its phase difference. Consequently, the probability of occurrence of an event,

P_k, is only defined as the time ratio between the duration while the event can happen, t_k, over the total listening period, T_{listen}, as described in equation (5.23).

$$P_k = \frac{t_k}{T_{listen}} \tag{5.23}$$

Except for the last wake-up beacon, unless it perfectly fits within the last time frame, $t_k = t_{WB} + t_{sw} + t_{I_{WB}}$. It corresponds shorter wake-up beacon pattern to be repeated until synchronization.

Equation (5.24) is obtained by developing (5.22):

$$
\begin{aligned}
\bar{t}_{sync} &= \sum_{k=1}^{M} P_{WB_k} \cdot t_{sync_k} + P_{WB_N} \cdot t_{sync_N} \\
&= \sum_{k=1}^{M} \frac{t_k}{T_{listen}} \cdot (t_{WB} + (t_{WB} + t_{I_{WB}})(k-1)) + \\
&\quad \frac{T_{listen} - M \cdot t_{list_{DuCy}}}{T_{listen}} \cdot (t_{WB} + (t_{WB} + t_{I_{WB}})(N-1))
\end{aligned}
\tag{5.24}
$$

By applying the above calculation to figure 5.15, with a 50% duty-cycled receiver, the resulting average additional synchronization time is: $\bar{t}_{sync}$=5.6 TU. It is identified in the figure by the pink star.

The channel availability and system power consumption are calculated with a similar approach to the heartbeat synchronization scheme presented in section 5.2.

5.3.3 Comparison

This section is dedicated to comparing both synchronization approaches under the same conditions within the framework of the Human Intranet. The comparison scenario is the following. It includes a hub and a leaf only. The latter is set to transmit data towards the hub every Lat=200 ms for the duration of the superframe, T. The leaf's data generation rate is set to D_{gen}=1 kbps. It is assumed that the data generated between two consecutive uploads are stored in a memory and uploaded all at once.

It is important noting that both schemes are compared with the same three metrics but depend on totally different input parameters. On one hand, the heartbeat-based synchronization outcome depends on the superframe duration, T. On the other hand, the duty-cycled receiver mechanism is a function of the duty cycle, $DuCy$. Therefore, the comparison charts below present both variables along two distinct Y-axis while the results are read along the X-axis (unless a single variable is plotted).

5.3.3.1 Channel Availability Comparison

The channel availability (CA) results for both schemes are plotted in figure 5.16. The Heartbeat-based synchronization sees its channel availability decreasing monotonously with the superframe duration as presented within section 5.3.1. It reaches a minimum of 96% for a superframe of T=1500 ms (i.e. heart rate of HR=40 bpm). The duty-cycled approach offers a better average channel availability for duty cycle ratios greater than $DuCy$>5%. However, it must be noted that the channel availability drops abruptly and significantly below CA<96% for duty cycles lower than $DuCy$<3%. Also, as stated within section 5.3.2, the duty cycle scheme relies on probabilities. Consequently, the channel availability can be approximated to its average (as plotted) but cannot be guaranteed. To highlight this particularity, figure 5.16 includes error bars, specifying the possible range of results around their mean. Given this probabilistic nature,

the only possibility to ensure a channel availability as good as the heartbeat-based scheme is to set the duty cycle above $DuCy > 11\%$.
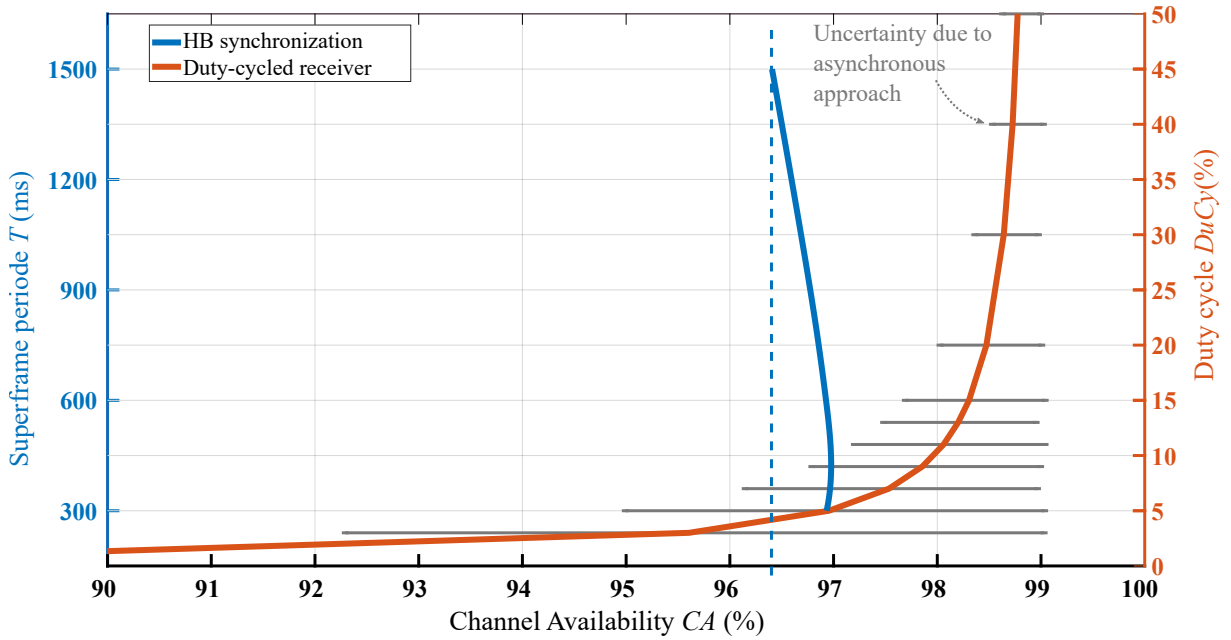
Figure 5.16: Achievable channel availability with HB-sync and Duty-cycled receiver.

5.3.3.2 System Power Consumption Comparison

Figure 5.17 compares the system power consumption for both synchronization and communication approaches. The heartbeat-based system power consumption increases monotonously with the superframe duration in a similar manner as the channel availability. In fact, the superframe-dependent terms in equations (5.16) and (5.19) are the same. As expected, the system power consumption reaches a maximum for the longest superframe of $T=1500$ ms (i.e. heart rate of $HR=40$ bpm) at $P=450\,\mu$W.
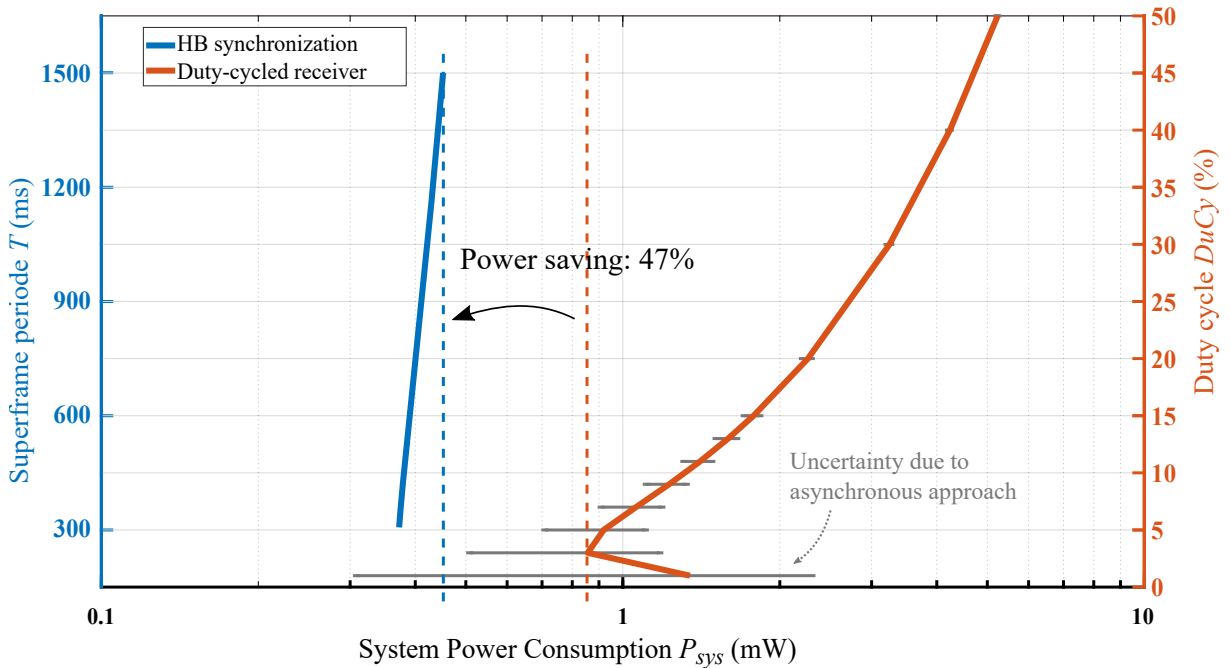
Figure 5.17: System power consumption with HB-sync and Duty-cycled receiver.

The duty-cycled receiver shows a system power consumption following a V-shape, with a local minimum at $DuCy=3\%$. Such behavior is observed as the duty cycle impacts both nodes:

the receiver and the transmitter. For low ratios, the hub power consumption increases as it needs to send more wake-up beacons until the leaf is finally waken-up, as it spends most of its time in sleep mode. On the other hand, higher duty cycles imply opening a listening window more frequently, increasing the power consumed by the leaf. Since the system power consumption takes into account the global energy spent to establish the communication, an optimum appears on the plot. Again, due to its asynchronous nature, the associated system power consumption is variable for a given duty cycle.

For an upload every Lat=200 ms the heartbeat-based synchronization scheme achieves a 47% power saving in a worst-to-best comparison (HB-sync maximum vs. Duty-cycle-sync minimum). Ultimately, the power saving increases up to 68% if we consider a duty cycle of $DuCy$=11%. Such a ratio is the minimum to guarantee under any circumstances that the duty-cycle approach offers a channel availability as good as the Heartbeat-based scheme, as presented within the previous section.

5.3.3.3 Communication latency

One of the main differences highlighted earlier between both schemes lies in their synchronization mechanism: synchronous for the heartbeat-based scheme, and asynchronous for the duty-cycled receiver.

The heartbeat-based synchronization scheme does not suffer any additional synchronization latency (as defined within section 5.2). The reason is dual:

- It offers a synchronous approach, paced by the heartbeat. The considered bio-signal, not generated by the system, allows all nodes included in the network to sync-up on the same event all over the body.

- The above mechanism still suffers variability on the exact synchronization signal detection time as well as the embedded local timing accuracy. Consequently, to compensate for those limitations, a synchronization margin was established to mitigate the overall timing errors.

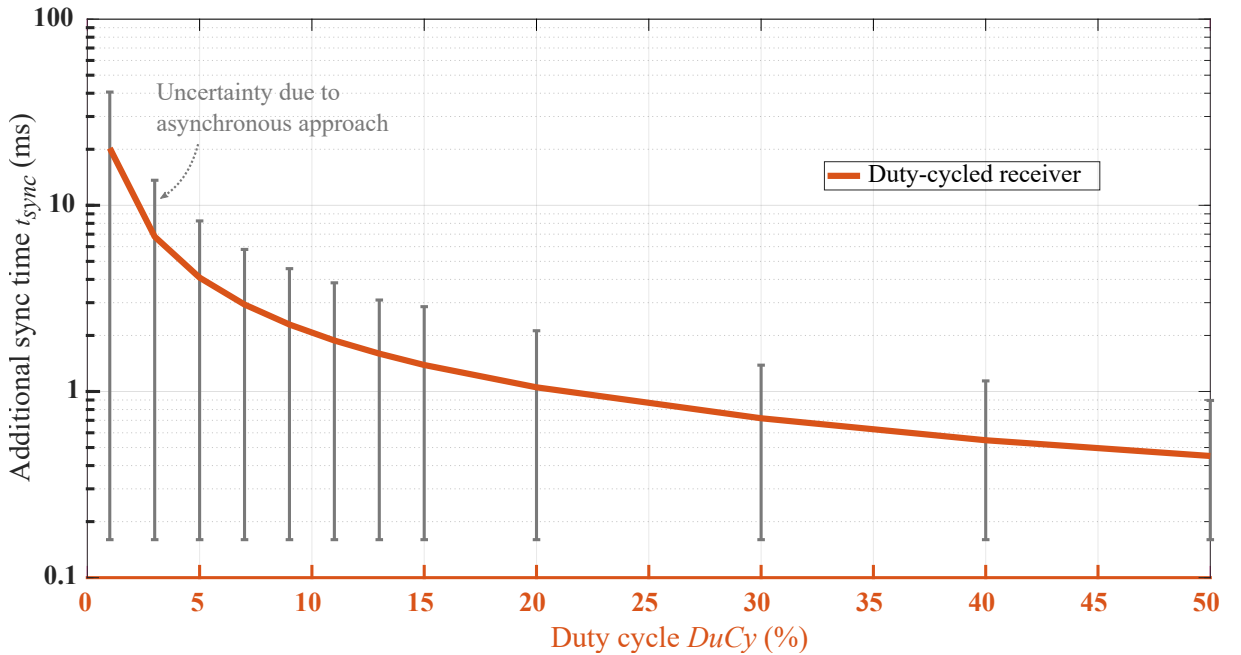Figure 5.18: System power consumption with HB-sync and Duty-cycled receiver.

On the other hand, the duty-cycled receiver is purely asynchronous. It consequently requires an initial synchronization phase before any communication, leading to an additional and mandatory synchronization latency. The latter was mathematically expressed within section 5.3.2 and

the resulting numerical values are presented in figure 5.18.

The additional synchronization time is inversely proportional to the duty cycle and increases exponentially with lower ratios. It is worth noting that this expected behavior is the same as the channel availability highlighted in figure 5.16. In fact, both (the CA decrease and the additional synchronization time) are linked by the phenomena: for low duty cycles, it takes longer, on average, for a weak-up beacon to be fully received. Consequently, the channel availability decreases as the hub is busy firing the wake-up signal. In parallel, this elapsed corresponds to the additional synchronization latency.

Figure 5.18 shows an average additional synchronization time greater than $\bar{t}_{sync}>2$ ms for duty cycles lower than $DuCy<10\%$. The associated probabilistic nature highlight that for a given setting, the maximum additional synchronization time can be as high a three times the calculated average. Finally, to guarantee a reactivity below 1 ms (i.e. $\bar{t}_{sync}<1$ ms), a duty cycle greater than $DuCy>50\%$ is compulsory, soaring the system power consumption as covered earlier.

5.4   Conclusion

This chapter has presented a system-level analysis centered on the heartbeat synchronization concept introduced in chapter 4. This new synchronization scheme, benefits from the on-body network deployment. This chapter has proposed a quantitative performance analysis and presented a metered comparison with one of the most attractive low power synchronization solution: a duty-cycled radio.

To perform such a quantitative analysis, the synchronization function has been divided into two functional blocks: the heartbeat detector and the timer. The former has been designated to detect the peak of the highest amplitude within the QRS complex (R-wave), setting the communication superframes boundaries. On the other hand, the timer in charge of the time-division within the superframe, defining the sub-frames managing the communication. Both functional blocks have been mathematically modeled, including their respective non-idealities and resulting timing errors. The heartbeat detection function suffers the signal propagation time between two nodes, defined as the heartbeat skew. The timer, however, faces intrinsic inaccuracy as it is based on a free-running oscillator, usually more power-efficient. Those sources of timing errors are: (i) the oscillator offset frequency, (ii) its frequency drift and, (iii) the resulting accumulated random jitter.

The above-listed timing error sources have been addressed by defining a synchronization margin within the proposed communication scheme. It consists of switching the receiver node into listening mode ahead of the theoretical upload schedule. It frees both nodes from an additional status checking phase as it ensures both node timing alignment when the transmission begins.

Three metrics have been established: the latency, channel availability and, system power consumption. The latency specifies how often the data exchange takes place. The channel availability represents how degraded is the main traffic from hub-to-hub. Ultimately, the system power consumption corresponds to the overall energy spent by all involved nodes. Those three metrics enable the synchronization scheme efficiency evaluation and highlight each system parameters' contribution to the final results.

Analytical simulations have been conducted, relying on state-of-art published implementation and effective results. Although, conservative values have been considered. The oscillator's frequency of operation has been defined to minimize the maximum time difference between two nodes, per puncturing event. It was chosen as $f_{osc} = 10$ kHz. It has been highlighted that for heart rates higher than 100 bpm, the heartbeat skew is dominant. For lower heart rates, the oscillator is the dominant source of inaccuracy. It is worth noting that the oscillator's timing

errors come from the hardware implementation. An optimized design would improve the timer accuracy. Regarding the heartbeat skew, it is only due to the signal propagation speed. To limit its impact on the system, a calibration operated on the MAC layer could be helpful. An extended feature would also clarify each node's relative position to the heart, reducing even further the synchronization margin required. Such a calibration mechanism could improve the system power consumption by 30% (for a latency of 200 ms and heart rate of 80 bpm).

The channel availability and the system power consumption are a function of the superframe duration and the communication period (i.e. the latency). The channel availability decreases with the superframe length and the upload period. The system power consumption behaves following the exact opposite as a source of the channel availability degradation (i.e. the wait time), is also the cause for the system power consumption increase. It impacts both simultaneously.

The leaf power breakdown has also been investigated. Given the communication scenario (where a leaf uploads data towards its dedicated) and the proposed communication scheme, the timing alignment constraint has been moved onto the hub. Consequently, the most consuming block from a leaf standpoint is its transmitter. Its power-share has been established above 80% for an average bit transmission rate of 10 bit/s. Improving the transmitter energy efficiency would immediately decrease the leaf power consumption, leading to extended battery life or a smaller embedded reserve of energy.

Based on the mathematical models and corresponding results, a comparison with a duty-cycled receiver has been conducted for a fixed scenario within the Human Intranet framework. In terms of channel availability, the duty-cycled receiver can achieve results as good as the heartbeat-based synchronization. However, due to its probabilistic nature, duty cycles above 11% and required to equal heartbeat-based counterpart under any circumstances. Regarding the system power consumption, the heartbeat-based synchronization offers at least a power saving of 47% in a worst-to-best comparison. This number increases up to 68% while ensuring equivalent channel availability. Finally, the heart-beat based synchronization does not suffer additional latency while the duty-cycled receiver does. The former offers a deterministic behavior while the latter is probabilistic. Such a drawback could be problematic for critical application in particular.

6. Conclusion and Future Work

6.1   Conclusion

This research work has been focusing on the development of a wearable platform addressing the Human Intranet. The Human Intranet concept has been introduced and its requirement highlighted: robustness, reliability, low power, safety and security.

While those requirements have been presented in chapter 1, multiple communication mechanisms have been reviewed in the second chapter. The different communication options investigated were: regular RF, Ultra Wide Band (UWB), ultrasonic and Body Coupled Communication (BCC). The latter highlighted the highest level of compatibility and the greatest potential to build the Human Intranet. Within BCC, three types were studied: Magnetic coupling, Galvanic coupling, and Capacitive coupling (C-BCC). C-BCC offered the best trade-off in terms of attenuation, range, bandwidth, form factor and room for improvement. However, its main drawback is the strong influence of the return path on the channel characteristics. It makes C-BCC sensitive to environment variations. Nevertheless, C-BCC has been selected as our solution of choice to establish the Human Intranet. Its downsides have been identified and addressed.

Given the reported results from the state of the art, we oriented our research towards C-BCC with a higher frequency to address the Human Intranet needs. A full communication channel characterization has been performed and presented in chapter 3. The theoretical analysis has highlighted that a higher frequency of operation of 450 MHz makes the surface waves the dominant propagation mechanism. Surface wave propagation directly addresses the return path limitation as the latter influence on the communication channel is minor.

The theoretical study has been followed by electromagnetic simulations with Ansoft HFSS software. The electrode-set was 3D-modeled, according to the real electrode built in the lab. In addition, a simple 3D human arm phantom has been designed (in HFSS). Two main types of simulation have been conducted: in free-space, and on-phantom. The surface wave behavior expected from theory has been confirmed in simulation and a good fit between the two has been highlighted. Furthermore, the on-phantom simulation results showed a larger propagation distance of the E-field than in free-space, the body acting as a kind of wave guide. Ultimately, the simulation results also highlighted a wide band behavior of the electrode over a frequency range of at least 100 MHz centered in 450 MHz.

The last stage of our channel characterization consisted of performing real measurements. An experimental on-body communication system has been fabricated with off-the-shelf component. This prototype was fully battery powered, the only appropriate configuration to evaluate a C-BCC channel. Two of these devices have been used, one set as the transmitter while the other was configured as a receiver. From those measurement results, initial assumptions and results from simulation have been confirmed. First, the on-body attenuation was lower than in free-space by at least 20 dB and up to 45 dB (over a distance of 20 cm). Second, the flat attenuation over over a bandwidth of 90 MHz has been recorded, confirming the the advantage of C-BCC and the surface dominance as the main propagation mechanism. A global attenuation of 60 dB, 65 dB, and 70 dB have been reported for separation distances of 20 cm, 30 cm, and 40 cm respectively. Ultimately, a torso-to-back communication has been achieved with a path loss similar to the 40 cm distance in line-of-sight. Finally, a path loss model has been proposed. The predicted attenuation is coherent with the measurements, however, due to the human body non-homogeneity, the model gives more a trend over distance than precise results.

To conclude regarding C-BCC potential in enabling communication over the human body,

a comparison with six other wireless communication techniques has been conducted under the same scenario on a human arm. The other technology involved were: (i) 450 MHz BCC, (ii) 450 MHz Monopoles, (iii) 915 MHz Printed dipoles, (iv) 2 GHz Monopoles, (v) 2 GHz Dipole arrays, and (vi) 2.4 GHz Bluetooth. While C-BCC has the highest insertion loss it also offers the lowest attenuation per unit of distance and the smaller for factor. It is also the only technology offering such a wide bandwidth of 90+ MHz.

Capacitive Body Coupled Communication has been thoroughly studied in the 400-500 MHz frequency band, highlighting attractive results to build the Human Intranet. Its ability to enable communication over the human body is desirable, the propagation mechanism involved at those frequency tackles the limitations highlighted in chapter 2, especially on the return path. In fact, the classic C-BCC representation from figure 2.14 is not entirely correct for frequencies of operation above a few tens of MHz as only recently (March 2019) proven in Nature Scientific Reports [42]. Finally, the wide bandwidth available, makes a pulse-based communication possible, allowing a strong transceiver duty-cycling, lowering the nodes' power consumption.

The next stage of our research focused on finding the most appropriate network structure and associated communication mechanism to meet the Human Intranet requirements. By analyzing a potential medical use-case for the Human Intranet, we established two types of nodes: the hubs and the leaves. The former embeds important capabilities in terms of communication, computing power and access to energy. The latter is meant to be simpler, mostly gathering and transmitting data. Given those two node categories, different network architecture were reviewed leading to a hybrid solution: a mesh of star network. This hybrid topology offers a reliable and robust network backbone which connects the hubs together in a mesh (or partial mesh). The local star configuration connects the leaves to a single hub. This approach lowers the complexity on the leaf, permitting simple and a more energy efficient design.

Achieving a communication over the the human body, not only requires a physical layer and a network architecture but also a MAC layer, as presented in chapter 4. The IEEE 802.15.4 and 802.15.6 standards have been reviewed. Their intrinsic limitations do not permit to directly apply them given the Human Intranet requirements, our physical layer, and the hybrid network topology proposed above. However, many concepts have been reused such as the superframe approach, delimited with beacons, and the TDMA access to the physical layer while developing our own porposed MAC protocol. Besides, the wake-up receiver approach and radio-duty cycling mechanism have been studied as well. They offer attractive power saving scheme without always necessitating all nodes to be synchronized. The duty-cycle radio concept quickly losses its interest in a scenario with frequent communications such as the Human Intranet.

In an attempt to combine the best of both worlds (beacon-based superframes, TDMA, and non-synchronized nodes), a heartbeat-based communication scheme in combination with a puncturing approach have been proposed. In consists of using the subject's heartbeat a common and shared clock to synchronize the nodes. It has the advantage of not being generated by the network which saves power and does not take any communication bandwidth to be shared among the network. It also adapts to the physical activity, without additional sensing capabilities required. The heartbeats and then used to define the communication superframe boundaries, similar to the beacon role in the IEEE standards mentioned earlier. However, a below-3 Hz synchronization clock is not sufficient to appropriately pace the communication in the Human Intranet framework. Consequently, a puncturing approach, prioritizing the hub-to-hub communication (as they are the main nodes) but allowing periodic leaf-to-hub data exchange has been proposed. The latter occur on "appointment", requiring both nodes to ready on time to allow the communication and avoid losing data.

The heartbeat-based communication scheme has been presented in depth and mathematically modeled in chapter 5. To achieve such synchronization and communication, two functional blocks are required: (i) a heartbeat detector and, (ii) a timer. Both non-idealities blocks have been

taken into account. The heartbeat detector suffers of the heartbeat skew, which corresponds to the electric signal propagation within the body. The timer is made of two sub-blocks: an oscillator and a counter. The oscillator suffers three non-idealities: (i) its static frequency offset, (ii) its drift in time and, (iii) the accumulated random jitter. All the above-listed non idealities lead to a global timing error on both end, impacting both nodes alignment, potentially leading to a communication failure.

A synchronization margin as then been defined following a worst-case approach. It consists of the maximum possible timing error added from all four sources. Based on the mathematical model, equation-based calculation were performed associated with conservative numerical values taken from the state-of-the-art. We established that a 10 kHz oscillator frequency optimizes the maximum timing error and then the synchronization margin necessary. It was highlighted that for lower heart rates, the oscillator drift is the dominant source of timing error as the superframes are longer. On the other hand, for higher heart rate, the timing error will mostly suffer from the heartbeat skew.

For comparison purposes, the duty-cycled radio approach as also been modeled ans used as a reference to evaluate the performance of our proposed heartbeat-based synchronization scheme. Both approach were studied under the same configuration, including one hub-leaf pair. Three metrics have been defined: (i) the channel availability, (ii) the latency, and (iii) the system power consumption. The comparison scenario involved a hub-to-leaf communication period of 200 ms. The heartbeat-based synchronization system power consumption achieves a power saving of at least 47% in the given scenario. It is worth noting that the duty-cycle radio is asynchronous leading to a probabilistic behavior. In other words, the average expected performance cannot be guaranteed. The only solution to secure a minimum performance is to increase the duty-cycle ratio. Ultimately, due to probabilistic behavior, the duty-cycle receiver suffers additional synchronization time where the heartbeat-based scheme does not since its behavior is deterministic. Finally, the Heartbeat-based synchronization approach performs more efficiently in the Human Intranet context than a duty-cycled receiver. The former is offering an energy efficient and reliable (due to its deterministic nature) solution to enable the communication within a mesh of star network with a single channel PHY, such as the one envisioned for the Human Intranet.

In this research work within the Human Intranet framwork, Capacitive Body Coupled communication has been evaluated for frequencies between 400 MHz and 500 MHz highlighting desirable characteristics to efficiently enable the communication over the human body. A mesh of star hybrid network topology has been proposed as the network backbone architecture along with a heartbeat synchronization scheme combined with a puncturing approach. The latter has been evaluated highlighted good results in a realistic scenario, performing better than other solutions such as a duty-cycled radio.

6.2 Future Work

To further improve the results obtained in this research work, three main topics have been identified as the future work to be addressed and presented in this section.

The electrode design

The electrode-set used to perform the measurement were designed with off-the-shelf components and assemble in order to propose a proof of concept. The help of printed electronics enable a smaller form factor, a greater contact with the skin and optimized performance. An appropriate design, optimized with electromagnetic simulation software including a body model will decrease the insertion losses, improving the channel loss and make C-BCC more competitive compared to other RF solution.

In addition, a multi-purpose electrode-set, combining C-BCC and heartbeat detection abil-

ities can be imagined with a convenient form factor as proposed in [119]. Such design would allow having a single patch interfacing the body for each node enabling the synchronization and communication functions envisioned for the Human Intranet.

Transceiver implementation on silicon

The measurement performed with our prototype allowed a realistic demonstration that C-BCC is carrying desirable characteristics for a frequency of operation between 400 MHz and 500 MHz. However, only a continuous wave was generated from the transceiver. A dedicated transceiver, implementing a impulse radio will allow, proper communication while benefiting from the wide bandwidth available and potentially achieving cutting edge energy efficiency. In addition, the same transceiver could be compatible with multiple data rate, by managing the "inter-pulse" duration. Ultimately, the transceiver could embed the synchronization blocks with improved characteristics compared to the values taken to perform the simulation, minimizing the timing errors on each nodes.

The obtained results permitted to start another Ph.D. program taking over this achieved work and centered on implementing beyond-state-of-the-art hardware with cutting-edge technology.

The MAC Layer

The simple heartbeat-based MAC layer can be completed, including advanced feature such as handling connections and disconnections, the heartbeat detector duty cycling scheme such as the one depicted in [95]. In addition, the sycnrhonization margin required can be minimized. A calibration phase would identify the relative location of each node to the heart and compensate for the heartbeat skew, reducing even further the wait time. Such a feature can benefits from the wide band communication available in combination with the time of flight accessible with impulse radios. Such calibration mechanism could improve the system power consumption by 30% (for a latency of 200 ms and a heart rate of 80 bpm).

Bibliography

[1] J. M. Rabaey, "The human intranet: where swarms and humans meet," in *Proceedings of the 2015 Design, Automation & Test in Europe Conference & Exhibition.* EDA Consortium, 2015, pp. 637–640.

[2] CSEM, Centre Suisse D'electronique Et De Microtechnique Sa - Recherche Et Developpement, "WiserBAN, smart miniature low-power wireless microsystem for Body Area Networks," https://cordis.europa.eu/docs/projects/cnect/4/257454/080/deliverables/001-WiserBANWP3D31Final20111007.pdf, last accessed on Nov 24, 2020.

[3] Ł. Januszkiewicz, "Analysis of human body shadowing effect on wireless sensor networks operating in the 2.4 ghz band," *Sensors*, vol. 18, no. 10, p. 3412, 2018.

[4] A. Fort *et al.*, "Ultra-wideband channel model for communication around the human body," *IEEE Journal on Selected Areas in Communications*, vol. 24, no. 4, pp. 927–933, 2006.

[5] R. E. Fields, "Evaluating compliance with fcc guidelines for human exposure to radiofrequency electromagnetic fields," *OET bulletin*, vol. 65, no. 10, 1997.

[6] T. Ogasawara *et al.*, "Human body communication based on magnetic coupling," *IEEE Transactions on Antennas and Propagation*, vol. 62, no. 2, pp. 804–813, 2013.

[7] J. Yoo, "Body coupled communication: Towards energy-efficient body area network applications," in *Radio-Frequency Integration Technology (RFIT), 2017 IEEE International Symposium on.* IEEE, 2017, pp. 244–246.

[8] Y. K. Hernández-Gómez *et al.*, "Magnetic human body communication based on double-inductor coupling," in *2017 IEEE International Instrumentation and Measurement Technology Conference (I2MTC).* IEEE, 2017, pp. 1–6.

[9] Y. Fujita, F. Koshiji, and K. Koshiji, "Transmission characteristics through the bent arm wearing magnetically-coupled coils for body area communication," in *2015 IEEE 4th Global Conference on Consumer Electronics (GCCE).* IEEE, 2015, pp. 481–482.

[10] M. S. Wegmueller *et al.*, "Signal transmission by galvanic coupling through the human body," *IEEE Transactions on Instrumentation and Measurement*, vol. 59, no. 4, pp. 963–969, 2009.

[11] Q. Zhang *et al.*, "Assessment of on-body skin-confined propagation for body area network," *IEEE Antennas and Wireless Propagation Letters*, vol. 16, pp. 2610–2613, 2017.

[12] P. Chen *et al.*, "All-digital galvanically-coupled bcc receiver resilient to frequency misalignment," *IEEE transactions on biomedical circuits and systems*, vol. 11, no. 3, pp. 714–726, 2017.

[13] T. G. Zimmerman, "Personal area networks (pan): Near-field intra-body communication," Master's thesis, MIT, 1995.

[14] J. Mao, H. Yang, and B. Zhao, "An investigation on ground electrodes of capacitive coupling human body communication," *IEEE transactions on biomedical circuits and systems*, vol. 11, no. 4, pp. 910–919, 2017.

[15] N. Seyed Mazloum, "Body-coupled communications-experimental characterization, channel modeling and physical layer design," Master's thesis, Chalmers University of Technology, 2008.

[16] N. Cho *et al.*, "The human body characteristics as a signal transmission medium for intrabody communication," *IEEE transactions on microwave theory and techniques*, vol. 55, no. 5, pp. 1080–1086, 2007.

[17] J. Bae *et al.*, "The signal transmission mechanism on the surface of human body for body channel communication," *IEEE Transactions on microwave theory and techniques*, vol. 60, no. 3, pp. 582–593, 2012.

[18] K. Zhang *et al.*, "Modeling and characterization of the implant intra-body communication based on capacitive coupling using a transfer function method," *Sensors*, vol. 14, no. 1, pp. 1740–1756, 2014.

[19] A. Moin *et al.*, "Optimized design of a human intranet network," in *Proceedings of the 54th Annual Design Automation Conference 2017*, 2017, pp. 1–6.

[20] IEEE, "Iso/iec/ieee international standard - information technology – telecommunications and information exchange between systems – local and metropolitan area networks – specific requirements – part 15-6: Wireless body area network," *ISO/IEC/IEEE 8802-15-6:2017(E)*, pp. 1–274, March 2018.

[21] R. X. Stroobandt, S. S. Barold, and A. F. Sinnaeve, *ECG from Basics to Essentials: Step by Step.* John Wiley & Sons, 2016.

[22] J. M. Rabaey, "The swarm at the edge of the cloud-a new perspective on wireless," in *VLSI Circuits (VLSIC), 2011 Symposium on.* IEEE, 2011, pp. 6–8.

[23] E. A. Lee *et al.*, "The swarm at the edge of the cloud," *IEEE Design & Test*, vol. 31, no. 3, pp. 8–20, 2014.

[24] G. Slack, "The last firewall," *Berkeley Engineer*, pp. 8–11, Sping 2014.

[25] IEEE, "Ieee standard for safety levels with respect to human exposure to radio frequency electromagnetic fields, 3 khz to 300 ghz," *IEEE Std C95.1-2005 (Revision of IEEE Std C95.1-1991)*, pp. 1–238, April 2006.

[26] IEEE, "Ieee standard for safety levels with respect to human exposure to radio frequency electromagnetic fields, 3 khz to 300 ghz amendment 1: Specifies ceiling limits for induced and contact current, clarifies distinctions between localized exposure and spatial peak power density," *IEEE Std C95.1a-2010 (Amendment to IEEE Std C95.1-2005)*, pp. 1–9, March 2010.

[27] A. Moin *et al.*, "Adaptive body area networks using kinematics and biosignals," *IEEE Journal of Biomedical and Health Informatics*, 2020.

[28] M. Ghamari *et al.*, "Comparison of low-power wireless communication technologies for wearable health-monitoring applications," in *2015 International Conference on Computer, Communications, and Control Technology (I4CT).* IEEE, 2015, pp. 1–6.

[29] J. F. Zhao *et al.*, "A review on human body communication: signal propagation model, communication performance, and experimental issues," *Wireless Communications and Mobile Computing*, vol. 2017, 2017.

[30] A. F. Harris III *et al.*, "Bluetooth low energy in dense iot environments," *IEEE Communications Magazine*, vol. 54, no. 12, pp. 30–36, 2016.

[31] S. M. Abbas *et al.*, "On-body antennas: Design considerations and challenges," in *2016 URSI International Symposium on Electromagnetic Theory (EMTS)*. IEEE, 2016, pp. 109–110.

[32] S. Dumanli, "On-body antenna with reconfigurable radiation pattern," in *2014 IEEE MTT-S International Microwave Workshop Series on RF and Wireless Technologies for Biomedical and Healthcare Applications (IMWS-Bio2014)*. IEEE, 2014, pp. 1–3.

[33] A. S. Andrenko, I. Ida, and T. Kikuzuki, "Dual-band patch antenna with monopole-like radiation patterns for ban communications," in *2013 7th European Conference on Antennas and Propagation (EuCAP)*. IEEE, 2013, pp. 1922–1926.

[34] S. M. S. Razafimahatratra, "Contribution au dimensionnement d'une liaison radio sur le corps humain: étude canal et antenne à 60 ghz," Ph.D. dissertation, Université Pierre et Marie Curie-Paris VI; Université libre de Bruxelles . . . , 2017.

[35] FCC, "safety of radiofrequency (RF) and microwave emissions from transmitters and facilities regulated by the FCC." https://www.fcc.gov/engineering-technology/electromagnetic-compatibility-division/radio-frequency-safety/faq/rf-safety#:~:text=The%20most%20restrictive%20limits%20on,the%20whole%20body%20is%20exposed., last accessed on Dec 8, 2020.

[36] USGS, "The water in you: Water and the human body." https://www.usgs.gov/special-topic/water-science-school/science/water-you-water-and-human-body?qt-science_center_objects=0#qt-science_center_objects, last accessed on Nov 25, 2020.

[37] F. Rivet *et al.*, "Intra-body communications: radio-frequency versus ultrasonic," *Analog Integrated Circuits and Signal Processing*, vol. 87, no. 2, pp. 289–299, 2016.

[38] E. Demirors *et al.*, "High data rate ultrasonic communications for wireless intra-body networks," in *2016 IEEE International Symposium on Local and Metropolitan Area Networks (LANMAN)*. IEEE, 2016, pp. 1–6.

[39] G. E. Santagati *et al.*, "Medium access control and rate adaptation for ultrasonic intrabody sensor networks," *IEEE/ACM Transactions on Networking*, vol. 23, no. 4, pp. 1121–1134, 2014.

[40] M. A. Callejon *et al.*, "Distributed circuit modeling of galvanic and capacitive coupling for intrabody communication," *IEEE Transactions on Biomedical Engineering*, vol. 59, no. 11, pp. 3263–3269, 2012.

[41] K. Ito and Y. Hotta, "Signal path loss simulation of human arm for galvanic coupling intra-body communication using circuit and finite element method models," in *2015 IEEE Twelfth International Symposium on Autonomous Decentralized Systems*. IEEE, 2015, pp. 230–235.

[42] D. Das *et al.*, "Enabling covert body area network using electro-quasistatic human body communication," *Scientific reports*, vol. 9, no. 1, pp. 1–14, 2019.

[43] M. D. Pereira, G. A. Alvarez-Botero, and F. R. de Sousa, "Characterization and modeling of the capacitive hbc channel," *IEEE Transactions on Instrumentation and Measurement*, vol. 64, no. 10, pp. 2626–2635, 2015.

[44] B. Zhao *et al.*, "A low-power compact ieee 802.15. 6 compatible human body communication transceiver with digital sigma–delta iir mask shaping," *IEEE Journal of Solid-State Circuits*, vol. 54, no. 2, pp. 346–357, 2018.

[45] G. S. Anderson and C. G. Sodini, "Body coupled communication: The channel and implantable sensors," in *2013 IEEE International Conference on Body Sensor Networks*. IEEE, 2013, pp. 1–5.

[46] J. Mao *et al.*, "A self-adaptive capacitive compensation technique for body channel communication," *IEEE Transactions on Biomedical Circuits and Systems*, vol. 11, no. 5, pp. 1001–1012, 2017.

[47] J. Lee *et al.*, "A 48 μw, 8.88× 10- 3 w/w batteryless energy harvesting bcc identification system," in *2016 IEEE International Symposium on Circuits and Systems (ISCAS)*. IEEE, 2016, pp. 1806–1809.

[48] H. Cho *et al.*, "A 79pj/b 80mb/s full-duplex transceiver and a $42.5 mu\{mathrmW\}$ 100kb/s super-regenerative transceiver for body channel communication," in *Solid-State Circuits Conference-(ISSCC), 2015 IEEE International*. IEEE, 2015, pp. 1–3.

[49] J. Jang *et al.*, "4-camera vga-resolution capsule endoscope with 80mb/s body-channel communication transceiver and sub-cm range capsule localization," in *Solid-State Circuits Conference - (ISSCC), 2018 IEEE International*. IEEE, 2018, pp. 282–284.

[50] S. Maity *et al.*, "Secure human-internet using dynamic human body communication," in *Low Power Electronics and Design (ISLPED, 2017 IEEE/ACM International Symposium on*. IEEE, 2017, pp. 1–6.

[51] Z. alliance, "Zigbee specification," https://zigbeealliance.org/wp-content/uploads/2019/11/docs-05-3474-21-0csg-zigbee-specification.pdf, last accessed on Nov 26, 2020.

[52] Bluetooth SIG, "Core specification v5. 1," 2019.

[53] IEEE, "Ieee standard for low-rate wireless networks," *IEEE Std 802.15.4-2015 (Revision of IEEE Std 802.15.4-2011)*, pp. 1–709, 2016.

[54] H. Cho *et al.*, "21.1 a 79pj/b 80mb/s full-duplex transceiver and a 42.5 μw 100kb/s super-regenerative transceiver for body channel communication," in *Solid-State Circuits Conference - (ISSCC), 2015 IEEE International*. IEEE, 2015, pp. 1–3.

[55] J. Park and P. P. Mercier, "A sub-10-pj/bit 5-mb/s magnetic human body communication transceiver," *IEEE Journal of Solid-State Circuits*, vol. 54, no. 11, pp. 3031–3042, 2019.

[56] M. Seyedi *et al.*, "An energy-efficient pulse position modulation transmitter for galvanic intrabody communications," in *2014 4th International Conference on Wireless Mobile Communication and Healthcare-Transforming Healthcare Through Innovations in Mobile and Wireless Technologies (MOBIHEALTH)*. IEEE, 2014, pp. 192–195.

[57] W. Saadeh *et al.*, "A 1.1-mw ground effect-resilient body-coupled communication transceiver with pseudo ofdm for head and body area network," *IEEE Journal of Solid-State Circuits*, vol. 52, no. 10, pp. 2690–2702, 2017.

[58] N. Gershenfeld, *The physics of information technology*. Cambridge: Cambridge University Press, 2000.

[59] K. Norton, "The propagation of radio waves over the surface of the earth and in the upper atmosphere," *Proceedings of the Institute of Radio Engineers*, vol. 24, no. 10, pp. 1367–1387, 1936.

[60] K. A. Norton, "The propagation of radio waves over the surface of the earth and in the upper atmosphere," *Proceedings of the Institute of Radio Engineers*, vol. 25, no. 9, pp. 1203–1236, 1937.

[61] S. Gabriel, R. Lau, and C. Gabriel, "The dielectric properties of biological tissues: III. Parametric models for the dielectric spectrum of tissues," *Physics in Medicine & Biology*, vol. 41, no. 11, p. 2271, 1996.

[62] Mouser website, "Covidien. kendall ecg electrodes product data sheet." https://www.mouser.com/datasheet/2/813/H124SG-1022817.pdf, last accessed on Feb 29, 2020.

[63] H. T. Friis, "A note on a simple transmission formula," *Proceedings of the IRE*, vol. 34, no. 5, pp. 254–256, 1946.

[64] H. G. Schantz, "Near field propagation law & a novel fundamental limit to antenna gain versus size," in *2005 IEEE Antennas and Propagation Society International Symposium*, vol. 3.   IEEE, 2005, pp. 237–240.

[65] Minicircuits website, "Ceramic balun, RF Transformer NCS1.5-232+," https://www.minicircuits.com/pdfs/NCS1.5-232+.pdf, last accessed on March 24, 2020.

[66] STMicroelectronics website, "Steval-fki433v2," https://www.st.com/resource/en/data_brief/steval-fki433v2.pdf, last accessed on March 25, 2020.

[67] R. Benarrouch *et al.*, "Capacitive body-coupled communication in the 400–500 MHz frequency band," in *EAI International Conference on Body Area Networks*.   Springer, 2019, pp. 218–235.

[68] A. Thielens *et al.*, "A comparative study of on-body radio-frequency links in the 420 MHz–2.4 GHz range," *Sensors*, vol. 18, no. 12, p. 4165, 2018.

[69] M. Anderson *et al.*, "Ultra-low power on-antenna beamforming for antenna arrays using tunable passives," *IEEE MTT Lett*, vol. 29, no. 2, pp. 158–160, 2019.

[70] A. Moin *et al.*, "An EMG gesture recognition system with flexible high-density sensors and brain-inspired high-dimensional classifier," in *2018 IEEE International Symposium on Circuits and Systems (ISCAS)*.   IEEE, 2018, pp. 1–5.

[71] A. Fort *et al.*, "Indoor body-area channel model for narrowband communications," *IET microwaves, antennas & propagation*, vol. 1, no. 6, pp. 1197–1203, 2007.

[72] J. Grosinger, "Feasibility of backscatter RFID systems on the human body," *EURASIP journal on embedded systems*, vol. 2013, no. 1, pp. 1–10, 2013.

[73] L. Roelens *et al.*, "Path loss model for wireless narrowband communication above flat phantom," *Electronics Letters*, vol. 42, no. 1, pp. 10–11, 2006.

[74] L. Petrillo *et al.*, "Ban working frequency: A trade-off between antenna efficiency and propagation losses," in *The 8th European Conference on Antennas and Propagation (Eu-CAP 2014)*.   IEEE, 2014, pp. 3368–3369.

[75] A. Fort *et al.*, "A body area propagation model derived from fundamental principles: Analytical analysis and comparison with measurements," *IEEE Transactions on Antennas and Propagation*, vol. 58, no. 2, pp. 503–514, 2009.

[76] N. Katayama *et al.*, "Channel model on various frequency bands for wearable body area network," *IEICE transactions on communications*, vol. 92, no. 2, pp. 418–424, 2009.

[77] A. K. Majumdar, *Optical wireless communications for broadband global internet connectivity: fundamentals and potential applications*.   Elsevier, 2018.

[78] J. Elias and A. Mehaoua, "Energy-aware topology design for wireless body area networks," in *2012 IEEE international conference on communications (ICC)*.   IEEE, 2012, pp. 3409–3410.

[79] J. A. Afonso *et al.*, "Hierarchical wireless networks of body sensor networks for healthcare applications," in *Handbook of Research on Developments in E-Health and Telemedicine: Technological and Social Perspectives*.   IGI Global, 2010, pp. 65–86.

[80] Y. Xue and L. Jin, "A naturalistic 3d acceleration-based activity dataset & benchmark evaluations," in *2010 IEEE International Conference on Systems, Man and Cybernetics*.   IEEE, 2010, pp. 4081–4085.

[81] A. Ahmadi, D. D. Rowlands, and D. A. James, "Investigating the translational and rotational motion of the swing using accelerometers for athlete skill assessment," in *SENSORS, 2006 IEEE*. IEEE, 2006, pp. 980–983.

[82] Z. Alliance, "ZigBee Specification," https://zigbeealliance.org/wp-content/uploads/2019/11/docs-05-3474-21-0csg-zigbee-specification.pdf, last accessed on May 7, 2020.

[83] O. G. Osorio, B. S. R. Dazai, and O. J. Salcedo, "Comparative study of performance for 804.15. 4 zigbee and 6lowpan protocols." in *SOFSEM (Student Research Forum Papers/Posters)*, 2016, pp. 59–71.

[84] M. Hämäläinen and J. Iinatti, *Wireless UWB body area networks: Using the IEEE802. 15.4-2011*. Academic Press, 2014.

[85] M. Hernandez and R. Miura, *Body Area Networks using IEEE 802.15. 6: Implementing the ultra wide band physical layer*. Academic Press, 2014.

[86] S. A. Salehi *et al.*, "Ieee 802.15. 6 standard in wireless body area networks from a healthcare point of view," in *2016 22nd Asia-Pacific Conference on Communications (APCC)*. IEEE, 2016, pp. 523–528.

[87] S. Ullah, M. Mohaisen, and M. A. Alnuem, "A review of ieee 802.15. 6 mac, phy, and security specifications," *International Journal of Distributed Sensor Networks*, vol. 9, no. 4, p. 950704, 2013.

[88] N. Seyed Mazloum, "Duty-cycled wake-up schemes for ultra-low power wireless communications," Ph.D. dissertation, Lund University, 2016.

[89] N. S. Mazloum and O. Edfors, "Dcw-mac: An energy efficient medium access scheme using duty-cycled low-power wake-up receivers," in *2011 IEEE Vehicular Technology Conference (VTC Fall)*. IEEE, 2011, pp. 1–5.

[90] N. S. Mazloum and O. Edfors, "Influence of duty-cycled wake-up receiver characteristics on energy consumption in single-hop networks," *IEEE Transactions on Wireless Communications*, vol. 16, no. 6, pp. 3870–3884, 2017.

[91] K. Englehart, B. Hudgins *et al.*, "A robust, real-time control scheme for multifunction myoelectric control," *IEEE transactions on biomedical engineering*, vol. 50, no. 7, pp. 848–854, 2003.

[92] L. H. Smith *et al.*, "Determining the optimal window length for pattern recognition-based myoelectric control: balancing the competing effects of classification error and controller delay," *IEEE Transactions on Neural Systems and Rehabilitation Engineering*, vol. 19, no. 2, pp. 186–192, 2010.

[93] H. Li and J. Tan, "Heartbeat-driven Medium-Access Control for Body Sensor Networks," *IEEE transactions on information technology in biomedicine*, vol. 14, no. 1, pp. 44–51, 2009.

[94] R. Benarrouch *et al.*, "Heartbeat-based synchronization scheme for the human intranet: Modeling and analysis," in *2020 IEEE International Symposium on Circuits and Systems (ISCAS)*. IEEE, 2020, pp. 1–5.

[95] F. Solt *et al.*, "Energy efficient heartbeat-based mac protocol for wban employing body coupled communication," *IEEE Access*, vol. 8, pp. 182 966–182 983, 2020.

[96] S. Pirbhulal *et al.*, "Heartbeats based biometric random binary sequences generation to secure wireless body sensor networks," *IEEE Transactions on Biomedical Engineering*, vol. 65, no. 12, pp. 2751–2759, 2018.

[97] M. Ludwig *et al.*, "Measurement, prediction, and control of individual heart rate responses to exercise—basics and options for wearable devices," *Frontiers in physiology*, vol. 9, p. 778, 2018.

[98] D. Da He and C. G. Sodini, "A 58 nW ECG ASIC with Motion-tolerant Heartbeat timing Extraction for Wearable Cardiovascular Monitoring," *IEEE transactions on biomedical circuits and systems*, vol. 9, no. 3, pp. 370–376, 2014.

[99] P. S. Raj and D. Hatzinakos, "Feasibility of single-arm single-lead ecg biometrics," in *2014 22nd European Signal Processing Conference (EUSIPCO)*. IEEE, 2014, pp. 2525–2529.

[100] T. T. Habte *et al.*, *Ultra low power ECG processing system for IoT devices*. Springer, 2019.

[101] D. Teichmann *et al.*, "Non-contact monitoring techniques-principles and applications," in *2012 Annual International Conference of the IEEE Engineering in Medicine and Biology Society*. IEEE, 2012, pp. 1302–1305.

[102] O. T. Inan *et al.*, "Ballistocardiography and seismocardiography: A review of recent advances," *IEEE journal of biomedical and health informatics*, vol. 19, no. 4, pp. 1414–1427, 2014.

[103] J. Allen, "Photoplethysmography and its application in clinical physiological measurement," *Physiological measurement*, vol. 28, no. 3, p. R1, 2007.

[104] A. Kamal *et al.*, "Skin photoplethysmography—a review," *Computer methods and programs in biomedicine*, vol. 28, no. 4, pp. 257–269, 1989.

[105] H.-S. Cho and Y.-J. Park, "Detection of heart rate through a wall using uwb impulse radar," *Journal of healthcare engineering*, vol. 2018, 2018.

[106] N. Sperelakis, *Cell physiology source book: essentials of membrane biophysics*. Elsevier, 2012.

[107] T. Buchner and J. Gierałtowski, "How fast does the ECG signal propagate within the body," *Working Group for Cardiovascular Physics. Faculty of Physics, Warsaw University of Technology. Sixth Cardiology Meets Physics & Mathematics, At Zakopane*, vol. 6, 2015.

[108] H. Tanaka, K. D. Monahan, and D. R. Seals, "Age-predicted Maximal Heart Rate Revisited," *Journal of the american college of cardiology*, vol. 37, no. 1, pp. 153–156, 2001.

[109] P. Bjerregaard, "Mean 24 hour Heart Hate, Minimal Heart Rate and Pauses in Healthy Subjects 40–79 Years of Age," *European Heart Journal*, vol. 4, no. 1, pp. 44–51, 1983.

[110] D. Marchaland *et al.*, "Novel Pulse Generator Architecture Dedicated to Low Data Rate UWB Systems," in *The European Conference on Wireless Technology, 2005*. IEEE, 2005, pp. 229–232.

[111] Q. Gu, *RF System Design of Transceivers for Wireless Communications*. Springer Science & Business Media, 2006.

[112] H. R. Anderson, *Multiple-Access Techniques*. John Wiley & Sons, Ltd, 2003, ch. 8, pp. 275–320.

[113] U. R. Acharya *et al.*, "Heart Rate Variability: a Review," *Medical and biological engineering and computing*, vol. 44, no. 12, pp. 1031–1051, 2006.

[114] Mayo Clinic, "What's a normal resting heart rate?" https://www.mayoclinic.org/healthy-lifestyle/fitness/expert-answers/heart-rate/faq-20057979, last accessed on July 1, 2020.

[115] N. Da Dalt and A. Sheikholeslami, *Understanding Jitter and Phase Noise: A Circuits and Systems Perspective.* Cambridge University Press, 2018.

[116] M. Zielinski *et al.*, "Estimation of the clock signal jitter using the time-interval measurement system," in *Proc. of XVIII IMEKO World Congress Metrology for a Sustainable Development.* Citeseer, 2006.

[117] M. Zieliński *et al.*, "Accumulated jitter measurement of standard clock oscillators," *Metrology and Measurement Systems*, vol. 16, no. 2, pp. 259–266, 2009.

[118] S. Jeong *et al.*, "A 5.8 nW CMOS wake-up timer for ultra-low-power wireless applications," *IEEE Journal of Solid-State Circuits*, vol. 50, no. 8, pp. 1754–1763, 2015.

[119] Y. Khan *et al.*, "Flexible hybrid electronics: Direct interfacing of soft and hard electronics for wearable health monitoring," *Advanced Functional Materials*, vol. 26, no. 47, pp. 8764–8775, 2016.

APPENDICES

A Matlab code for accumulated random jitter verification

The code below was ran in Matlab to verify the accumulated random jitter theoretical expression in section 5.1.2.3.

```matlab
clear all
close all

Duration=50e-3; %Reference cycle duration
% Freq_list=[100 1e3 10e3 100e3 1e6]; %Oscillator frequencies
Freq_list=logspace(3,6); %Oscillator frequencies
Nb_iteration=10000; %Number of iteration of the random process


Acc_jitter_avg=zeros(Nb_iteration, length(Freq_list)); %Create and
    initiliaze variable
NbCy=round(Duration.*Freq_list); %Number of cycle for the given duration
    with the
%listed frequencies
std_freq=zeros(1,length(Freq_list)); %Create and initiliaze variable

for i=1:1:Nb_iteration
for j=1:1:length(Freq_list)
Acc_jitter_avg(i,j)=(sum(randn(1,NbCy(j)))/NbCy(j)); %Average accumulated
    jitter over
%the number of cycle with Normally distributed pseudorandom numbers
end
end

for k=1:1:length(Freq_list)
std_freq(k)=std(Acc_jitter_avg(:,k)); % Accumulated random jittervariance
    over the
%number iteration (10k)
end


figure('DefaultTextFontName', 'Times', 'DefaultAxesFontName', 'Times');
set(gcf,'color','w');
hold on
set(gca, 'XScale', 'log')
set(gca, 'fontsize',18)
plot(Freq_list,std_freq, 'linewidth',4)
plot(Freq_list,1./sqrt(NbCy), '--', 'linewidth',4) %theoretical expected
    results
hold off
grid on
box
xlabel('Oscillator frequency (Hz)')
ylabel('Avg variance per oscillation')
leg=legend('$\sigma$ calculated','$\frac{1}{\sqrt{Number of cycle}}$');
set(leg, 'Interpreter', 'latex')
```